BINARY AND TERNARY DECAY DYNAMICS OF NUCLEAR SYSTEMS WITHIN FRAGMENTATION APPROACH

A THESIS

Submitted for the partial fulfillment of requirement for the award of the degree of

DOCTOR OF PHILOSOPHY

By

Nitin Sharma

(Reg. No: 901812010)

Under the supervision of

Dr. Manoj K. Sharma

Professor

SCHOOL OF PHYSICS AND MATERIALS SCIENCE

THAPAR INSTITUTE OF ENGINEERING AND TECHNOLOGY, PATIALA - 147004

PUNJAB, INDIA

JANUARY, 2024

Dedicated to My Family and Friends,
You are my strongest support.

THESIS CERTIFICATE

This is to certify that the thesis titled "**BINARY AND TERNARY DECAY DYNAMICS OF NUCLEAR SYSTEMS WITHIN FRAGMENTATION APPROACH**", submitted by **Mr. Nitin Sharma**, for the fulfillment of the requirements for the award of Degree of Doctor of Philosophy in the School of Physics and Materials Science, Thapar Institute of Engineering and Technology, Patiala, is a record of the candidate's own work carried out by her under my supervision. The matter presented in this thesis has not been submitted in part or full for the award of any degree in any other university or institute.

Supervisor

Manoj Kumar Sharma
Professor
School of Physics Materials Science
TIET, Patiala - 147004
Punjab, INDIA

Date: 04.01.2024

Place: Patiala

ACKNOWLEDGEMENTS

The journey of a tree from a tiny seed to large bunches full of green leaves and fruits is too hard and not an easy task. The conversion process of a seed to the plant and than to a tree is mainly due to the restless efforts of the Gardner. Similarly, in my PhD journey lots of people help me a lot. First of all, I thank to lord Krishna who give me support through the beautiful Srimad bhagvad-gita and many other scriptures. Without his blessings, this achievement would not have been possible. I would like to express my sincere gratitude to my esteemed supervisor Dr. Manoj K. Sharma, Professor, School of Physics and Materials Science, Thapar Institute of Engineering and Technology (TIET), Patiala, for the continuous support of my PhD study and research. His guidance helped me in all the time of research and writing of this thesis. I thank him personally for being such a wonderful and supportive supervisor. I express profound gratitude to Prof. Kulvir Singh, Head, School of Physics and Materials Science and Prof. N. Tejo Prakash, Dean of Research and Development Cell, TIET, Patiala, to provide me with all facilities to carry out this research work. I sincerely appreciate the whole hearted cooperation and valuable suggestions provided by Advisory Doctoral Committee comprising Dr. Sunil Devi, Dr. Alka Upadhyay and Dr. A. K. Lal. My sincere thanks also goes to all the staff of the School for their help and kind support. Special thanks To Dr. Amandeeep Kaur for his valuable support in my research work. I also express my heartfelt thanks to my seniors and lab mates Dr. Gudveen Sawhney, Dr. Neha Grover, Dr. Kanishka Sharma, Dr. Gurjit Kaur, Dr. Shivani Jain, Dr. Vishal Parmar, Shilpa Rana, Shubhpreet Kaur, Ashutosh Kaushik, Chahat Jindal, Harshit Sharma, Diksha Pathania, for their co-operation and encouragement. In our department, special thanks to Beant Kaur, Sangeeta, Nishu, Santosh, Ajit, Sudhanshu, Ankush, Rashmi For their support.

Again and again i am nothing without support of my parents (Mr. Devdutt Sharma and Anita Sharma), My sisters(Prerana and Komal), Manish Shukla and Anuj (brother-in-law), Anaya and Vedika (niece). Thank to you all for support.

Nitin S

(NITIN SHARMA)

ABSTRACT

The nuclei belonging to the heavy mass region are highly radioactive and may undergo different binary decay modes such as α decay, cluster radioactivity (CR), heavy particle radioactivity (HPR) and the spontaneous fission (SF). A radioactive nucleus may opt any of these decay modes and the disintegration process depends on different factors such as the shell effect, shape, size, deformation etc. In addition of these decay modes there exist a probability of three fragment emission, and the process is termed as ternary decay. The primary objectives of this work is to make a comparative analysis of different binary decay modes (α-decay, CR, HPR and SF), identification of the binary fission fragments and their comparison with the ternary fission fragments. In the present work, the binary decay analysis is carried out using preformed cluster model (PCM) and three cluster model (TCM) is employed to study ternary decay mechanism. The comparison of the binary decay modes is made using the fragmentation potential, preformation probability (P_0), penetration probability (P) and the assault frequency (ν). Similarly, the ternary fission analysis is carried out for the light and heavy third fragment accompanied fission modes. In view of the above, the present work is divided into eight chapters, and their brief description is given below:

In **Chapter 1**, historical background of the radioactivity and its importance in the modern time is described. The general radioactive decay modes such as α-decay,β-decay and gamma radiation emission are explained. In addition to this, other observed ground state decay modes such as the cluster radioactivity (CR), heavy particle radioactivity (HPR) and spontaneous fission (SF) are illustrated. After the exploration of the binary decay mechanisms, types of ternary decay mechanism and corresponding experimental and theoretical background is outlined. At the end of the chapter, the motivation of the present work and organisation of thesis is outlined.

In **Chapter 2**, the methodology adopted for the binary and ternary decay analysis is briefly discussed. First of all, the quantum mechanical fragmentation theory (QMFT) and related terms have been explained. After this, the QMFT based preformed cluster model (PCM) and three cluster model (TCM) are explained. In PCM, the fragmentation potential is

calculated, which in turn used for the identification of the most probable fission fragments. This potential is further used to calculate the preformation probability (P_0) of the decaying fragments. In addition to this, the penetration probability (P) of the probable decay channel is calculated as three step process using W.K.B. approximation. The classical and quantum mechanical view of the assault frequency (ν) is explained. Using the preformation probability (P_0), penetration probability (P) and the assault frequency (ν), the decay constant and decay half-lives are calculated. In TCM, two kind of geometrical arrangement (i.e. ECT and CCT) of three fragments are illustrated. The three body fragmentation potential is described where third fragment of the outgoing channel is kept fixed. The barrier penetration probability is calculated with respect to the surface separation of three fragments. The calculated penetrability further is uesed further to calculate the relative yield of the fragment combinations.

In **Chapter 3**, a comprehensive study of the alpha particle emergence from $^{188-218}$Po isotopes is carried out within the framework of the preformed cluster model (PCM). The barrier characteristics are studied using two choices of radii (with surface diffuseness (C_i) and without surface diffuseness(R_i)). The α decay is found to be most prominent decay mode in the chosen set of isotopes. The preformation and penetrative probability of the decay fragments is studied with respect to increase in the neutron number of the parent nucleus. The alpha decay half lives of Polonium are calculated using classical assault frequency (ν_c) and quantum mechanical assault frequency (ν_q) and a comparison is made with the experimental data. Further, the alpha decay half-lives of the $^{198-220}$ Rn isotopes are calculated using effective assault frequency (ν_e) parameter and a comparison is made with the available experimental data.

In **Chapter 4**, the binary decay analysis of the ^{253}Es radioactive nucleus is carried out using PCM. A comparative study of all probable radioactive decay modes such as α-decay, CR, HPR and SF etc. is carried outin terms of the fragmentation potential, preformation probability (P_0) and penetration probability (P). The fragmentation structure is explored using two kind of nuclear potentials , i.e., Yukawa plus exponential and proximity potential. The structure of the fragmentation potential and the location of potential minima are found to be independent of the choice of nuclear potential. The decaying fragments and their complementary fragments are found to lie near the shell closure. The decay half-lives ($T_1/2$) are calculated for all decay modes by the optimization of the neck length parameter

ΔR. The calculated half-lives of α decay and spontaneous fission find nice agreement with the experimental data. Also, the half-lives are predicted for cluster and heavy particle radioactivity, for which experimental verification would be of further interest.

In **Chapter 5**, the role of deformation and orientation in the spontaneous fission (SF) is explored using PCM. The SF analysis of even mass $^{242-260}$Fm isotopes is carried out and the mass distributions is explored. The deformation effects are included upto the quadrupole (β_2) deformed nuclei with optimum orientations ($\theta_i^{opt.}$) leading to hot-compact (side-to-side) and cold-elongated (tip-to-tip) configurations. The spherical and hot-compact deformed configurations of decay fragments result in the symmetric fragment mass distributions for Fm isotopes; however, the symmetric peak gets sharper with an increase in the neutron (N) number of the parent nucleus. In the case of cold orientations, a transition from two-peaked (asymmetric fission) to three-peaked (multimodal fission) mass distribution is observed with an increase in the mass number of Fm isotopes. The SF half-lives ($T_{1/2}^{SF}$) are calculated using the neck-length parameter (ΔR) for $^{242-260}$Fm isotopes and compared with the experimental data. Besides this, the induced fission of Fm isotopes is also studied within the dynamical cluster-decay model. The energy dependence of fission fragment mass distributions and the isotopic dependence is analyzed at energy range E^* = 5–42 MeV. In addition, the role of temperature-dependent deformations is also explored in the preview of the fission dynamics.

In **Chapter 6**, Light charge particle accompanied fission (ternary fission) mode of the ^{253}Es nucleus is explored using three cluster model (TCM). The calculations are performed using two kinds of nuclear potentials i.e. Yukawa plus exponential and proximity potential. The fragmentation structure is used for the identification of most probable fission fragment. The decay probability of the probable fission fragments seems relatively higher in case of the proximity potential. A comparison of the barrier characteristics for both nuclear potentials is made. In addition to this, comparison of the binary and ternary fission fragments is also carried out. The mass distribution for both kind of decay modes (binary and ternary) is studied and it is observed that the contribution of relative yield is higher in case of binary fission as compared to ternary fission. Further, the role of shell effects is analyzed in binary as well as ternary decay channel.

In **Chapter 7**, the ternary fission analysis of two Fm isotopes nuclei having atomic mass A_P = 242 and 258 is carried out using TCM. First, the choice of third fragment (A_3) is fixed by minimizing the probable A_3 fragments having different proton neutron configurations.

Further, the fission fragment combinations ($A_1 + A_2 + A_3$) are identified for the fixed third fragments by selecting the channel of lower ternary fragmentation potential and higher relative fission yield. Two type of tripartition of radioactive nuclei is considered, equatorial cluster tripartition (ECT) and collinear cluster tripartition (CCT). A comparative analysis of ternary fragmentation potential and relative fission yield within ECT and CCT geometrical arrangement is carried out for different choices of third fragment, i.e., $A_3 = 1$ to $A_P/3$. The choice of most probable fragments suggest that the proton and neutron magic shell closures play essential role in the ternary mass division. Finally, a relative analysis of binary and ternary fragmentation is worked out for better insight of the dynamics involved.

In the last chapter of the thesis **Summary**, the results related to the binary and ternary decay mechanisms are briefly summarized and the future scope of the present work is briefly outlined.

Contents

List of Tables

List of Figures

THESIS BASED PUBLICATIONS

In International Journals

1. "Analysis of various competing binary and ternary decay processes of the ^{253}Es nucleus"
   Nitin Sharma, Amandeep Kaur and Manoj K. Sharma
   Phys. Rev. C **102**, 064603 (2020)
   Impact Factor: *3.199*

2. "Effect of compact and elongated configurations on the spontaneous and induced fission of Fm isotopes"
   Amandeep Kaur, **Nitin Sharma** and Manoj K. Sharma
   Phys. Rev. C **103**, 034618 (2021)
   Impact Factor: *3.199*

3. "Ternary fission analysis of ^{242,258}Fm nuclei using equatorial and collinear cluster tripartition configurations"
   Nitin Sharma, Amandeep Kaur and Manoj K. Sharma
   Phys. Rev. C **105**, 044602 (2022)
   Impact Factor: *3.199*

4. "α decay of Po and Rn isotopes using different choices of impinging frequency"
   Nitin Sharma and Manoj K. Sharma
   Phys. Rev. C **106**, 034608 (2022)
   Impact Factor: *3.199*

5. "Decay Dynamics of ^{253}Ac* Nucleus Formed in ^{16}O- and ^{12}C-Induced Reactions at Above Barrier Energies "
   Nitin Sharma, Amandeep Kaur and Manoj K. Sharma
   Bulletin of the Russian Academy of Sciences: Physic **85**, 1486 (2021)[Not the part of the thesis]

6. "Binary and Ternary Fragmentation Analysis of ^{252}Cf Nucleus using Different Nuclear Radii"
   Nitin Sharma and Manoj K. Sharma
   J. Nucl. Phys. Mat. Sci. Rad. A.,**9**, 55 (2021)

7. "Sequential decay analysis of the ^{235}U(nth,f) reaction using a fragmentation approach",
   Nitin Sharma, Ashutosh Kaushik and Manoj K. Sharma
   Chinese Phys. C (under review)

8. "Study of various ground state decay mechanisms of Actinide nuclei",
   Chahat Jindal, **Nitin Sharma** and Manoj K. Sharma
   Chinese Phys. C **47**, 104108 (2023) [Not the part of the thesis]

National/International Conference Proceedings

1. "Probable spontaneous decay modes of ^{254}Es radioactive nucleus "
   Nitin Sharma, Amandeep Kaur and Manoj K. Sharma
   AIP Conf. Proc. **2352**, 0500441 (2020)

In National and International Conferences/Symposiums

1. "Study of (n,p) reaction on ^{78}Se nucleus using Collective clusterization approach"
   Nitin Sharma and Manoj K. Sharma
   23rd Punjab Science Congress (Feb.7-9, 2020), Sant longowal institute of engineering technology , Longowal (Punjab).

2. " Decay dynamics of ^{221}Ac* nucleus formed in ^{16}O and ^{12}C induced reactions at above barrier energies"
   Nitin Sharma, Amandeep Kaur and Manoj K. Sharma
   LXX international conference "Nucleus 2020. Nuclear physics and elementary particle physics. Nuclear physics technologies", Saint Petersburg University, Russia.

3. "Binary and ternary fragmentation analysis of ^{252}Cf nucleus using different nuclear radii"
   Nitin Sharma and Manoj K. Sharma
   "International conference on Theoretical aspects of nuclear physics". Central university of Himachal Pradesh , Dharamshala (India).

4. "Probable spontaneous decay modes of ^{254}Es radioactive nucleus"
   Nitin Sharma, Vishal Parmar, Amandeep Kaur and Manoj K. Sharma
   5^{th} National conference on advanced materials and radiation physics. Sant longowal institute of engineering technology, Longowal (Punjab).

5. "Cluster emission of ^{258,260}Fm nuclei using different sets of binding energies."
   Nitin Sharma and Manoj K. Sharma
   "International conference on HYPERFINE interactions and their applications". Brasov (Romania).

6. "Alpha decay of Polonium isotopes using different choices of assault frequency."
   Nitin Sharma, Amandeep Kaur and Manoj K. Sharma
   LXXI international conference "Nucleus 2021. Nuclear physics and elementary particle physics. Nuclear physics technologies", Saint Petersburg university, Russia."

7. "Analysis of cluster radioactivity using Q-value dependent relative separation"
   Chahat Jindal, **Nitin Sharma**,and Manoj K. Sharma
   LXXII international conference " Nucleus 2022" Saint Petersburg university, Russia.

8. "Fragmentation analysis of binary, ternary and quaternary fission of U and Fm isotopes"
   Chahat Jindal, **Nitin Sharma**,and Manoj K. Sharma
   DAE symposium on Nuclear Physics. 66 , 2022, Cotton university, Guwahati."

ABBREVIATIONS

CR	Cluster Radioactivity
HPR	Heavy Particle Radioactivity
SF	Spontaneous Fission
CAF	Classical Assault Frequency
QAF	Quantum Mechanical Assault Frequency
QMFT	Quantum Mechanical Fragmentation Theory
TKE	Total Kinetic Energy
ECT	Equatorial Cluster Tripartition
CCT	Collinear Cluster Tripartition
ASAFM	Analytical Super-Asymmetrical Fission Model
GLDM	Generalized Liquid Drop Model
UFM	Unified Fission Model
LCP	Light Charge Particle
TTF	True Ternary Fission
CYEM	Cubic Plus Yukawa Plus Exponential Model
SHE	Super Heavy Element
P-T	Projectile-Target

NOTATIONS

A	Mass Number of nucleus
Z	Charge Number of nucleus
N	Neutron Number of nucleus
T	Temperature
$\bar{R}$	Radius of curvature
α	Angle of rotation of radius vector
β	Deformation parameter
θ	Orientation of symmetry axis
ϕ	Azimuthal angle
$\triangle R$	Neck-length parameter
$Y_{\lambda}^{(0)}$	Spherical-harmonic function of axial-symmetric shapes
s_0	Minimum separation distance
η_A	Mass-asymmetry parameter
η_Z	Charge-asymmetry parameter
E_{CN}^{*}	Excitation energy of excited Compound Nucleus
$E_{c.m.}$	Center of mass energy
Q	Q-value of entrance-channel
Q_{eff}	Effective Q-value
ℓ	Angular momentum quantum number
μ	Reduced mass
I	Moment of inertia
R	Separation distance between two nuclei
V_B	Barrier height
R_B	Barrier position
R_a, R_b	Classical tunneling points

Chapter 1

INTRODUCTION

"*Have no fear of perfection : you will never reach it.* "

- Marie curie

1.1 An Overview

In modern times, human being is surrounded by numerous inventions and each of them acts as an initiator for the advancement of technology. An idiom has been in use for centuries i.e. "Necessity is the mother of invention", which means human necessities arise from time to time and attempts are made to achieve them by ethically acceptable means. The inventions act as an ingredient to convert the earth into a better place full of ease and comfort. Generally, it is observed that inventions are made when some new and unique observations are encountered. A simple and common observation may inaugurate a new field of science which may further help to solve different intricacies and earlier reported failures. The well known observation of Issac Newton i.e. falling of a apple from tree, triggered the idea of the gravitational force which holds the objects on the earth's surface and also keeps the planets in a particular orbit around the earth. Such an ordinary observation gave birth to the theory of gravitation which is being used by the scientists for the satellite launching, mass determination of the planets etc. Similarly, an accidental observation was made by Henri Becquerel in 1896, where excretion of some strange radiation were registered on the photographic plate [1]. The source of this radiation was found to be the Uranium salt. Initially, Becquerel expected that these radiations will exhibit same behavior as that of the X-rays, but his further observations clarified that they are distinct from X-rays. After the observation of these rays, Marie and Pierre Curie further identified three additional elements

i.e. Polonium, Thorium and Radium which exhibit same kind of radiations and consequently a new phenomenon called "Radioactivity" was introduced. This discovery gave a new path to nuclear scientists to explore the reason of the emission of such kind of radiation from radioactive elements. Numerous proposals were provided in support of the obtained results. In the queue of such proposals, Frederick Soddy and Ernest Rutherford gave the disintegration postulate, that the source of these distinct radiation is basically a radioactive element. According to them, the radiation is produced due to a disintegration process which gives birth to a new element as end product. Initially, two radioactive series were proposed by Soddy and Rutherford, where both of the series initiate from Uranium (U) and Thorium (Th) element and terminate with Lead (Pb) as end product (^{208}Pb, a doubly magic nucleus). After the idea of the radioactive disintegration, Frederick Soddy introduced the "isotopes" i.e. the atoms which are chemically identical but have different atomic weight. The identification of such isotopes was quite useful for the understanding of the formation of Radiation. The isotopes can be categorised in two forms i.e. stable isotopes and unstable isotopes. The stability factor depends on various properties associated with the atomic nucleus. The ratio of number of protons to the number of neutrons, the atomic number, the mass number and the deformation etc. The unstable isotopes are the radioisotopes which can be produced naturally or due to the result of artificial modification of the atom. One example of the natural radioisotope is the Uranium, as 99.3 percent of the naturally obtained uranium is U-238 and the other isotopes are less stable. An unstable atom gets stabilized by emission of some mass, energy or the radiation. Generally, the radioactive emission includes the emission of the alpha particle, beta particle and gamma radiations. The alpha particle is basically a helium nucleus having two proton, two neutrons composition and is considered as smallest stable nucleus. The alpha decay was observed initially by Ernest Rutherford, where the radiation was deflected by the magnetic field. Further, the theoretical description of the emergence of alpha particle was given by Gamow, where alpha particle is considered in a trapped state within the nucleus. The radioactive nucleus may also disintegrate via beta (β) particle emission. Beta decay is the radioactive mode where a proton within the nucleus can be altered into a neutron and vice-versa. These changes within the nucleus happen due to emission of beta particle, when the proton to neutron conversion takes place then the process is called $\beta+$ decay and for neutron to proton conversion, β- emission process takes place. The third type of emission is the gamma decay, where the excess energy of the

radioactive nucleus is emitted mostly in terms of electromagnetic energy. Hence, the above mentioned three decay modes are the modes chosen by the unstable isotopes to attain a stable configuration.

In spite of above mentioned decay modes, there are some exotic radioactive decay modes such as Cluster radioactivity (CR), heavy particle radioactivity (HPR) and the spontaneous fission(SF) [2–4, 6, 22] etc. The radioactive emission mode where the emitted fragment is heavier than the alpha particle is called the cluster radioactivity [7–9]. Till now, different clusters have been examined theoretically as well as experimentally. The other decay mode where the emitted fragment is heavier than the cluster is known as heavy particle radioactivity and the phenomena was introduced theoretically by D. N. Poenaru *et al.* [10, 11], an experimental verification is still awaited. Another emission mode where the emitted fragments have comparable size is known as the spontaneous fission [12]. In addition to these usual binary decay mechanisms, there is a probability of emission of three fragments from the radioactive nucleus and the process is termed as ternary fission [13]. Ternary fission is relatively complex phenomenon which is mainly observed in the heavy and super-heavy mass region. The probability of binary or ternary emission increases when one move towards heavy or super-heavy mass region. A brief description of different radioactive decay mechanisms is given below.

1.2 Radioactive Decay

The disintegration phenomena in which an unstable radioactive nucleus proceeds to approach a stable configuration via emission of mass, radiation or energy is known as radioactive decay or radioactivity. The radioactivity can be expressed in terms of the unit Becquerel, which is equivalent to one disintegration per second. The time interval taken by a radioactive nucleus to decay fifty percent of its initial mass is called half-life ($T_{1/2}$). This $T_{1/2}$ value is different for different radioactive elements. The process of radioactive disintegration mainly depends on the decay half-life of the nucleus and the process may proceed in form of a chain process, where a radioactive nucleus dissociates and attains number of configurations. Such kind of radioactive decay chain keeps operating until a stable configuration is achieved. Most of the time such kind of decay chains are observed in the actinides, for example, a decay chain is

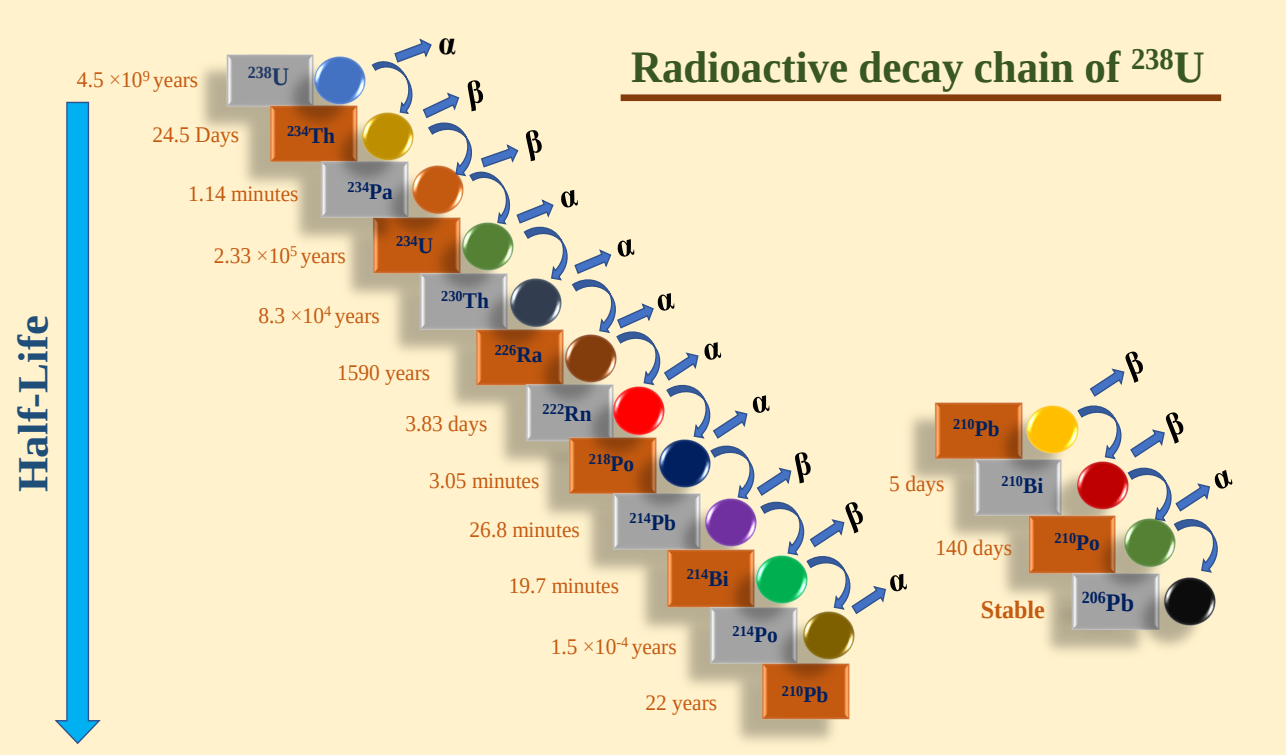

Figure 1.1: A schematic representation of radioactive decay chain initiates from ^{238}U nucleus and terminates at ^{206}Pb nucleus [14].

observed in ^{238}U nucleus and it undergo several disintegrations as shown in Fig.1.1. It can be noted that ^{238}U undergo different platform via emission of the alpha (α) particle, or beta (β) particles and finally the disintegration process terminates at stable lead (Pb) isotope. In such decay chains, formation of different nuclei takes place and the process acts as a natural production platform. The radioactive decay modes can be classified on the basis of mass and type of emitted fragments as shown in fig.1.2. The emission mode where the unstable parent nucleus splits into two fragments is known as binary decay mechanism and emission of three fragments is termed as ternary decay. The binary decay mechanism include α-decay, CR, HPR and SF. The ternary decay is a rare and complex emission mode where three fragment emission takes place and can be classified on the basis of the size of the third fragment. The three body decay mode where the third fragment is very light as compared to the two complementary decaying fragments is known as light charge particle (LCP) accompanied fission [15]. The decay mode where all the three fragments are of comparable size is known as true ternary decay process [16]. A brief analysis of binary and ternary decays is described below :

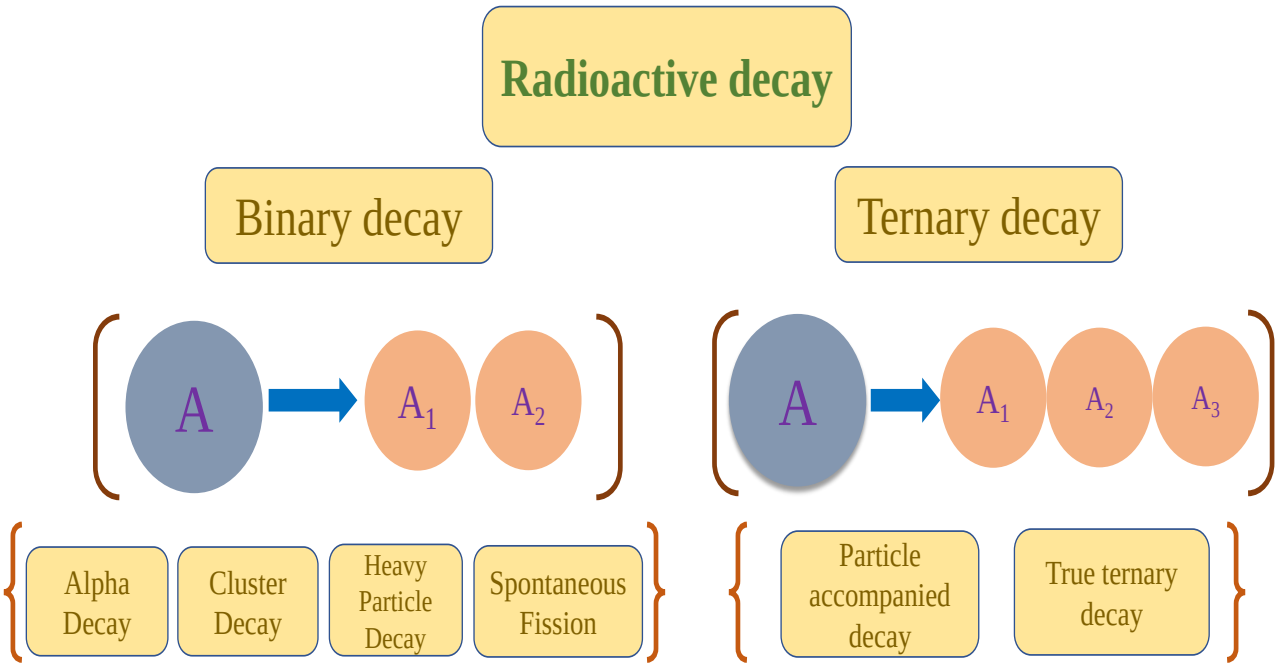

Figure 1.2: A schematic representation of various ground state decay mechanism evolved via binary and ternary decay path.

1.3 Binary decay

The radioactive splitting of the parent nucleus in two fragments is termed as binary decay. The binary decay is a common process and well known emission mode of the nuclei belonging to the periodic table. The probability of the binary emission is quite high as compared to multi-fragmentation processes. The most common experimental and theoretical observed binary decay modes are alpha (α) decay, CR, HPR and the SF. The α-decay is the process where a ^{4}He nucleus is emitted along with complementary fragment. When the emitted fragment lies in between the fission and alpha decay, the process is termed as cluster decay. In few theoretical descriptions, there is a probability of emission of fragments much heavier than cluster but lighter in comparison to the fission fragments, this process is termed as heavy particle radioactivity (HPR). Another possibility where decaying fragments are of comparable size is known as spontaneous fission (SF). In general, the most probable decay channel (anyone of the above mentioned mode) rely on the binding energy of nuclei and also

on the potentials acquire by the respective decay mode. In the present work an attempt is made to do a comparative analysis of such decay modes. The relevant explanation of these decay modes is given below:

1.3.1 Alpha decay

Alpha decay is the most observed radioactive decay mode where the radioactive nucleus disintegrates itself via emission of ^{4}He nucleus. Alpha disintegration was introduced by Ernest Rutherford, where these particles were treated as ionized helium atoms. After this description, George Gammow explained the α decay phenomenon as a tunneling effect, where alpha particle penetrates through a potential barrier. In the quantum mechanical description, alpha particle is considered as an independent cluster within the nucleus, that moves with a constant motion. The α particle holds within the core of the nucleus due to the interaction potential and also have a non-zero probability of penetration through the repulsive Coulomb barrier. The lower value of the penetration probability leads to higher value of decay half-life. Most of the time, alpha decay mode is observed as a common decay approach, and has higher decay probability as compared to other ground state decay channels (such as CR, HPR and SF etc.). Further, α decay also works as a decisive factor for the stability analysis of the nuclei belonging to heavy and superheavy mass regions. In nuclear chart, the alpha emission is mainly observed in the range Pb isotopes to the superheavy element Oganesson (Z=118) [17–23]. Additionally, few experimental attempts explored the continuous emission of the alpha particles near Z=50 [24]. The α decay chains are also observed in the superheavy mass region, where successive α emission happens and the process terminates with the spontaneous fission. Hence, alpha decay plays and important role in exploring the decay dynamics and the associated stability features of various nuclear systems.

Numerous experimental and theoretical attempts were performed to understand the radioactive emergence of the α particle [3, 25–32, 34–38]. Recently, experimental attempt [39] was made to study the isotopic behaviour of Ac isotopes during alpha particle emission and related alpha decay half-lives and decay energies were calculated. The odd-even staggering (ODE) is observed in the calculated α decay half-lives and given that the decay energies and the preformation factors play a crucial role in the staggering phenomenon. Another experimental attempt was made by Ognessian *et al.* [40] where α decay chains from $^{293,294}117$

and $^{294}118$ were observed, which eventually terminate via SF. In addition to this, some theoretical models are developed using different assumptions. The analytical superasymmetric fission model (ASAFM) was introduced by Poenaru et al. [41] where the decay half-lives are calculated using prescission and postscission stages. Using ASAFM the decay properties of 124 nuclei (which exhibit α decay experimentally) are studied and calculated outcomes are in accord with the experiment data [41]. The generalized liquid drop model (GLDM) [42] was also given where the macroscopic liquid drop energies play a key role to explore different decay properties associated with the α disintegration. GLDM is also employed in ref. [43], to study the alpha decay mechanism of 68 superheavy nuclei and the alpha decay half lives of $^{252-288}Rf$, $^{272-310}Fl$, $^{286-316}119$ and $^{292-318}120$ isotopes is extrapolated using Q-values obtained via WS4 and FRDM. Similarly, the preformed cluster model(PCM) is introduced, where α cluster is considered in a preformed state in the parent nucleus and the preformation yield is calculated using Schrodinger's equation i.e. based on mass-asymmetry dependent coordinate. Recently, PCM is employed [44] to study the α decay of Po and Rn isotopes using classical and quantum assault frequency and obtained outcomes are compared with the available experimental data. The α cluster is considered the lightest cluster mode as compared to other ground state decay mechanisms (i.e. CR, HPR and SF). The explanation of such mechanism is given in next subsections.

1.3.2 Cluster Radioactivity

In spite of the mostly observed α decay mode, another mode which is well established on theoretical and experimental platform is the cluster radioactivity (fragment heavier than the α particle). The process of emergence of the cluster from a radioactive parent nucleus is known as cluster radioactivity (CR). The first theoretical observation of the CR was made by Sandulescu *et al.* [45] using the fragmentation theory and this mode acts like a connector between the α decay and the spontaneous fission (SF). After the theoretical establishment, CR mode was experimentally explored by Rose and Jones [46], where ^{14}C was registered as a decaying fragment from ^{223}Ra nucleus. Similarly, different clusters of mass range A_2=14-34 (^{14}C,^{20}O,^{23}F,^{24}Ne,^{26}Ne, ^{28}Mg,^{30}Mg,^{32}Si,^{34}Si etc.) were detected experimentally [47]. Additionally, clusters lighter than ^{14}C, i.e. ^{10}Be and heavier than ^{34}Si (i.e.,^{46}Ar and ^{48}Ca) are also predicted in various theoretical attempts.

Different theoretical models are developed for the analysis of the cluster emergence from a radioactive parent nucleus. In some attempts like Unified fission model (UFM), the cluster is supposed to be in overlap region and the behaviour of the scattering potential is considered to be uniform throughout the overlapping region (beyond touching state). The decay half-lives are calculated by studying the overlapping region and the penetrating region [48]. In other view, cluster is supposed to be in a preformed state and the decay half -lives are calculated using the preformation probability and the barrier penetration probability. This approach is used in the preformed cluster model (PCM). PCM successfully explored the CR decay modes, for example one may see [49–51]. The results obtained are found in nice agreement with the experimental data. Till now, the cluster radioactivity mostly observed in the heavy mass region (Up to ^{252}Cf nucleus), but few theoretical attempts triggered that there is possibility of CR in heavy actinides and super-heavy mass region. Recently, the prediction of cluster decay from ^{253}Es nucleus is made [52] using PCM and the decay half-life of respective decay mode is calculated. The calculated results are compared with the Cubic plus Yukawa plus exponential model (CYEM) [56]. The relevant discussion of this work is made in chapter 4 of the present thesis. The other radioactive decay mode where the emitted fragments having size/mass heavier than the cluster is observed, termed as heavy particle radioactivity (HPR) and explained in the next section.

1.3.3 Heavy Particle radioactivity

In addition to the cluster radioactivity (A_2=14-34), prediction of another radioactive decay mode was made by D. N. Poenaru *et al.* [10, 11], which is known as heavy particle radioactivity (HPR). The theoretical predictions of HPR is made using ASAFM model, where the emitted fragment have mass heavier than usual cluster decay. In this analysis, first of all the decay half-lives for α decay and ^{14}C emission from ^{222}Ra is calculated and the obtained outcomes are found in accordance with experimental reference [47]. The calculated half lives for both decay modes is shorter as compared to other competing clusters (^{8}Be, $^{12,13}C$, ^{15}N and ^{16}O). When similar analysis is made for ^{288}114, α particle and ^{80}Ge cluster are registered with shorter half-lives as compared with other probable clusters [47]. In addition to this, clusters with Z>28 seem more probable along with alpha particle, and the process operated in heavy/super heavy mass region. Moreover, for Z=104-124, calculated

half-lives for HPR gives larger branching ratio [10,11] as compared to the α decay for heavier Super heavy nuclei. After the establishment of the HPR using ASAFM, the possibility of the heavy cluster emission (HPR) from $^{278}113$, $^{278-289}115$ and $^{293,294}117$ nuclei are studied using the preformed cluster model [53]. The decay half-lives are calculated for the probable heavy clusters suggested by the fragmentation structure. It is concluded that the deformation effects and the choice of the proximity potential play a crucial role in the clusterization process of the super heavy nuclei. Recently, generalized liquid drop model (GLDM) and 2001 formula [55] is employed by G. royer *et al.* [54] for the HPR analysis in the super heavy nuclei. The observed decay half-lives are found to be comparable with the alpha decay half-lives. In this calculation, $^{76-80}Zn$, ^{78}Ga,$^{72,74-76}Cu$, $^{69,71}Ni$ are observed as most probable clusters and their corresponding complementary fragments lie nearby ^{208}Pb nucleus. Recently, the prediction of heavy particle radioactivity from ^{253}Es nucleus is made [52] using PCM and the decay half-life of respective decay modes is calculated. The relevant discussion is made in chapter 4 of the present thesis. The other probable decay mode after the HPR is the spontaneous fission which is explained in the next section.

1.3.4 Spontaneous Fission

The radioactive decay mode where the emitted fragments are of comparable size is known as spontaneous fission (SF). This decay mechanism was first time observed by Georgy Flerov in 1940 [4] on ^{238}U isotope. After the establishment of this mechanism numerous experiments were performed and it was observed that numerous nuclei may undergoes the SF process. In nuclear chart, SF mechanism is observed mostly in heavy mass region (A $\geq$ 230). Different theoretical models are incorporated using various assumptions and many hidden phenomena are explored related to SF dynamics. Initially, the analysis have been made using liquid drop model (LDM) and concluded that the SF probability increases with increase in fissility parameter (Z^2/A) of the parent nucleus. The variation of the calculated Log$T_{1/2}$(yr) with the liquid drop model fissility parameter is shown in figure 1.3. It can be noted from the figure that the experimentally observed spontaneous fission probability increases with respect to increase in fissility parameter. In other view, the α decay chains are observed in super heavy mass region and the process terminates with the spontaneous fission.

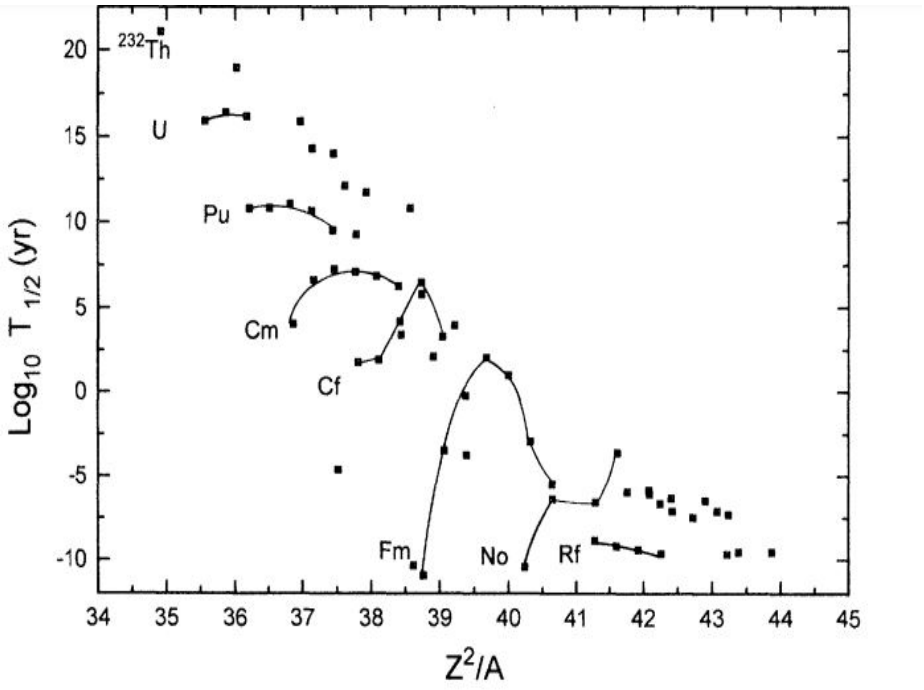

Figure 1.3: Variation of the spontaneous fission Log$T_{1/2}$(yr) as with respect to the fissility parameter of liquid drop model taken from [57]. All of these nuclei taken are the cases for which experimental observation of SF is obtained till now. The curves in the figure represents the even-even isotopes of several elements.

Randrup et al. [59] studied the SF dynamics for the doubly even nuclei with Z$\geq$ 92 using semi-classical WKB approach. In this work, effect of the axial symmetry and the reflection symmetry are included, which give decent inputs for the estimation of decay half-lives. In spite of the symmetry effects a multidimensional deformation space is included in ref [60] to explore the SF dynamics. Using this approach the decay half-lives of Z=102 and 104 is calculated, and concluded that the Sf half-life (T_{SF}) is shorter than alpha decay half-life (T_{α}). Additionally, calculated $T_{SF} \approx T_{\alpha}$ for a large number of isotopes (N=154-164). The generalized liquid drop model (GLDM) is employed in ref [61] to study the SF dynamics for nuclei Z=92-114, and calculated results are in accordance with experimental reference. The GLDM is further used to predict the T_{SF} for Z=114-120. The unified fission model (UFM) [62] is also used to calculate the T_{SF} and T_{α} for the nuclei belonging to super-heavy region, where microscopic shell correction and isospin effect based relations are proposed to calculate the decay half-lives. A competition between both decay modes (α and SF) is made using the calculated results and the decay half-lives are predicted for different unexplored nuclei [62]. In addition to this, role of preformation factor in SF mode is explored in ref [63] using the preformed cluster model (PCM). The mass distribution of nuclei is explored with respect to increase in N/Z ratio and asymmetric to symmetric transition is observed. The most probable fission fragments are identified using the potential energy surfaces and calculated T_{SF} is in accordance with the experimental results [64]. The PCM is further employed to study the SF dynamics of Fm isotopes by incorporating deformation and orientation effects [65]. In this work, transition from two peaked (asymmetric) to three peaked (Bimodal) Mass distribution is observed in case of the cold orientations. The relevant discussion is made in chapter 5 of the present thesis. In spite of these binary splitting modes there is a possibility of emission of three fragments, which is explained in the next section.

1.4 Ternary Decay

Generally, the radioactive decay modes comprise of emission of two fragments, but there is a complex and rare process where the radioactive parent nucleus may split into three fragments and the emission mode is known as ternary decay. First time, the experimental observation of the ternary decay was made by Alvarez et al [66], where alpha particle per

250 fission fragments was detected by irradiation of slow neutrons on ^{235}U nucleus. The three fragment emission is probable on both ground state as well as excited state. Different attempts were made to explore the ternary decay mechanism and the related dynamics. The terms related to the liquid drop model (LDM) have been employed by Swiatecki et al. [67], and given that the nuclei that lie in range $30.5 < Z^2/A < 43.3$ are more favourable for ternary fission. Most of the nuclei in this range belong to the heavy and superheavy mass region. Additionally, the fragmentation analysis (for ternary fission) of the decaying fragments was made by Poenaru *et al.* [68], and given that the main reason for three fragment emission is the is the proton or neutron shell closure associated with the decaying fragments. Further, the shape analysis of the nucleus during ternary fission was made in ref [69] and concluded that elongated configurations with two or three necks are more probable for the nuclei belonging to the heavy or superheavy region. Overall analysis of such attempts reveal that the probability of the binary or ternary fission events increases as one approaches towards the heavy mass region. Ternary fission can be classified on the basis of emission of the size of the third fragment. The decay mechanism where the third fragment is lighter as compared to other two fission fragments is known as light charge particle (LCP) accompanied decay and for heavy third fragment the mechanism is called true ternary decay. The description of these decay mechanisms is given below :

1.4.1 Light particle accompanied decay

The ternary decay mechanism where the third fragment is lighter as compared to other two decaying fragments is known as light particle accompanied decay [**?**, 70, 71, 73]. The third fragment in LCP decay mode may be a proton, Triton or an alpha particle. In general, α particle is registered mostly as third fragment in LCP decay mode in theoretical or experimental attempts. In heavy mass region, long range α particle are detected experimentally in the spontaneous fission of Pu, Cm and Cf isotopes [74–76]. It is concluded in these references that the emission probabilities of the α particle increases with increase in the fissility parameter. An experimental attempt was made to study long range α particle in spontaneous fission of ^{252}Cf [77] nucleus and it was suggested that the fission fragments energy -ratio distribution have great similarity for the binary and ternary splitting of a nucleus.

Additionally, dynamical model [78] was introduced to study the LCP formation process as a result of two random neck ruptures during the time interval about one single-particle period. Using this analysis new semi-classical expressions are given which are employed further to calculate the LCP yields and relative ternary fission probability. Similarly, three cluster model (TCM) [79–82] is given where the third fragment is kept fixed and the probable decaying fragments are identified by calculating the three body fragmentation potential. The TCM calculated observations are in accordance with the experimental reference [83, 84]. In chapter 6 of the present thesis, the LCP mode of ^{253}Es nucleus is studied using two kind of nuclear potentials i.e. Yukawa-plus and exponential and the proximity potentials, and the role of the shell closure in the most probable fission fragments is explored. In addition to the LCP mode, there is also a probability of true ternary fission (TTF) events where all three fission partners are of comparable masses. The explanation of the true ternary decay mechanism is given in the next section.

1.4.2 True ternary decay

In-spite of light third fragment (LCP mode), there is emission possibility of heavy third fragment along with two fission fragments and the respective decay mode is known as true ternary decay [85–89]. The experimental evidence for TTF was given by Mega et al. [90–92]. The mass of the light fragment in this experimental attempt is $30 < A < 70$ and the yield per binary fission is of the order of 10^{-5} and 10^{-6} for few nuclei belonging to the heavy mass region. Similarly, an experimental attempt was made to study decay mechanism of U^{236} nucleus and yield of mass $87 < A < 60$ is observed. Theoretical attempt was made by Greiner et al. [93], and concluded that heavy third fragment is more probable in case of superheavy nuclei. The main reason for such emission is shell closure effect and most probable two doubly magic Sn like structures. Similarly, the potential energy surfaces for TTF of ^{236}U and ^{252}Cf nucleus are explored in ref. [94] assuming pre-scission stage of three fragments arranged in a collinear state. The obtained minima in the PES give Ca, Fe, Ni, Ge and Se isotopes as probable heavy third fragments and lie nearby proton or neutron shell closures. This collinear arrangement is known as collinear cluster tripartition (CCT) and experimental attempt to observe this mode is made in ref [95], where two detectors are aligned at relative angle of 180^0. Two fragments of CCT mode are detected using the detectors and the third

fragment is obtained using missing mass method [95]. Different attempts were made to address the CCT mechanism using different formalisms. CCT mechanism is also considered as a sequential mechanism [96] which has a very short time between the ruptures of two necks, that makes a link between the middle fragment of the decay channel. In the first step, lower pre-scission barrier is produced and the heavier fragment decay happens in the next step. Additionally, the kinetic energy of the decaying fragments of the channel is calculated and the energy of the middle fragment is relatively low [97]. The theoretical investigation of the true ternary decay in the super-heavy nuclei was made by Zagrebaev et al. [98], and observed that the emission probability in the chosen region is high due to strong shell effects. In chapter 7 of the present thesis, the possible geometrical arrangement for true ternary decay mechanism is identified using the QMFT-based formalism. The collinear cluster tripartition (CCT) seems a suitable geometrical arrangement for both light and heavy third fragments. In the present work, an analysis of the LCP and true ternary decay mechanism is done using QMFT based approach, and the objectives of the work are outlined in the next section.

1.5 Motivation of the work

In present work, the nuclei belonging to heavy mass region of the nuclear chart are of interest, because most of them may proceed via any of the ground state decay modes (alpha decay, CR, HPR and SF etc.). One of the interesting property of such nuclei is that they can decay via one or multiple channels of the above mentioned decay modes. It will be of interest to make a comparative analysis of these decay modes using different parameters such as decay constant, preformation probability and barrier penetrability etc. For such analysis PCM is used where these radioactive decay modes are treated on parallel footing. In all these decay modes, α decay is the most observed decay mode. Hence, initially, α decay analysis is done using the diffuseness parameter and the role of neutron shell closure effects in α disintegration is explore. The alpha decay half-lives are calculated, which further depend on preformation probability, penetration probability and assault frequency etc. Role of these quantities is explored in view of alpha decay process. This work motivates me to study further heavier decay modes (CR,HPR and SF) and a comparative analysis of all these decay mode is worked out. In all of the above decay modes SF is considered as another

important decay mechanism where a radioactive nucleus splits into comparable size/mass. Additionally, the mass distribution of the radioactive nucleus can be easily identified using the SF dynamics. Hence, this work is focused on the SF mode where the decaying fragments are considered as spherical as well as deformed configurations. The mass distribution of different isotopes is explored using the cold orientation mode which is in good agreement with the experimental observed data.

In addition to the binary splitting, the nuclei belonging to the heavy mass region may divide into three fragments. Hence, the ternary decay mechanism is also investigated. The three body splitting phenomena is explored using three cluster model (TCM), where third fragment of the decay mechanism is kept fixed. The third fragment in ternary decay may be a light charge particle or a heavy particle. Most of the time, the light third fragment in the ternary decay mechanism is basically a α particle. This alpha particle is observed along with two heavy fission fragments. We are interested to identify the most probable decaying fragments along with this alpha particle. The most probable decaying fragments are identified by calculating the potential energy surface. It is of interest to analyse the relative emergence of ternary fragments with respect to the usually observed binary channel. Hence, the relative yield for both of binary and ternary decay modes are compared. There are two probable ternary configurations i.e. equatorial cluster tripartition (ECT) and collinear cluster tripartition (CCT). As a next step, comparative analysis of ECT and CCT mode is made for light and heavy third fragment. In this analysis, all the probable decaying channels are identified. The barrier characteristics of both of the decaying modes are compared. To give a systematic description of the above mentioned processes regarding the binary and ternary decay mechanisms, the present thesis is categorized according to the following objectives:

- Study of ground state decay mechanisms such as α emission, cluster emission and spontaneous fission etc.
- The study of ternary fission (particle accompanied fission) and identification of corresponding decaying fragments.
- Comparative analysis of fragmentation in binary and ternary decay mechanisms.
- The results will be compared with the available experimental data and an effort will

be made to explore the possibility of some relevant predictions.

The organization of present thesis on the basis of above said objectives is discussed in the following section. A pictorial representation of the outline of the thesis is shown in Fig.1.4.

1.6 Organisation of the Thesis

The organization detail of the present thesis is given below:

In **Chapter 2** of the thesis, different postulates and the formalism of the quantum mechanical fragmentation theory (QMFT) is explained. Using QMFT, preformed cluster model (PCM) and three cluster model(TCM) are developed which can be used for two and three body decay analysis respectively. The important terms related to PCM such as the fragmentation potential, and preformation probability are explained, which are further used for the binary fragment identification. The three step barrier penetration probability of the identified decay channel also explained. Additionally, the classical and quantum mechanical view of the impinging frequency is described. Beside this, formalism of TCM is explained where the fragmentation analysis is made using the three body potential energy surfaces (PES). The penetration probability of the decaying fragments is explained in terms of the surface separation of the decaying fragments in three body exit channel. The relative yield of the three body decay channel is described using the statistical relation.

In **Chapter 3**, α decay analysis of the Po isotopes is made nearby N=126. The isotopical behaviour of the preformation probability, penetration probability and the assault frequency is explored with respect to increase in neutron number. The half-lives of the α emission mode are calculated using classical and quantum mechanical description of the assault frequency. The effective assault frequency parameter is given and using such parameter the alpha decay analysis of Rn isotopes is carried out.

In **Chapter 4**, a comprehensive analysis of different ground state decay mechanisms (α decay, CR and HPR and SF) is made using PCM. The fragmentation structure is studied using two kind of nuclear potentials i.e. Yukawa plus exponential potential and proximity potential . The comprehensive emergence of the probable decaying decay modes is explored in terms of the fragmentation potential, preformation probability, penetration probability

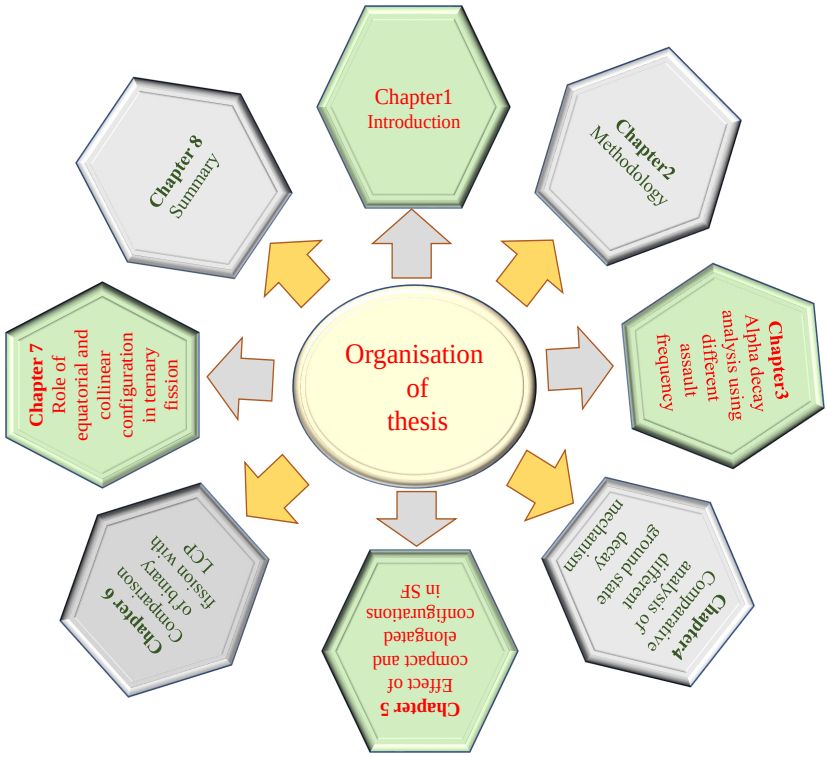

Figure 1.4: Pictorial representation of outline of thesis

and the decay half-lives.

In **Chapter 5**, SF analysis of even-even Fm isotopes is carried out by including deformation effects up to the quadrupole (β_2) deformed nuclei with optimum orientations (θ_i^{opt}) leading to hot-compact (side-to-side) and cold-elongated (tip-to-tip) configurations. The mass distribution of the Fm isotopes is studied with respect to increase in neutron number (N) of the parent nucleus. Role of shell closure effect have been explored in the mass distribution. In addition to this, the excitation energy dependence on the fission fragment mass distributions is analyzed.

In **Chapter 6**, an effort is made to explore the possibility of ternary fission (particle accompanied fission) using three cluster model (TCM). The fragmentation analysis is made using Yukawa plus exponential potential and proximity potentials to have synergy arround binary and ternary decay. The barrier penetration probability is calculated using the surface separation of the decaying fragments. The relative yield of the binary and ternary fission is compared and concluded that binary decay mode is more probable as compared to ternary decay mechanism.

In **Chapter 7**, the ternary fission analysis is made by calculating three body fragmentation potential. The choice of third fragment (A_3) is fixed by minimizing the probable

A_3 fragments having different proton neutron configurations. The most probable decaying fragments are identified for equatorial cluster tripartition (ECT) and collinear cluster tripartition (CCT). A comparative analysis of barrier characteristics of ECT and CCT decay mode is made with respect to the surface separation among the decaying fragments.

At the end, **Chapter 8** gives a brief note on the work done in reference to the objectives of the present thesis along with the future possibilities that arise from the established results.

Bibliography

[1] H. Becquerel, Compt. Rend. **122**, 420 (1896).

[2] E. Hourani *et al.*, Ann. Phys. (Paris) **14**, 311 (1989).

[3] D. N. Poenaru *et al.*, Europhys. Lett. **118**, 22001 (2017).

[4] D. N. Poenaru and R. A. Gherghescu, Phys. Rev. C **94**, 014309 (2016).

[5] Y. Z. Wang *et al.*, Phys. Rev. C **92**, 064301(2015).

[6] P Siwach, P. Arumugam, S. Modi, L. S. Ferreira, and E. Maglione, Phys. Rev. C **105**,L031302 (2022).

[7] H. J. Rose and G. A. Jones, Nature (London) **307**, 245 (1984).

[8] A. S˘andulescu, D. N. Poenaru, and W. Greiner, Sov. J. Part. Nucl. **11**, 528 (1980).

[9] R. Bonetti and A. Guglielmetti, Rom. Rep. Phys. **59**, 301 (2007).

[10] D.N. Poenaru, R.A. Gherghescu, W. Greiner, Phys. Rev. Lett. **107**, 062503 (2011).

[11] D.N. Poenaru, R.A. Gherghescu, W. Greiner, Phys. Rev. C **85**, 034615 (2012).

[12] K. Sharma *et al.*, Phys. Rev. C **96**, 054307 (2017).

[13] L. W. Alvarez *et al.*, Phys. Rev. **71**, 327 (1947).

[14] J. Perez-Perez *et al.*, Universe **8**, 112 (2022).

[15] A.J. Kordyasz *et al.*, Nucl. Phys. A. **439**, 88 (1985).

[16] A. V. Karpov , Phys. Rev. C **94**, 064615 (2016).

[17] D. N. Poenaru *et al.*, J. Phys. G: Nucl. Part. Phys. **32**, 1223 (2006).

[18] A. Staszczak, A. Baran, and W. Nazarewicz, Phys. Rev. C **87**, 024320 (2013).

[19] D. N. Poenaru and R. A. Gherghescu, J. Phys. G: Nucl. Part. Phys.**41**, 125104 (2014).

[20] D. N. Poenaru *et al.*, Eur. Phys. J. A **54**, 14 (2018).

[21] H. B. Yang *et al.*, Phys. Rev. C **105**, L051302 (2022).

[22] A. N. Bezbakh, G. G. Adamian, and N. V. Antonenko, Phys.Rev. C **105**, 054305 (2022).

[23] K. P. Santhosh, T. A. Jose, and N. K. Deepak, Phys. Rev. C **105**, 054605 (2022).

[24] L. Capponi *et al.*, Phys. Rev. C **94**, 024314 (2016).

[25] D. N. Poenaru and W. Greiner, Handbook of Nuclear properties, (clarendon press, Oxford) (1996).

[26] D. N. Poenaru , Nuclear decay modes, (Institute of Physics Publishing, Bristol) (1996).

[27] D. N. Poenaru et al.,J. Phys. G: Nucl. Part. Phys. **32**, 1223 (2006).

[28] D. T. Akrawy et al., Nucl. Phys. A **1021**, 122419 (2022).

[29] H. B. Yang et al., Phys. Rev. C **105**, L051302 (2022).

[30] A. N. Bezbakh, Phys. Rev. C **105**, 054305 (2022).

[31] K. P. Santosh et al., Phys. Rev. C **105**, 054605 (2022).

[32] D. N. Poenaru et al., Computer Physics Communications **25**, 297 (1982).

[33] D. T. Akrawy, D. N. Poenaru J. Phys. G: Nucl. Part. Phys. **44**, 105105 (2017).

[34] D. N. Poenaru et. al., Eur. Phys. J. A,**54**, 14 (2018).

[35] D. N. Poenaru and R. A. Gherghescu, Phys. Rev. C **97**, 044621 (2018).

[36] K. Varga et. al., Phys. Rev. L **69**, 37 (1992).

[37] I. Ahmad et al., Phys. Rev. C **8**, 2 (1973).

[38] D. N. Poenaru and R. A. Gherghescu , Eur. Phys. L **124**, 52001 (2018).

[39] H. B. Yang *et al.*, Phys. Rev. C **106**, 064311 (2022).

[40] Y. T. Oganessian *et al*, Phys. Rev. Lett. **109**, 162501 (2012).

[41] D. N. Poenaru and W. Greiner, Phys. Scr. **44**, 427 (1991).

[42] G. Royer and R. A. Gherghescu, Nucl. Phys. A **699**, 479 (2002).

[43] N. N. Ma *et al*, Chin. Phys. C **45**, 024105 (2021).

[44] N. Sharma and M. K. Sharma, Phys. Rev. C **106**, 034608 (2022).

[45] A. Sandulescu, D. N. Poenaru and W. Greiner, Sov. J. Nucl. **11**, 528 (1980).

[46] H. J. Rose and G. A. Jones, Nature (London) **307**, 245 (1984).

[47] R. Bonetti, A. Guglielmetti, Rom. Rep. Phys. **59**, 301 (2007).

[48] D. N. Poenaru and W. Greiner, Physica Scripta. **44**, 427, (1991).

[49] K. Sharma and M. k. Sharma, Int. J. Mod. Phys. E **28**, 1950048 (2019).

[50] N. Kaur, R. Kumar and M. K. Sharma, Eur. Phys. J A **56**, 35 (2020).

[51] Rajni, G. Sawhney and M. k. Sharma, Phys. Rev. C **106**, 044605 (2022).

[52] N. Sharma *et al.*, Phys. Rev. C **102**, 064603 (2020).

[53] G. Sawhney *et al.*, Eur. Phys. J. A **50**, 175 (2014).

[54] G. Royer *et al.*, Nucl. Phys. A. **1021**, 122427 (2022).

[55] G. Royer *et al.*, Nucl. Phys. A. **683**, 182 (2001).

[56] G. M. Carmel, V. Bai, and R. N. Agnes, Pramana J. Phys. **88**, 43 (2017).

[57] R. Bonetti *et al.*, Phys. Rev. C **51**, 5 (1995).

[58] G. N. Flerov and K. A. Petrzhak, Phys. Rev. **58**, 275 (1940).

[59] J. Randrup *et al.*, Phys. Rev. C **13**, 229 (1976).

[60] R. Smolanczuk *et al.*, Phys. Rev. C **52**, 4 (1995).

[61] Xiaojun Bao *et al.*, Nucl. Phys. A **906**, 1 (2013).

[62] X. J. Bao *et al.*, J. Phys. G: Nucl. Part. Phys. **42**, 085101 (2015).

[63] K. Sharma *et al.*, Phys. Rev. C **96**,054307 (2017).

[64] N. E. Holden and D. C. Hoffman, Pure Appl. Chem.**72**, 1525 (2000).

[65] A. Kaur, N. Sharma and M. K. Sharma, Phys. Rev. C **103**, 034618 (2021).

[66] L. W. Alvarez, as reported by G. Farewell, E. Segre, and C. Wiegand, Phys. Rev. **71**, 327 (1947).

[67] W.J. Swiatecki, Proceedings of the Second UN Conference on the Peaceful Uses of Atomic Energy, Geneva, **71** (United Nations, Geneva, 1958) 651,(1958).

[68] D.N. Poenaru *et al.*, Phys. Rev. C **59**, 3457 (1999).

[69] V.M. Strutinsky *et al.*, Nucl. Phys. A **46**, 639 (1963).

[70] N.N. Ajitanand *et al.*, Nucl. Phys. A **246**, 505 (1975).

[71] N. Feather, Phys. Rev. **170**, 4 (1968).

[72] H. Hongyin *et al.*, Nucl. Phys. A **615**,162 (1997).

[73] V. Andreev, G.G. Adamian, N.V. Antonenko, S.P. Ivanova, S.N. Kuklin, and W. Scheid Eur. Phys. J A **30**,579 (2006).

[74] P. Fong, Phys. Rev. **3**, 5 (1971).

[75] O. Soret *et al.*, Nucl. Phys. A **641**,34 (1998).

[76] s. vermote *et al.*, Nucl. Phys. A **806**,1 (2008).

[77] Z. Fraenkal, Phys. Rev. **156**, 4 (1967).

[78] V. A. Rubchenya and S. G. Yavshits, Z. Phys. A **329**, 217 (1988).

[79] K. Manimaran and M. Blasubramaniam, J. Phys. G **37**, 045104 (2010).

[80] K. Manimaran and M. Blasubramaniam, Eur. Phys. J. A **45**, 293 (2010).

[81] K. Manimaran and M. Balasubramaniam, Phys. Rev. C **79**, 024610 (2009).

[82] K. Manimaran and M. Balasubramaniam, Phys. Rev. C **83**, 034609 (2011).

[83] A. V. Ramayya, *et al.*, Phys. Rev. Lett. **81**, 947 (1998).

[84] A. V. Ramayya, *et al.*, Phys. Rev. C **57**, 2370 (1998).

[85] R. H. Iyer and J. W. Cobble, Phys. Rev. **172**, 1186 (1968).

[86] L. Rosen and A. M. Hudson, Phys. Rev. **78**, 533 (1950).

[87] R. L. Fleischer, P. B. Price, R. M. Walker, and E. L. Hubbard, Phys. Rev. **143**, 943 (1966).

[88] V. P. Perelygin, N. H. Shadieva, S. P. Tretyakova, A. H. Boos, and R. Brandt, Nucl. Phys. A **127**, 577 (1969).

[89] H. J. Becker, P. Vater, R. Brandt, and A. H. Boos, Phys. Lett. B **50**, 445 (1974).

[90] M. L. Muga, H. R. Bowman, and S. G. Thompson, Tripartition in the spontaneous-fission decay of Cf252, Phys. Rev. **121**, 270 (1961).

[91] M. L. Muga, in Proceedings of the IAEA Symposium on Physics and Chemistry of Fission, Salzburg, Vienna (IAEA, Vienna, 1965), Vol. 2, p. 409.

[92] M. L. Muga and C. R. Rice, in Proceedings of the Second IAEA Symposium on Physics and Chemistry of Fission, Salzburg, IAEA, Vienna (IAEA, Vienna, 1969), p. 107.

[93] V. I. Zagrebaev, A. V. Karpov, and Walter Greiner, Phys. Rev. C **81**, 044608 (2010).

[94] A. K. Nasirov *et al.*, Phys. Scr. **89**, 054022 (2014).

[95] Yu. V. Pyatkov *et al.*, Eur. Phys. J. A. **45**, 29 (2010).

[96] R. B. Tashkhodjaev *et al.*, Phys. Rev. C **91**, 054612 (2015).

[97] K. R. Vijayraghavan *et al.*, Eur. Phys. J. A. **48**, 27 (2012).

[98] V. I. Zagrebaev *et al.*, Phys. Rev. C **81**,044608 (2010).

Chapter 2

Methodology

2.1 Introduction

In the previous chapter, the historical background of the probable radioactive decay modes (i.e. the α decay, the Cluster decay, heavy particle decay, and spontaneous fission, etc.), and their importance and relevance has been discussed. Numerous attempts were made to explore these decay modes by introducing various experimental probes and theoretical formalisms, but the radioactive decay mechanism is still a Conundrum for the scientists working in this area. A radioactive nucleus can split into two or three fragments and the splitting process depends on different factors such as shell effect, deformation, orientation, and the fissility parameter, etc. associated with the nucleus and its corresponding decaying fragments. The comparative study of all the aforementioned spontaneous decay modes is of interest, as a nucleus may proceed to decay via any one of these decay modes. A number of theoretical attempts were made to overcome the intricacy of the spontaneous decay modes, but certain aspects are still not fully understood. Such most probable decay modes among all competing processes may be explored if a formalism is applied where the decay modes are treated at a parallel platform. Hence, in this work effort is made to explore these modes using collective clusterization approach, where all the probable decay modes are treated on parallel footing. The present chapter includes the description of theoretical formalism, which is employed for the binary and ternary fragmentation analysis of the radioactive nucleus. The binary decay analysis is made with the help of preformed cluster model (PCM) [1, 2] and the ternary decay mechanism is explored using the three cluster model (TCM) [3, 4]. Both of these models are inherited from the quantum mechanical fragmentation theory (QMFT) [5–7].

The QMFT works out in terms of mass/charge asymmetry coordinate (which behave as a dynamical collective fragmentation coordinate) [8–12]. Apart from this, some other coordinates are also uesd *i.e.* : (i) the relative separation among the decaying fragments (R), (ii)

the neck parameter, (iii) the azimuthal angle between the principal planes of the interacting fragments and (iv) the deformations and orientation of the nuclei. The postulates of the QMFT are further used for the establishment of the PCM and TCM which are discussed in upcoming sections:

2.2 Preformed cluster model

The binary decay analysis in this work is made using preformed cluster model (PCM) [13–16]. In PCM, the cluster is supposed to be in a preborn state within the parent nucleus and the cluster core interplay is explored using the mass asymmetry coordinates and the relative separation distance. All different ground state decay mechanisms (α decay, CR, HPR and SF) are successfully addressed by PCM in past years [17–19]. In PCM, different coordinates are employed to explore various properties associated with the ground state decay dynamics. These coordinates are employed to give the preformation probability of the decaying fragments, which in turn serves as an important tool for the estimation of the decay half-life, the decay constant, etc. The stability analysis of a radioactive nucleus depends on the decay constant, which is the product of preformation probability, penetration probability, and the barrier assault frequency. The decay constant (λ) is used to calculate the decay half-life $T_{1/2}$ of the nucleus with respect to probable decay mode using the relation

$$T_{1/2} = \frac{ln2}{\lambda}, \lambda = \nu P_0 P. \tag{2.1}$$

Here, ν and P_0 are the barrier assault frequency and the preformation probability respectively, and P refers to the penetration probability (R-motion). The assault frequency can be calculated using the classical or quantum mechanical view, the preformation probability is calculated by solving Schrödinger equation in η-coordinate and the penetration probability is calculated using the WKB approximation. The identification of the probable decay channels is made in view of the structural variations in the fragmentation potential. The description of various term used in the analysis is given below:

2.2.1 Fragmentation Potential

One of the important ingredient of PCM is the fragmentation potential $V_R(\eta)$, which helps for the identification of the most probable decay channel. The radioactive nucleus may have multiple possibilities of disintegeration in the exit channel, and it may split into any of these combinations. It is very difficult to identify the probable decay modes and this can be understood in terms of the fragmentation potential. The minima of the fragmentation potential correspond to the most probable decay channel. The fragmentation potential can be expressed as:

$$V_R(\eta) = - \sum_{i=1}^{2} B(A_i, Z_i) + V_C(R, Z_i, \beta_{\lambda i}, \theta_i) + V_N(R, A_i, \beta_{\lambda i}, \theta_i) \tag{2.2}$$

The first term in above expression is the binding energies of the decaying fragments. In present work the Binding energies are taken from the experimental observations of the Audi and wapstra [20] and the theoretical identified values from Moller *et al.* [21,22] (wherever the experimental results are not available). The second term in the expression is the Coulomb potential, which gives information regarding the repulsive force that acts between the two interacting nuclei. The decaying fragments can be considered in the spherical state or in deformed state, for the spherical choice of the decaying fragments the Coulomb potential can be written as

$$V_c(Spherical) = \frac{Z_1 Z_2 e^2}{R} \tag{2.3}$$

Here, the Z_i's represent the proton numbers of the interacting nuclei. When the decaying fragments are considered as deformed, then the above expression reads as [23–25]

$$V_C(Z_i, \beta_{\lambda i}, \theta_i, \alpha_i) = \frac{Z_i Z_j e^2}{R} + 3 Z_i Z_j e^2 \sum_{\lambda, i=1,2} \frac{1}{2\lambda+1} \frac{R_i^{\lambda}(\alpha_i)}{R^{\lambda+1}} Y_{\lambda}^{(0)}(\theta_i) \left[\beta_{\lambda i} + \frac{4}{7} \beta_{\lambda i}^2 Y_{\lambda}^{(0)}(\theta_i) \right] \tag{2.4}$$

In the above expression, α_i is the angle between the symmetry axis and the radius vector $R_i(\alpha_i)$ of the interacting nuclei and θ_i represents the angle between symmetry axis and the fission axis. The detailed description can be seen in ref [26]. The third term in the expression

is the nuclear potential. The nuclear potential gives information about the attractive force among the decaying fragments. There are numerous choices of the nuclear potential in the literature, but in present work we have used the Yukawa plus exponential potential [27] and the nuclear proximity potential [28].

Yukawa plus exponential potential

The Yukawa plus exponential potential is a short range nuclear potential. This potential can be expressed as [27]

$$V_{Yij} = -4\left(\frac{a}{r_0}\right)^2 \sqrt{a_{2i}a_{2j}}[g_i g_j(4+\xi) - g_j f_i - g_i f_j]\frac{exp(-\xi)}{\xi} \tag{2.5}$$

where $\xi = R^s_{ij}/a$, and the functions g and f are

$$g_k = \zeta cosh\zeta - sinh\zeta \tag{2.6}$$

and

$$f_k = \zeta^2 sinh\zeta, \tag{2.7}$$

where $\zeta = R_k/a$ with the radius of the nucleus being $R_k = r_0 A_k^{1/3}$. Here a=0.68 is the diffusivity parameter and the asymmetry parameter is $a_{2k} = a_s(1 - \omega I^2)$ with a_s=21.13 MeV, ω=2.3, and $I = \frac{N-Z}{A}$.

In addition to this potential, present work includes the proximity potential. The proximity potential has been proposed by Blocki et al. [28], where the interaction between the nuclear surfaces is estimated, when they are in close proximity with each other. It is believed that the potential among the two close surfaces is in proportion to the interaction potential per unit area between two flat surfaces. Till now, various nuclear proximity potentials have been proposed. In the present work two proximity potentials i.e. Prox77 and Prox00 are used.

Proximity 1977 (prox77)

The expression for prox77 is

$$V_{Pij}(s) = 4\pi\overline{R}\gamma b\Phi(s). \tag{2.8}$$

where, s is the surface separation of fragments, γ=0.9517[1-1.7826 $(N-Z/A)^2$] MeV fm^{-2}, the surface energy constant and b=0.99 is the nuclear surface thickness. $\overline{R}$ is the mean curvature radius and Φ is the universal function which can be expressed as

$$\phi(s) = \begin{cases} -\frac{1}{2}(s-\xi_0)^2 - 0.0852(s-\xi_0)^3; s \leq 1.2511 \text{ fm} \\ -3.437 \exp\left(-\frac{s}{0.75}\right); s > 1.2511 \text{ fm} \end{cases} \tag{2.9}$$

for more details, see ref. [28]).

Proximity 2000 (prox00):

The other nuclear potential which is used in the present work is the proximity 2000 (called as prox00) [29, 30]. In this potential the nuclear radii and surface charge coefficients are given using the well known droplet model concept. The expression for this potential is identical as prox77, but the related terms have been changed which are described below:

$$V_P = 4\pi\overline{R}\gamma b\Phi(\xi). \tag{2.10}$$

The radius expression R_i reads as

$$R_i = c_i + (N_i/A_i)t_i, \tag{2.11}$$

where c_i denotes half density radii of the charge distribution and t_i represents the neutron skin of the mother nucleus. The nuclear charge radius R_{00} (fm) be given as

$$R_{00i} = \sqrt{\frac{5}{3}} < r^2 >^{1/2} \tag{2.12}$$

$$= 1.240 A_i^{1/3} \left(1 + \frac{1.646}{A_i} - 0.191\frac{A_i - 2Z_i}{A_i}\right). \tag{2.13}$$

The half density radius c_i can be obtained from the relation [29]

$$c_i = R_{00_i}\left(1 - \frac{7}{2}\frac{b^2}{R_{00_i}^2} - \frac{49}{8}\frac{b^4}{R_{00_i}^4} + ...\right). \tag{2.14}$$

The neutron skin t_i is given as [29]

$$t_i = \frac{3}{2} r_0 \frac{JI_i - \frac{1}{12} c_1 Z_i A_i^{-1/3}}{q + \frac{2}{4} J A_i^{-1/3}}, \tag{2.15}$$

where r_0=1.4 fm, the energy constant J=32.65 MeV, the constant c_1=$(3/5)(e^2/r_0)$=0.757895 MeV and the neutron skin stiffness coefficient q=35.4 MeV. The nuclear surface energy coefficient γ in terms of neutron skin can be written as

$$\gamma = \frac{1}{4\pi r_0^2} \left[18.63(MeV) - q \frac{t_1^2 + t_2^2}{2 r_0^2} \right] \tag{2.16}$$

where t_1 and t_2 can be calculated using Eq. (2.15), and the universal function can be written as

$$\phi(\xi) = \begin{cases} -0.1353 + \sum_{i=0}^{5} \frac{c_n}{n+1} (2.5 - \xi)^{n+1}; \ 0 < \xi \leq 2.5 \\ -0.09551 exp[\frac{2.75 - \xi}{0.7176}]; \ \xi \leq 2.5 \ , \end{cases} \tag{2.17}$$

where $\xi = R - R_i - R_j$. The c_n constant values are : c_0=-0.1886, c_1=-0.2628, c_2=-0.15216, c_3=-0.04562, c_4=0.069136, c_5=-0.011454.

2.2.2 Preformation probability

With the help of the fragmentation potential $V_R(\eta, T)$, the preformation yields $P_0(A_i)$ of decaying fragments (A_i) is calculated using the Schrödinger equation in terms of the η-coordinate at fixed $R = R_a$,

$$\left\{ -\frac{\hbar^2}{2\sqrt{B_{\eta\eta}}} \frac{\partial}{\partial \eta} \frac{1}{\sqrt{B_{\eta\eta}}} \frac{\partial}{\partial \eta} + V_R(\eta, T) \right\} \psi^{\nu}(\eta) = E^{\nu} \psi^{\nu}(\eta), \tag{2.18}$$

with $\nu = 0, 1, 2, 3...$ referring to ground state ($\nu = 0$) and excited state solutions, with the ground state preformation probability P_0 given as

$$P_0 = |\psi(\eta(A_i))|^2 \sqrt{B_{\eta\eta}} \frac{2}{A_{CN}}, \tag{2.19}$$

The higher values of ν contribute for excited states, and these contributions enter via excitation of higher vibrational states. For these excited states the wave function reads as

$$|\psi|^2 = \sum_{\nu=0}^{\infty} |\psi^\nu|^2 exp(-E^\nu/T). \tag{2.20}$$

In the present formalism, the temprature effects are incorporated for the excited state analysis where as these effects remains silent for the ground state mechanism. Majority of the work in the present thesis is done at T=0 MeV. The preformation probability (P_0) is the probability to find certain mass fragments at position R on the decay path, and is calculated using collective clusterization approach. The term $B_{\eta\eta}$ in Eq. 2.18 and 2.19 represents the mass parameter [31] given by Kroger and Scheid. This parameter depict the hydrodynamical flow and mathematically can be written as:

$$B_{\eta\eta} = \frac{AmR^2}{4}\left[\frac{\nu_t(1+\gamma)}{\nu_c(1+\delta^2)} - 1\right] \tag{2.21}$$

The detailed description can be seen in the ref. [31–33]. After the η-motion, the R-motion analysis is made by calculating the penetration probability (P) of the decay channel and it's explanation is given in the next section:

2.2.3 Penetration probability

In PCM, penetration probability P is three step process and obtained from Wenzel-Kramers-Brillouin (WKB) integral, and calculated using [34]

$$P = P_a W_i P_b. \tag{2.22}$$

The transmission probability consists of three contributions as shown in Fig. 2.1,

(i) the penetrability P_a from R_a to R_i

$$P_a = exp[-\frac{2}{\hbar}\int_{R_a}^{R_i}\{2\mu[V(R) - V(R_i)]\}^{1/2}dR], \tag{2.23}$$

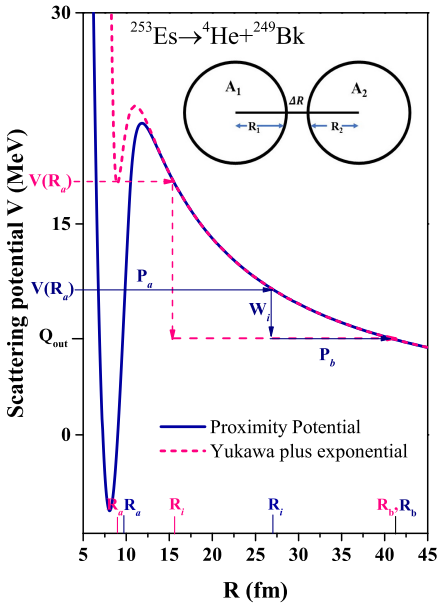

Figure 2.1: The binary scattering potential V(R) (calculated as sum of Coulomb and nuclear potentials) for the α-decay of ^{253}Es nucleus for two kind of nuclear potentials, i.e., Yukawa plus exponential and proximity potentials. The three stages of the penetration process are also shown in figure.

(ii) the inner de-excitation probability W_i at R_i (and is taken to be unity [34]),

$$W_i = exp(-BE_i), \tag{2.24}$$

(iii) the penetrability P_b from R_i to R_b

$$P_b = exp[-\frac{2}{\hbar}\int_{R_i}^{R_b}\{2\mu[V(R)-Q]\}^{1/2}dR]. \tag{2.25}$$

The de-excitation probability W_i is taken from the excitation model of Greiner *et al.* [34]. In Eq. 2.24, E_i represents the energy of excitation of the daughter nucleus, which is basically the energy difference between V(R_i) and the Q value of the decay products. At this point, the excitation of the daughter nucleus is a consequence of nuclear and Coulomb interactions of the decaying fragments [34]. Furthermore, if parameter B of Eq.2.24 was allowed to depend on R_i (see Fig. 2 of Ref. [34]), then the process may proceed towards multiple de-excitations and move as a step-like process. In the present work, the de-excitation of the daughter nucleus is constrained to only a solo transition. Here, parameter B is taken to be negligibly small which means that the excitation of the decay fragments plays a minor role,

and hence $W_i = 1$. The first turning point R_a is defined as $R_a = R_1 + R_2 + \triangle$R. Here R_1, R_2 are radii of the decaying fragments. $\triangle$R is the relative separation distance between two fragments or clusters and is supposed to assimilate the neck formation effects, and hence is referred to as the neck-length parameter.

2.2.4 Assault Frequency

The assault frequency can be calculated via different methods or sometimes taken as constant (nearly 10^{21}). In the present work, two type of assault frequencies i.e. classical assault frequency (ν_c) and Quantum assault frequency(ν_q) are used. In classical view, the assault frequency ν_c is calculated as

$$\nu_c = \frac{(2E_2/\mu)^{1/2}}{R_0}, \tag{2.26}$$

in the above equation, R_0 represents the radius of the nucleus, μ is the reduced mass, and E_2 denotes the kinetic energy of the cluster. The emitted cluster along with its complementary fragment is produced in the ground state decay mode. Hence, the Q-value (decay energy) of the outgoing decay channel represents the total kinetic energy (Q= E_1+E_2). This energy is shared between the decaying fragments in terms of E_1 (energy of the Daughter nucleus) and E_2 (energy of the emitted cluster). Energy E_2 can be calculated using relation

$$E_2 = \frac{A_1}{A}Q \tag{2.27}$$

and E_1 represent the recoil energy of complementary fragment (A_1). In quantum picture, the cluster is assumed to be vibrating in a harmonic oscillator potential near the surface of the parent nucleus [35]. The quantum assault frequency (ν_q) is given as

$$\nu_q = \frac{(G + \frac{3}{2})\hbar}{1.2\pi\mu R^2} \tag{2.28}$$

G denotes the global quantum number of a cluster state and is given using the Widermuth rule [36].

$$G = 2n + l = \sum_{i=1}^{4} g_i \tag{2.29}$$

The value of g_i is given as 4, for (N,Z) $\leq$ 82, 5 for 82 $<$ (N,Z) $\leq$126 and 6 for (N,Z) $>$ 126, where N, Z represent the neutron and proton numbers of the parent nucleus. for further details see ref. [35, 37, 38].

The binary decay analysis in the present work is made using the above mentioned preformed cluster model. As we discussed earlier, there is also probablity of ternary fission from a radioactive nucleus. For the three body decay analysis, some modifications are made in the PCM and the modified version is known as three cluster model (TCM). The explanation the TCM is given below.

2.3 Three cluster model (TCM)

The ternary decay analysis in the present work is made using the three cluster model (TCM) [3, 4]. This model is the extension of the PCM and based on the QMFT. In this model, the mass asymmetry flow (η-motion) takes place between the light and heavy fragment (A_1 and A_2), and the third fragment A_3 is kept fixed. The relative separation R between the decaying fragments depends on the geometrical arrangement of the three decaying fragments [4]. There are two probable geometrical arrangements [4] of the decaying fragments i.e. equatorial cluster tripartition (ECT) and collinear cluster tripartition (CCT) (will be discussed later in upcoming section). The ternary fission can be categorized into two kind of emission processes, on the basis of the size of the emitted fragments i.e. the light particle accompanied fission and the true ternary fission. In recent years, TCM successfully explored both the emission modes [39–41], and the obtained results are in good agreement with the experimental data. Additionally, the predictions are made in ref [39] for the true ternary fission in super heavy region using the postulates of the TCM. A flowchart representing the working of TCM is shown in figure.2.2. The model is work out in terms of the three body fragmentation potential, the penetration probability of the decay channel and the relative yield of the outgoing fragments. The explanation of these terms is given below:

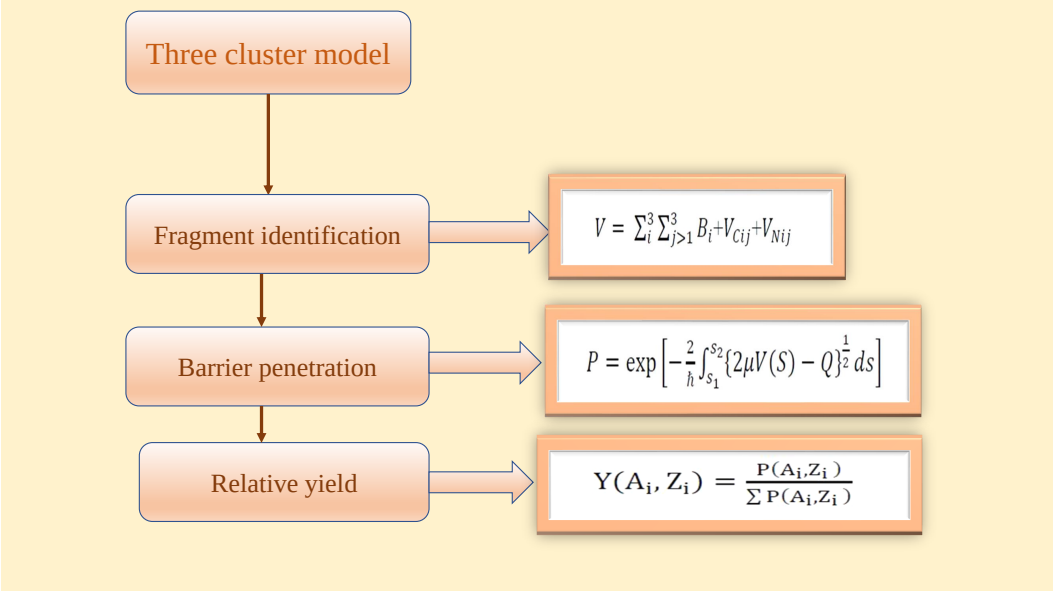

Figure 2.2: A flowchart represents different terms used in the three cluster model (TCM).

2.3.1 Geometrical arrangement

Numerous attempts [39–48] were made in last few decades to explore the ternary decay dynamics and concluded that the decay phenomenon depends on various factors such as the magicity, fissility parameter, deformations, orientations and the geometrical arrangement of the decaying fragments etc. The geometrical arrangement of the clusters plays crucial role in the ternary fission. Fragmentation structure drastically changes with respect to change in the geometrical arrangement of the decaying fragments. There are two probable arrangement of the decaying fragments i.e. equatorial cluster tripartition (ECT) and the collinear cluster tripartition (CCT). The pictorial representation of both the configurations is shown in fig.2.3. The configuration mode where the third fragment emission happens orthogonal to the fission axis is known as equatorial configuration arrangement or equatorial cluster tripartition (ECT). The pictorial representation of equatorial configuration is given in fig.2.3(a). In this case, the relative separation in between the fragments is taken as [49]

$$R_{12} = R_1 + R_2 + s_{12}, \tag{2.30}$$

$$R_{23} = R_2 + R_3 + s_{23}, \tag{2.31}$$

$$R_{31} = R_3 + R_1 + s_{31}. \tag{2.32}$$

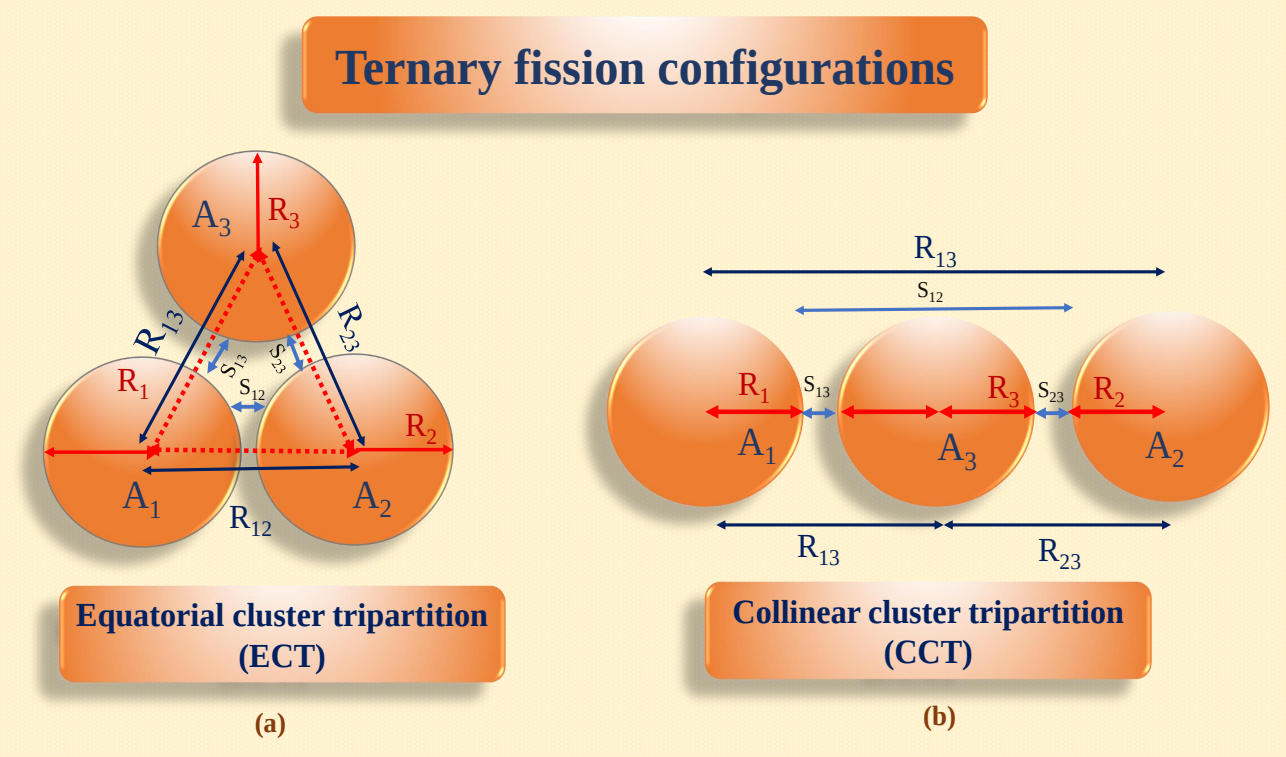

Figure 2.3: A pictorial representation of two probable geometrical configurations in ternary fision i.e. (a) equatorial cluster tripartition (ECT) and (b) collinear cluster tripartition (CCT) [49, 50].

Here R_1, R_2, R_3 represents the radius vector of three fragments, and the surface separation considered as $s_{12} = s_{23} = s_{31} = s$. On the other hand, the configuration mode where the third fragment emission happens along with the fission axis is known as collinear configuration arrangement or collinear cluster tripartitition (CCT), see Fig. 2.3(b). The relative distance in between the center of fragments is obtained using eqn.2.30-2.32 with an exception that, for collinear emission the surface separation $s_{12} = 2(R_3 + s)$ and $s_{23} = s_{31} = s$.

2.3.2 Three-body fragmentation potential

The identification of the decaying fragments in TCM is made using the fragmentation potential. The three body fragmentation potential is basically the sum of the binding energies of the outgoing fragments, repulsive Coulomb potential, attractive nuclear potential and

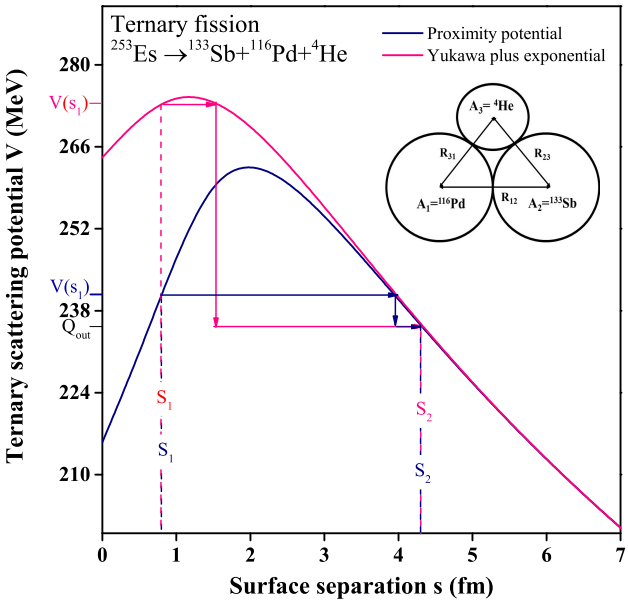

Figure 2.4: The ternary fission scattering potential V (MeV) as a function of surface separation (s) for ^{253}Es is plotted with the use of Yukawa plus exponential and proximity nuclear potentials.

collectively written as [4]

$$V_{tot} = \sum_{i=1}^{3}\sum_{j>1}^{3} B_i + V_{Cij} + V_{Pij}. \tag{2.33}$$

2.3.3 Penetration probability

In TCM, η motion is defined in terms of the fragmentation potential and the R-motion is studied using the penetration probability of the exit channel. The penetration probability is the probability for which three fragments cross the potential barrier, and is calculated using the WKB integral and given as

$$P = exp[-\frac{2}{\hbar}\int_{s_1}^{s_2}\{2\mu[V(R)-Q]\}^{1/2}ds]. \tag{2.34}$$

In the above expression, s_1 and s_2 are the first and second turning point satisfying the V(s_2)=Q condition (can be seen in (Fig. 2.4)). The Q-value for the decay of three fragments is obtained as $Q = M - \sum_{i=1}^{3} m_i$. It is important to mention that in case of collinear emission the available Q-value is assumed to be shared between first and the second frag-

ments (Q=E_1+E_2), assumed to be moving in opposite directions among the three decay products and the third fragment is considered at rest (E_3=0). In equation (2.34), μ is the reduced mass of three fragments [4] ,

$$\mu_{123} = \left(\frac{\mu_{12}A_3}{\mu_{12}+A_3}\right)m, \tag{2.35}$$

where $\mu_{12} = A_1A_2/(A_1+A_2)$ and m is the nucleon mass.

2.3.4 Relative yield

The relative yield for all the identified decay channels for the ternary fission process [29] is calculated as the ratio of a probable fragment combination over the sum of the penetration probabilities of all possible decay channel as

$$Y(A_i, Z_i) = \frac{P(A_i, Z_i)}{\Sigma P(A_i, Z_i)} \tag{2.36}$$

Here P(A_i,Z_i) is the three body penetration probability as given by Eq. (2.34).
The ground state binary and ternary decay analysis in the present work is done using PCM and TCM where the temprature effects remains silent (i.e. T=0 MeV). Although in some calculations, the temprature effects are also for the binary decay analysis. Such calculations are performed using the dynamical cluster decay model (DCM). The explanation of the DCM is given below.

2.4 Dynamical cluster decay model (DCM)

In the previous sections, the preformed cluster model (PCM) and three cluster model (TCM) are explained along the aasociated physical quantities. These models are used to study the ground state decay dynamics where the temprature effects remain silent. The temprature effects can be included in PCM and the modified version is known as the dynamical cluster decay model (DCM). The temprature (T) of the compound nuclei with excitation energy

E* is given using the relation [51]

$$E^* = \frac{A_{CN}}{a}T^2 - T. \tag{2.37}$$

The quantity $\left(\frac{A_{CN}}{a}\right)$ in above equation represents the level density, and 'a' varies from 9-11 depending upon mass of compound (A_{CN}). The excitation energy-dependent fragmentation potential, penetration probability, and preformation probability can be calculated using T dependence and a detailed description can be obtained in ref. [52–58]. The deformation parameter is also made temperature dependent [59, 60], by using the relation

$$\beta_{\lambda i}(T) = exp(-T/T_0)\beta_{\lambda i}(0), \tag{2.38}$$

where $\beta_{\lambda i}(0)$ is the static deformation and T_0 is the temperature of the nucleus at which the shell effects start to vanish (T_0=1.5 MeV) [61]. In DCM, the first turning point (R_a) is expressed as

$$\begin{aligned} R_a(T) &= R_1(\alpha_1, T) + R_2(\alpha_2, T) + \Delta R(T) \\ &= R_t(\alpha, T) + \Delta R(T), \end{aligned} \tag{2.39}$$

with radius vectors R_i $(i = 1, 2)$

$$R_i(\alpha_i, T) = R_{0i}(T)\left[1 + \sum_{\lambda}\beta_{\lambda i}Y_{\lambda}^{(0)}(\alpha_i)\right] \tag{2.40}$$

and T-dependent nuclear radii R_{0i} of the equivalent spherical nuclei [62],

$$R_{0i}(T) = [1.28A_i^{\frac{1}{3}} - 0.76 + 0.8A_i^{\frac{-1}{3}}](1 + 0.0007T^2)fm. \tag{2.41}$$

In addition to the above, the temprature effects can be incorporated into the fragmentation potential and the penetration path. The detailed description can be seen in ref. [63]

On the basis of above mentioned theoretical formalism, the binary and ternary decay analysis of the nuclei belongs to heavy mass region is carried out. The detailed analysis of theoretical investigation and the results obtained are discussed in the subsequent chapters.

Bibliography

[1] B. B. Singh, S. K. Patra and R. K. Gupta, Phys. Rev. C **82** 014607 (2010).

[2] S. K. Arun *et al.*, Phys. Rev. C **79** 064616 (2009).

[3] K. R. Vijayraghvan *et al.*, Phys. Rev. C **91** 044616 (2015).

[4] K. Manimaran and M. Balasubramaniam, Phys. Rev. C **83** 034609 (2011).

[5] J. Maruhn and W. Greiner, Phys. Rev. Lett. **32**, 548 (1974).

[6] R. K. Gupta, W. Scheid, and W. Greiner, Phys. Rev. Lett. **35**, 353 (1975).

[7] R. K. Gupta, A. Sandulescu, and W. Greiner, Phys. Lett. B **67**, 257 (1977)

[8] D. R. Saroha and R. K. Gupta, J. Phys. G: Nucl. Phys. **12**, 1265 (1986)

[9] A. Kaur and M. K. Sharma, Eur. Phys. J. A **55**, 89 (2019).

[10] R. K. Gupta *et al.*, Phys. Rev. C **56**, 6 (1997).

[11] B. B. Singh *et al.*, Phys. Rev. C **77**, 054613 (2008).

[12] M. Bansal *et al.*, Phys. Rev. C **86**,034604 (2012).

[13] G. Sawhney *et al.*, Phys. Rev. C **83**,064610 (2011).

[14] S. K. Arun *et al.*, Phys. Rev. C **79**,064616 (2009).

[15] R. Kumar and M. K. Sharma, Phys. Rev. C **85**,054612 (2012).

[16] M. Balasubramaniam and R. K. Gupta,Phys. Rev. C **60**,064316 (1999).

[17] N. K. Virk *et al.*, Eur. Phys. J. A **56**, 35 (2020).

[18] K. Sharma, *et al.*, Nucl. Phys. A **972**, 1 (2018).

[19] K. Sharma, G. Sawhney, and M. K. Sharma, Phys. Rev. C **96**, 054307 (2017).

[20] G. Audi, A. H. Wapstra, and C. Thibault, Nucl. Phys. A **729**, 337 (2003).

[21] P. M¨oller, J. R. Nix, W. D. Myers, and W. J. Swiatecki, At. Data Nucl. Data Tables **59**, 185 (1995).

[22] M. Wang, A. Wapstra,*et al.*, Chin. Phys. C **59**, 1603 (2012).

[23] K. Alder and A. Winther, Nucl. Phys. A **132**, 14 (1969).

[24] B. V. Carlson, L. C. Chamon and L. R. Gasques, Phys. Rev. C **70**, 057602 (2004).

[25] N. Takigawa, T. Rumin, and N. Ihara, Phys. Rev. C **60**, 044607 (2000).

[26] R. K. Gupta, M. Balasubramaniam, R. Kumar, N. Singh, M. Manhas and W. Greiner, J. Phys. G: Nucl. Part. Phys. C **31**, 631 (2005).

[27] G. Shanmugam and B. Kamalharan, Phys. Rev. C **38**, 1377 (1988).

[28] J. Blocki, J. Randrup, W. J. Swiatecki, and C. F. Tsang, Ann. Phys. (N.Y.)**105**, 427 (1977).

[29] W. D. Myers and W. J. Swiatecki, Phys. Rev. C **62**, 044610 (2000).

[30] I. Dutt and R. K. Puri, Phys. Rev. C **81**, 064609 (2010).

[31] H. Kroger and W. Scheid, J. Phys. G **6**, L85 (1980).

[32] J. Maruhn and W. Greiner, Phys. Rev. L **32**, 10 (1974).

[33] R. K. Gupta, W. Scheid and W. Greiner, Phys. Rev. L **35**, 6 (1975).

[34] M. Greiner and W. Scheid, J. Phys. G 12, L229 (1986).

[35] H. F. Zhang, G. Royer, and J. Q. Li, Phys. Rev. C **84**, 027303 (2011).

[36] K. Wildermuth and Y. C. Tang, A Unified Theory of the Nucleus (Academic, New York, 1977).

[37] P. Mohr, Phys. Rev. C **61**, 045802 (2000).

[38] B. Buck, A. C.Merchant, and S.M. Perez, Phys. Rev. C **51**, 559 (1995).

[39] M. Balasubramanian *et al.*, Phys. Rev. C **93**, 014601 (2016).

[40] K. Vijayraghvan *et al.*, Phys. Rev. C **90**, 024601 (2014).

[41] M. Balasubramanian *et al.*, Pramana **85**, 423 (2015).

[42] N. Sharma *et al.*, Phys. Rev. C **102**, 064603 (2020).

[43] N. Sharma *et al.*, Phys. Rev. C **105**, 044602 (2022).

[44] S. W. Cosper, J. Cerny, and R. C. Gatti, Phys. Rev. **154**, 1193 (1967).

[45] G. M. Raisbeck and T. D. Thomas, Phys. Rev. **172**, 1272 (1968)

[46] S. L. Whetstone and T. D. Thomas, Phys. Rev. Lett. **15**, 298 (1965); Phys. Rev. **154**, 1174 (1967).

[47] D. N. Poenaru *et al.*, Rom. Rep. Phys. **55**, 781 (2003).

[48] K. R. Vijayaraghavan, M. Balasubramaniam, and W. Von Oertzen, Phys. Rev. C **91**, 044616 (2015).

[49] K. Manimaran and M. Balasubramaniam, Phys. Rev. C **83**, 034609 (2011).

[50] S. Thakur *et al.*, Int. J. Mod. Phys. E **22**, 1350014 (2013)

[51] K. J. Lecouteur and D. W. Lang, Nucl. Phys. **13**, 32 (1959).

[52] A. Kaur and M. K. Sharma, Phys. Rev. C **99**, 044611 (2019)

[53] A. Kaur and M. K. Sharma, Eur. Phys. J. A **55**, 89 (2019).

[54] G. Kaur, K. Sandhu, A. Kaur, and M. K. Sharma, Phys. Rev. C **97**, 054602 (2018)

[55] A. Kaur, G. Kaur, S. K. Patra, and M. K. Sharma, Nucl. Phys. A **990**, 94 (2019).

[56] B. B. Singh, M. K. Sharma, and R. K. Gupta, Phys. Rev. C **77**, 054613 (2008).

[57] S. Chopra, N. Goel, M. K. Sharma, P. O. Hess, Phys. Rev. C **106**, L031601 (2022).

[58] Raj K. Gupta, M. Balasubramaniam, Rajesh Kumar, Dalip Singh, C. Beck, and Walter Greiner, Phys. Rev. C **71**, 014601 (2005).

[59] M. Muenchow and W. Scheid, Phys. Lett. B **162**, 265 (1985); Nucl. Phys. A **468**, 59 (1987).

[60] M. Rashdan, A. Faessler, and W. Waida, J. Phys. G: Nucl. Part. Phys. **17**, 1401 (1991).

[61] A. S. Jensen, J. Damgaard, Nucl. Phys. A **203**, 578 (1973).

[62] G. Royer and J. Mignen, J. Phys. G: Nucl. Part. Phys. **18**, 1781 (1992).

[63] C. Karthikraj *et al.*, Phys. Rev. C **86**,014613(2012).

Chapter 3

Alpha decay analysis using different impinging frequency

In the previous chapter, details of the theoretical formalism (PCM and TCM) employed in the present work is explained. The binary decay modes are explored with the help of PCM and the ternary decay mechanism is studied using TCM. As expected, it is evident that the binary decay mode has higher occurrence probability as compared to the ternary decay mechanism. In the binary decay modes, α-decay is the most common observed mode and plays a crucial role in the stability analysis of the radioactive nuclei. In the present chapter, an analysis of the α-decay is made using classical and quantum mechanical discriptions of the assault frequencies. The isotopic analysis of the polonium (Po) isotopes is made using the fragmentation potential, preformation probability (P_0), and penetration probability (P). The role of the shell closure effects in the α-decay mechanism is explored. The detailed analysis of the α-decay mode is given below.

3.1 Introduction

Generally, it is considered that a radioactive nucleus may try to reach a stable configuration via emergence of alpha (α), beta (β) and gamma (γ) decay modes respectively. There are also other radioactive decay modes such as the cluster radioactivity (CR) [1,2], heavy particle radioactivity (HPR) and the spontaneous fission (SF) [3], etc. In the above mentioned decay modes, α decay is most common observed mode which have higher decay probability among other competing modes (CR, HPR , SF etc.). Further, α decay also works as an decisive factor for the stability analysis of nuclei belonging to heavy and super-heavy mass regions [4–13]. Few experimental attempts [14] explore the continuous emission of α particle nearby Z=50. The alpha decay chains are also observed in case of super heavy mass region, where successive alpha emission happens and the process terminates with spontaneous fission. Hence, the alpha decay plays an important role to explore the decay dynamics and the associated stability aspects.

Numerous experimental and theoretical attempts [15–28] were performed to understand the radioactive emergence of the α particle. Several nuclear models such as Generalized liquid drop model (GLDM) [29, 30], Cluster formation model(CFM) [31], Double folding potential model [32], Unified fission model (UFM) [33], Analytical super asymmetric fission model (ASAFM) [34] and Preformed cluster model (PCM) [35, 36] were introduced to understand the cluster-core interplay within the radioactive parent nuclei. The above mentioned models are based on some assumptions and work out in terms of certain coordinates to study different decay properties associated with unstable nuclei. In generalized liquid drop model (GLDM), the macroscopic liquid drop energies plays key role to give different decay channel properties. On the other hand, unified fission model (UFM) is introduced, where the preformation or spectroscopic factors are taken to be unity and the decay half-lives are calculated using the barrier characteristics. Similarly, the preformed cluster model (PCM) [37], successfully explored different ground state decay mechanisms such as alpha decay, CR, HPR and SF [38, 39] etc. In this model, cluster is supposed to be in a preborn state within the parent nucleus and the cluster core interplay is explored using the mass asymmetry coordinates and the relative separation distances. These coordinates are further employed collectively and give the preformation probability of the decaying fragments which will further serve as a prime tool for the evaluation of the decay life-time and the decay constant. The stability analysis of a radioactive nucleus depends on the decay constant which is a product of preformation probability (P_0), Penetration probability and the barrier assault frequency. The term "impinging frequency" or the "assault frequency" is the frequency of the α particle near the surface of the parent nucleus. The preformation probability of the probable decay channel is calculated with the help of stationary Schrödinger equation and the penetration probability is calculated via WKB approximation method. In the present work the role of assault frequency (ν_0) is calculated using classical and quantum mechanical views. In classical view, the assault frequency is calculated using the decay energy or the total kinetic energy, which is shared among the decay fragments [40]. In quantum mechanical view, the cluster is supposed to vibrate near the surface of the parent nucleus under the influence of a harmonic oscillator potential [41]. Furthermore, some attempts were made [42, 43] where the modified assault frequency parameters were introduced. It is assumed that the spectroscopic factors are included in such calculations. In the present chapter, an attempt is made to explore the role of effective assault frequency parameters

using the Q value of the decay channel.

As discussed earlier, the α particle emission is one of the major common emission mode in a radioactive nucleus, which may attain a stable configuration under the influence of proton or neutron shell closure effects. It will be of interest to study such effects for chosen set of nuclear isotopes. In this chapter, α decay analysis of $^{188-218}$Po isotopes is performed which after α decay give the lead (Pb) isotopes as daughter fragment. The α particle emission is studied using PCM and the behaviour of the preformation probability, penetration probability and assault frequency is explored with respect to increment in the neutron number of the parent or daughter nucleus. A comparative analysis of α decay half-lives is made using different choices of assault frequency. The overview of this chapter is as follows. In Section.3.2 of the chapter, alpha decay analysis of Po isotopes is carried out using different assault frequencies. The effective frequency parameter is given and further this parameter is used to calculated the decay half-lives of Rn isotopes. Finally, a summary of the observations and conclusions drawn is outlined in Section.3.3. The work presented in this chapter is published in the ref [44]

3.2 Calculations and the results

The present section represents theoretical investigation of alpha emission from $^{188-218}$Po isotopes using preformed cluster model. The calculations are done using quadrupole deformation (β_2) with cold-elongated configuration. First, in Section.3.2.1, the fragmentation analysis of Po isotopes is carried out using the fragmentation potential. The importance of neutron shell closure effects is explored using the preformation probability and the penetration probability. The decay half-lives of the polonium isotopes is calculated using two choices of assault frequencies (ν_c and ν_q). In Section.3.2.2 , the effective assault frequency of the polonium isotopes is calculated and an effort is made to estimate $T_{1/2}$ using a Q-value dependent assault frequency parameter. Further, in Section.3.2.3, the alpha decay half-lives of Rn isotopes are calculated using the effective assault-frequency parameter ν_e given in Section.3.2.2.

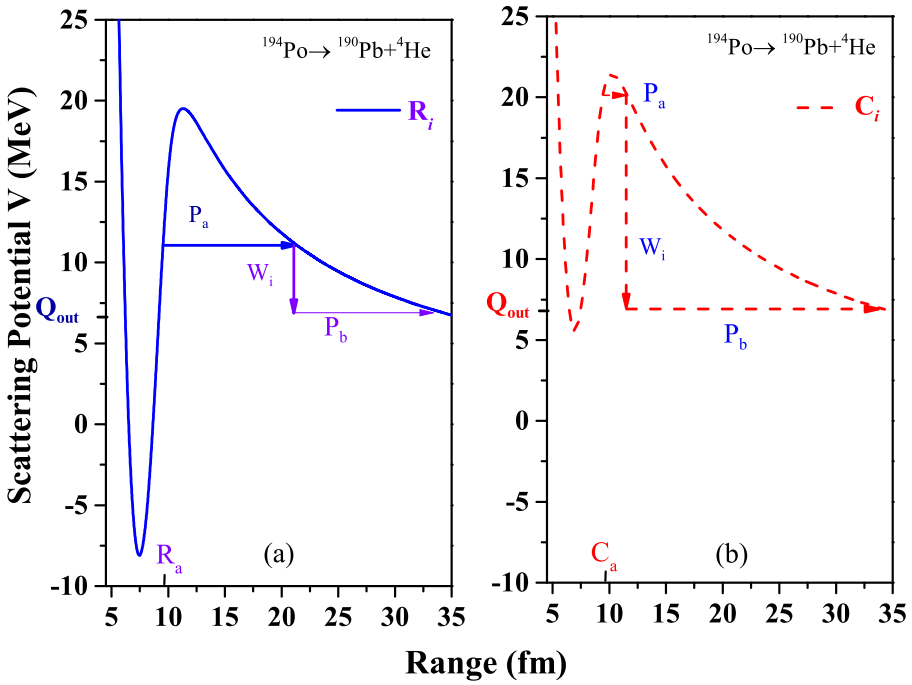

Figure 3.1: The scattering potential V(R) of the α emission mode using effective sharp (a) radius R_i (without surface diffuseness) and (b) süsumann central radii C_i (with surface diffuseness).

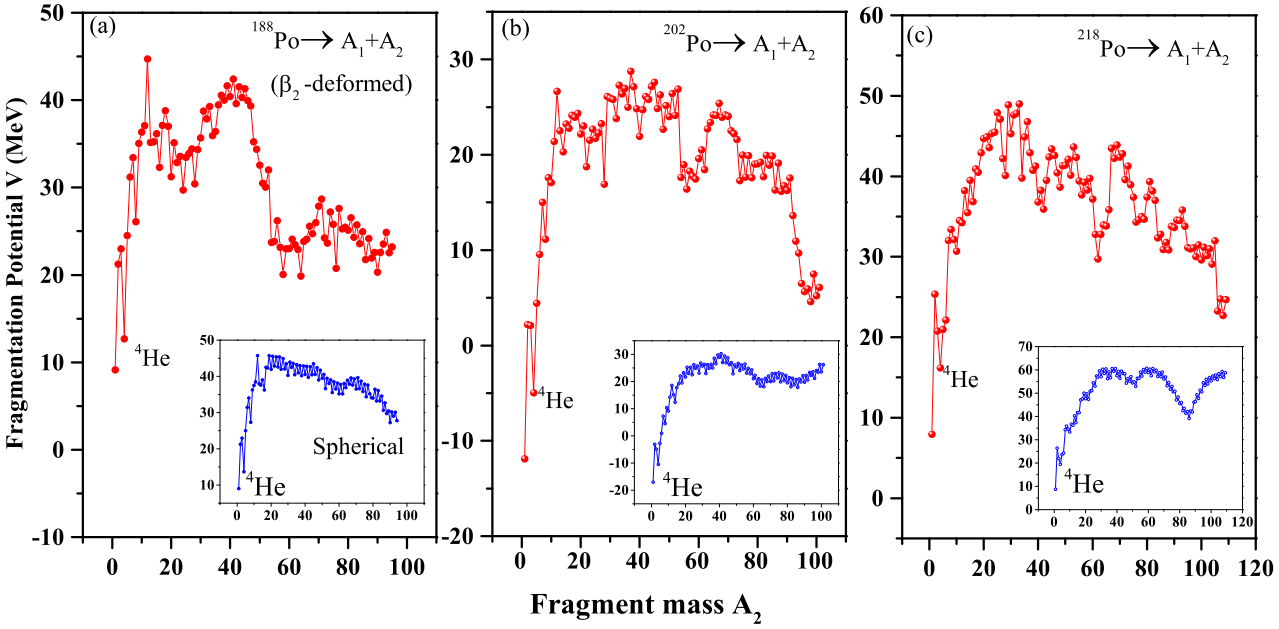

Figure 3.2: The fragmentation potential V with respect to increase in the fragment mass A_2 for the (a) ^{188}Po, (b) ^{202}Po and (c)^{218}Po isotopes using deformed and spherical choice (within small box) of the decaying fragments.

3.2.1 Alpha decay analysis of $^{188-218}$Po isotopes using different assault frequency

In this section, isotopic analysis of Po nuclei is carried out using the preformation probability (P_0) , penetration probability (P) and the assault frequency (ν). The explored data of P_0, P and ν is used to estimate the half-lives of the Po isotopes. The decay half-lives are also affected by the surface diffuseness of the decaying fragments. It is suggested by different authors [46,47] that the surface diffuseness along with the deformation effects play important role on the decay mechanism. Similarly, in [48] it is concluded that nuclear surface diffuseness is an important property that must be added along with the deformation effects for lighter cluster ($A_2 < 20$). As we are interested in alpha particle emission, hence as a first step a comparison of barrier characteristics without surface diffuseness (R_i) and with surface diffuseness (C_i) is made and shown in figure.3.1. Here, we are interested to study the Inter-fragment radii with inclusion of surface diffuseness (C_i) or without surface diffuseness(R_i). The difference in the barrier characteristics is due to the change in the proximity potential and the Coulomb potential. The barrier position and the barrier height is different for both cases. Hence, the penetration probability for both of the cases get modified accordingly. We have performed calculations using both radii and C_i gives better agreement with the experimental data (will be discuss in further in figure.3.6). After the analysis of surface diffusion, the fragmentation potential $V_R(\eta)$ is calculated which will further help to suggest the most probable decaying fragments of the exit channel. The fragmentation potential for ^{188}Po,^{202}Po and ^{218}Po isotopes as a function of the fragment mass A_2 is shown in figure.3.2 (a-c). The fragmentation structure for spherical choice of the decaying fragments is shown within inset. The minima in the fragmentation potential represents the most probable decay fragment along with its complementary fragment for both spherical and deformed choices. One can observe from the figure that A_2=^{4}He is located at minima for all three isotopes and may be treated as one of the most probable fragment along with its complementary daughter. It may be concluded that independent of deformation effects, the alpha decay is the most prominent decay choice among its competing decay channels for the chosen isotopes of polonium nucleus. Furthermore, one can observe that the fission region changes from the symmetric fission mode to the asymmetric fission mode when one proceeds from ^{188}Po to the ^{218}Po isotope for the spherical choice of fragmentation. For the deformed choice, fission

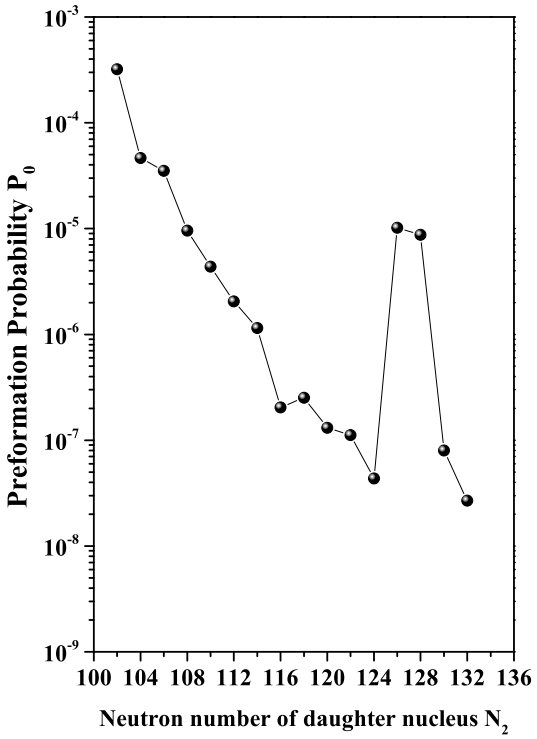

Figure 3.3: The preformation probability P_0 as a function of neutron number N_2 for $^{188-218}$Po isotopes

region changes from asymmetric to nearly symmetric mode. It is relevant to note that alpha decay is observed experimentally for this nucleus, other decay modes such as CR or SF are not yet observed. Hence, in the present work we are interested to study the alpha particle emission only.

The preformation probability P_0 is estimated using the stationary Schrodinger equation in terms of η (the mass asymmetry coordinate). In figure.3.3, preformation probability is plotted with respect to neutron number N_2 of the daughter nucleus. It is observed that P_0 decreases with increase in the neutron number up to N_2=124 (for parent nucleus N =126) and increases abruptly with addition of two more neutrons in the parent nucleus. Such kind of behaviour of P_0 is due to influence of neutron shell effects (N=126) and it may be concluded that the alpha cluster preformation yield decreases as the nucleus approach the shell closure. The P_0 value is found maximum at N_2=126 (with N=128) because the preformation probability is higher for the case where the alpha particle is accompanied with a stable nucleus complementary fragment. Hence, preformation factors strongly depends on the shell effects effects of the parent nucleus as well as that of the decaying fragments.

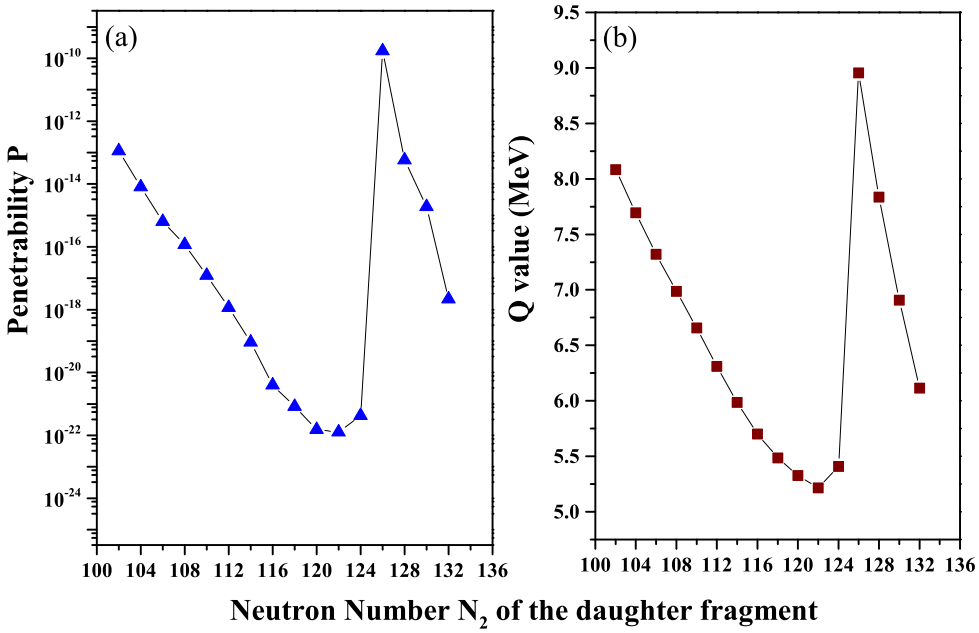

Figure 3.4: The PCM calculated (a) penetration probability P and (b) the Q value of the α decay channel as a function of neutron number of the daughter fragment N_2.

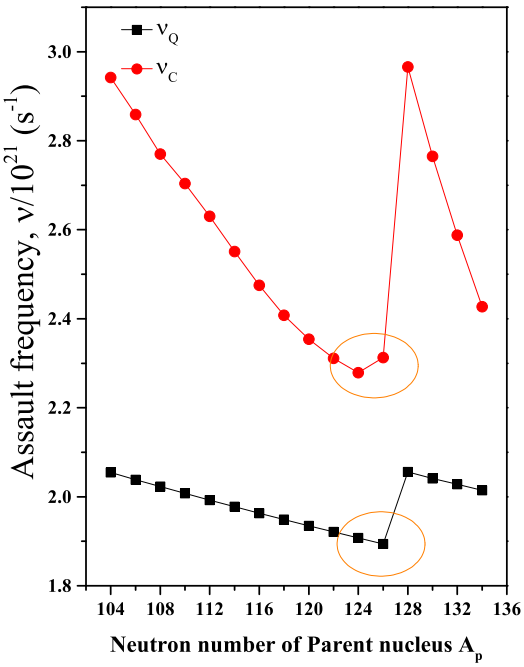

Figure 3.5: Calculated (a) Quantum assault frequency (ν_q) and (b) Classical assault frequency (ν_c) with respect to increase in the neutron number of the parent nucleus.

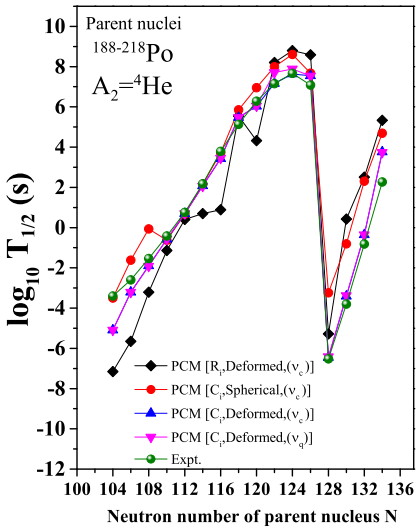

Figure 3.6: PCM calculated decay half-lives using Quantum assault frequency ν_q and classical assault frequency ν_c with respect to increase in the neutron number of the parent nucleus for spherical and the deformed choice of the decaying fragments. The calculated decay half-lives are compared with the experimental data [51].

After the analysis of P_0, the penetration probability P is calculated using WKB approximation. figure.3.4.(a) represents the penetration probability with respect to neutron number of the daughter nucleus N_2. The penetration probability P decreases with respect to increase in neutron number and shows similar behaviour as we observed in case of P_0. It may be noted that the penetration probability P depends on the Q value of the decay channel [38]. We have plotted the Q value of the decay channel as a function of neutron number of the daughter nucleus N_2 in figure.3.4.(b). The trend of of barrier penetrability P is similar to that of the Q value, both decrease till N = 126 and get maximum value for the case of N_2=126. Hence, the penetrability and Q-value are also influenced by the shell effects. Further, the classical assault frequency ν_c and quantum assault frequency ν_q is also calculated and plotted with respect to the neutron number N of parent nucleus in figure.3.5. One can note that the assault frequencies (ν_c and ν_q) starts diminishing as one approach towards the N=126. Such kind of variation in ν_c is basically due to the influence of the decay energy (Q value) which is shared among the decaying fragments. Further, the global quantum number [41] plays important role in case of ν_q, due to which the assault frequency starts decreasing till N = 126. It is concluded that the assault frequency is also influenced by the shell effects of the parent nucleus.

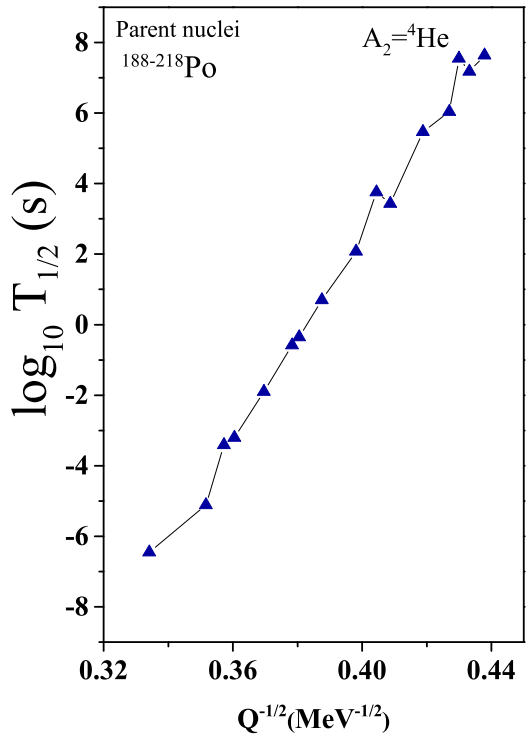

Figure 3.7: The calculated Log $T_1/2$ as a function of $Q^{-1/2}$ for the verification of G-N law.

Hence, the P_0,P and ν play key role in the alpha decay process and many other theoretical approaches such as SAM and GLDM [49,50], also explore the importance of these factors for polonium isotopes. The PCM calculated P_0,P and ν is compared with these factors in table 3.1. It may be noted that the PCM calculated assault frequency ν and log P_0P value compare nicely with the literature and few order difference is seen for the calculated P_0 and P values. PCM is based on the collective clusterization approach, which handle all the probable decay processes (such as light particle, alpha particle, cluster, intermediate/heavy mass fragment and fission decay) on parallel footing. Since the PCM deals with collective clusterization approach, the relative preformation probabilities of all minimized binary fragments are calculated by solving Schrödinger equation in mass asymmetry coordinate η. The penetration probability is calculated as three step process following the excitation model of Greiner *et al.* [60]. However, In GLDM and SAM, the penetration probability P is calculated as a single step process and the P_0 values are given using the experimental half-lives and the empirical relation.

After studying the behaviour of P_0,P and ν, the alpha decay half lives are calculated

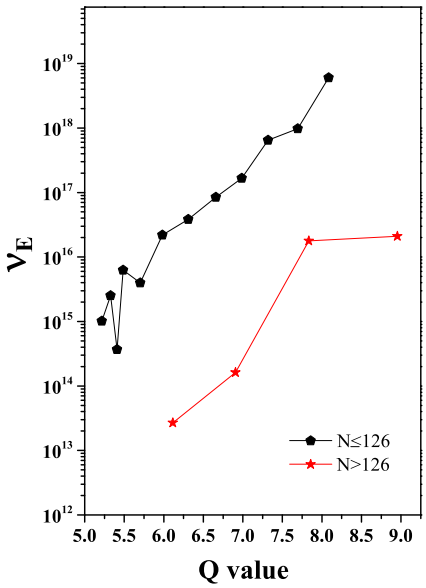

Figure 3.8: The calculated effective assault frequency as a function of Q value for N $\leq$ 126 and N $>$ 126.

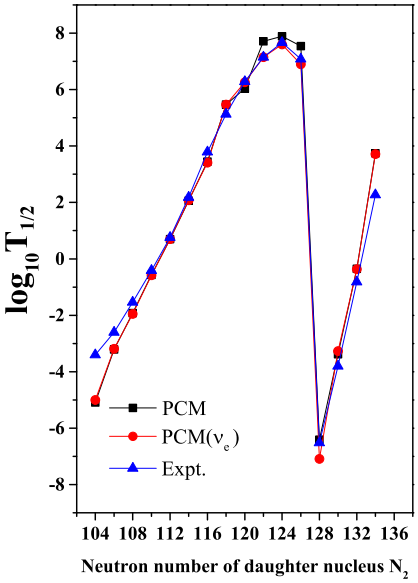

Figure 3.9: The calculated Decay half-lives of Po isotopes using effective assault frequency parameter (ν_e) and its comparison with previous calculation (PCM(ν_q) and the experimental data [51].

Table 3.1: PCM calculated preformation probability (P_0), penetrability (P) and the assault frequency (ν_c) for the α decay of $^{188-218}$Po isotopes and a comparison of these values is made with theoretical models SAM and GLDM [49, 50] calculated values

Parent	PCM				SAM [49]				GLDM [50]			
nucleus	logP_0	log P	logP_0P	$\nu/10^{21}(s^{-1})$	logP_0	log P	logP_0P	$\nu/10^{21}(s^{-1})$	logP_0	logP	logP_0P	$\nu/10^{21}(s^{-1})$
^{188}Po	-3.531	-12.950	-16.482	2.942					-1.832	-16.089	-17.922	1.452
^{190}Po	-4.319	-14.091	-18.410	2.859	-1.348	-17.17	-18.518	1.41	-1.477	-17.228	-18.706	1.411
^{192}Po	-4.496	-15.197	-19.694	2.771	-1.336	-18.34	-19.676	1.37	-1.350	-18.407	-19.758	1.371
^{194}Po	-5.080	-15.925	-21.006	2.704	-1.325	-19.47	-20.795	1.33	-1.387	-19.488	-20.875	1.335
^{196}Po	-5.370	-16.913	-22.284	2.630	-1.312	-20.69	-22.002	1.30	-1.341	-20.690	-22.032	1.299
^{198}Po	-5.710	-17.936	-23.646	2.551	-1.299	-22.09	-23.389	1.26	-1.357	-22.081	-23.439	1.259
^{200}Po	-5.953	-19.033	-24.987	2.475	-1.286	-23.52	-24.806	1.22	-1.522	-23.513	-25.036	1.222
^{202}Po	-6.689	-20.394	-27.084	2.408	-1.274	-24.84	-26.114	1.19	-1.600	-24.764	-26.364	1.188
^{204}Po	-6.490	-21.077	-27.567	2.354	-1.265	-25.89	-27.155	1.16	-1.642	-25.861	-27.503	1.161
^{206}Po	-6.882	-21.819	-28.701	2.311	-1.257	-26.73	-27.987	1.14	-1.718	-26.647	-28.366	1.141
^{208}Po	-7.273	-21.893	-29.166	2.279					-1.939	-27.242	-29.181	1.126
^{210}Po	-7.712	-21.365	-29.078	2.313	-1.257	-26.24	-27.497	1.14	-2.187	-26.118	-28.305	1.142
^{212}Po	-4.712	-9.762	-14.475	2.966	-1.365	-13.41	-14.775	1.46	-1.467	-13.337	-14.804	1.466
^{214}Po	-4.952	-13.232	-18.184	2.765	-1.334	-16.42	-17.754	1.36	-1.058	-16.365	-17.424	1.366
^{216}Po	-6.501	-14.719	-21.220	2.588	-1.306	-19.47	-20.773	1.28	-1.010	-19.435	-20.445	1.278
^{218}Po	-7.571	-17.661	-25.232	2.427	-1.278	-22.65	-23.928	1.20	-0.961	-22.546	-23.507	1.199

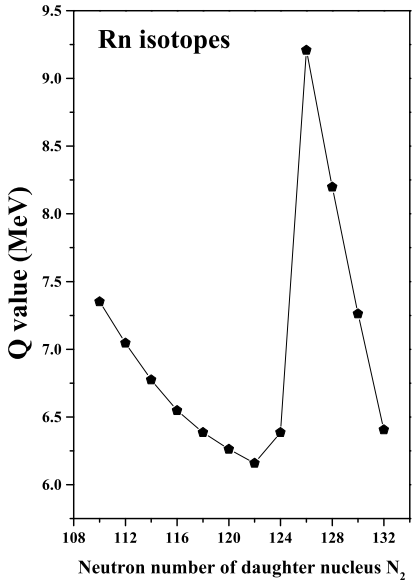

Figure 3.10: The calculated Q value for Rn isotopes as a function of neutron number of the parent nucleus.

using both choices of assault frequencies ν_c and ν_q and results are reported in Table 3.2. A comparison of the evaluated results is made with the experimental data [51] and other theoretical models such as CPPM, ADF, UDL, SLH, SLB and SemFIS etc [52–59]. It may be observed from the table that the calculated decay half-lives find nice agreement with the available experimental and the theoretical data. PCM calculations seem independent of the assault frequencies, except for lightest and heaviest isotopes of Po chosen for the analysis.

The calculated half-lives are plotted with respect to the neutron number of parent nucleus (N) in figure.3.6 for ν_c and ν_q using spherical and deformed choice of the decaying fragments and comparison is made with the experimental data. It can be observed that the decay half lives increase with respect to the increment in the neutron number N of the parent nucleus and its magnitude is maximum at N=126. The obtained representation is in accordance and agreement with the results obtained for the P_0,P and ν. The deformed choice of the decaying fragments gives better results as compared with the spherical choice. Additionally, the half-lives calculated using C_i gives better results as compared with R_i. It may be concluded from the above analysis that the decay half lives and other factors (P_0,P and ν) strongly depends on the shell closure, Q value of the decay channel along with the associated deformation effects. The Q value dependency on the decay half-lives can be visualized using Geigger-

Table 3.2: PCM calculated half-life times $\log T_{1/2}$ for the α decay of $^{188-218}$Po isotopes using different assault frequencies ν_c, ν_q and a comparison of decay half-lives is made with the experimental data [51] and different theoretical formulas (CPPM, ADF, UDL, SLH, SLB, SemFIS) [52–59] calculated values. The optimized value of neck length parameter ΔR is also shown in the table.

Parent	PCM (ν_c)		PCM (ν_q)		Expt.	CPPM	ADF	UDL	SLH	SLB	SemFIS
nucleus	ΔR (fm)	$\log T_{1/2}$	ΔR(fm)	$\log T_{1/2}$							
^{188}Po	1.92	-5.11	1.92	-5.09	-3.40	-3.50	-3.64	-4.42	-4.04	-3.43	-3.88
^{190}Po	1.91	-3.20	1.90	-3.21	-2.62	-2.38	-2.57	-3.22	-2.88	-2.23	-2.78
^{192}Po	1.93	-1.90	1.92	-1.90	-1.47	-1.21	-1.46	-1.98	-1.65	-0.98	-1.64
^{194}Po	1.61	-0.58	1.61	-0.57	-0.41	-0.08	-0.41	-0.80	-0.47	0.20	-0.53
^{196}Po	1.51	0.70	1.51	0.70	0.76	1.13	0.72	0.46	0.78	1.46	0.64
^{198}Po	1.36	2.14	1.36	2.08	2.26	2.53	2.02	1.90	2.21	2.90	2.00
^{200}Po	1.25	3.43	1.26	3.41	3.79	3.98	3.35	3.38	3.67	4.37	3.40
^{202}Po	1.35	5.47	1.32	5.47	5.15	5.32	4.57	4.74	5.02	5.73	4.69
^{204}Po	1.19	6.03	1.21	6.04	6.28	6.43	5.58	5.86	6.13	6.84	5.75
^{206}Po	1.20	7.17	1.30	7.71	7.15	7.28	6.33	6.70	6.99	7.70	6.55
^{208}Po	1.00	7.64	1.10	7.89	7.96	7.89	6.88	7.32	7.62	8.33	7.14
^{210}Po	1.20	7.55	1.20	7.54	7.08	6.75	5.81	6.18	6.56	7.26	6.04
^{212}Po	1.00	-6.45	1.00	-6.41	-6.52	-6.26	-6.62	-7.31	-6.42	-5.82	-6.57
^{214}Po	0.50	-3.41	0.50	-3.38	-3.80	-3.28	-3.68	-4.10	-3.28	-2.67	-3.65
^{216}Po	0.70	-0.35	0.70	-0.34	-0.82	-0.21	-0.72	-0.87	-0.13	0.49	-0.65
^{218}Po	0.90	3.76	0.90	3.74	2.28	3.03	2.31	2.45	3.10	3.76	2.47

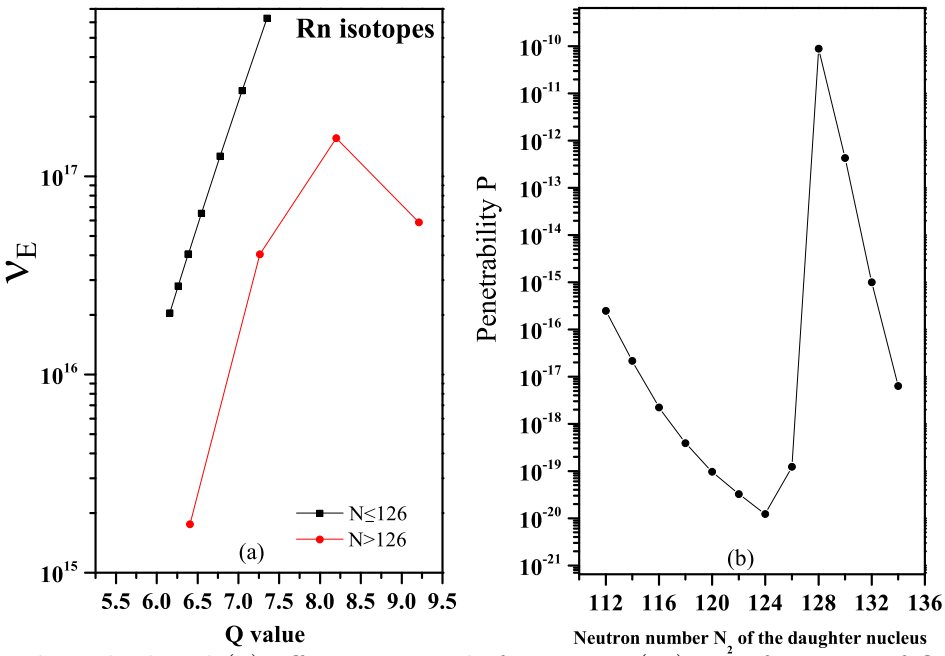

Figure 3.11: The calculated (a) effective assault frequency (ν_e) as a function of Q value and (b) barrier penetrability P as a function of neutron number of the daughter nucleus N_2.

Nuttal plot, where linear variation is observed among the decay half-lives and $Q^{-1/2}$. After the analysis of decay half-lives, verification of Geigger-Nuttal (G-N) plot is donein view of log $T_{1/2}$ vs. $Q^{-1/2}$ in figure.3.7. It is observed that log $T_{1/2}$ varies almost linearly with increase in the value of $Q^{-1/2}$ (with slope 141.437 and intercept -54.04). Hence, the calculated $T_{1/2}$ are in agreement with the G-N plot, which means that the decay half-lives are strongly influenced by the Q-value of the exit channel.

3.2.2 Study of the effective assault frequency of polonium isotopes

In the previous section, behaviour of penetration probability P, preformation probability P_0 and the assault frequency ν is studied with respect to the neutron number of the daughter fragment (N_2) or the parent nucleus (N). It was concluded that all of the three parameters play crucial role for the stability analysis of the radioactive nucleus. The stability further depends on the shell effects and the Q-value of the decay channel. In refs. [42, 43] different preformation parameter or assault frequency parameter are introduced which depend on the Q-value, Isospin and the charge number of the daughter nucleus accompanied with the

Table 3.3: PCM calculated half-life times $T_{1/2}$ for the α decay of $^{198-220}$Rn isotopes using effective assault frequencies ν_e a comparison is made with the avialable experimental results [51]. The value of the neck-length ΔR and Q value is also shown in the table.

Parent nucleus	Q Value (MeV)	PCM (ν_E)		Expt.
		ΔR (fm)	log$T_{1/2}$	log$T_{1/2}$
^{198}Rn	7.351	1.92	-2.35	-1.19
^{200}Rn	7.045	1.85	0.07	0.04
^{202}Rn	6.775	1.92	0.391	1.04
^{204}Rn	6.547	1.90	1.437	2.00
^{206}Rn	6.385	1.92	2.89	2.74
^{208}Rn	6.262	1.93	2.90	3.38
^{210}Rn	6.159	1.92	3.44	3.95
^{212}Rn	6.386	1.90	2.15	3.16
^{214}Rn	9.209	1.35	-6.87	-6.57
^{216}Rn	8.198	1.30	-4.98	-4.35
^{218}Rn	7.262	1.35	-1.76	-1.46
^{220}Rn	6.405	1.00	1.79	1.75

α particle. Additionally, some parameters are given which contain both assault frequency and preformation factor. Such type of parameter is known as modified assault frequency or effective assault frequency (ν_e). Following this work, the product of the quantum mechanical assault frequency (ν_q) and the calculated preformation probability is framed with respect to the Q-value for N $\leq$ 126 and N $>$ 126 and shown in figure 3.8. It can be observed from the figure that the effective assault frequency increases with increase in the Q-value. Using this plot a second order polynomial is obtained for the assault frequency parameter as a function of Q value as given below.

$$Log\nu_e = AQ^2 + BQ + C \tag{3.1}$$

where A = -0.06315, B = 2.10074 and C = 5.76766 for N $\leq$ 126 and A = -0.53702, B = 8.9285 and C = -19.91152 for N $>$ 126. The validity of these parameters is analysed by calculating the decay half-lives of the Polonium isotopes using eqn.3.1. The ν_e calculated decay half-lives are compared with the calculations performed in Section.3.2.1 and the experimental results, and indicated in figure.3.9. Here in this plot, PCM (ν_q) denotes the calculations which are performed in Section.3.2.1 and PCM (ν_e) is the calculations which is performed

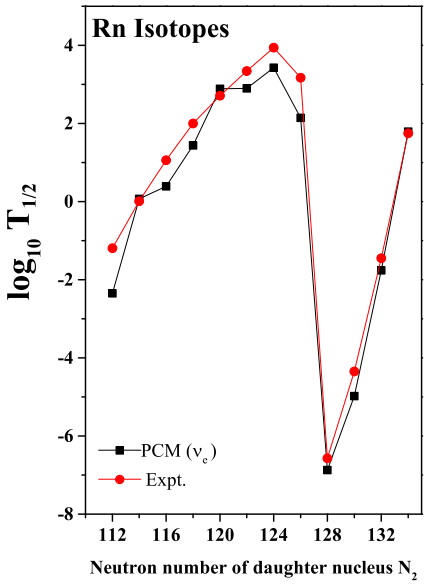

Figure 3.12: The calculated decay half lives using the effective assault frequency (ν_e) and barrier penetrability, and its comparison with the available experimental data

using the frequency parameter (Eqn. 3.1). It can be observed from the figure that PCM (ν_e) calculated decay half lives are in good agreement with the PCM (ν_q) and the experimental data. Hence one may use Eqn.3.1 to calculate the half-lives, where the Q-value lies in range 5 - 10 MeV.

3.2.3 Verification of effective assault frequency parameter

In the previous section, effective assault frequency parameter ν_e is obtained and half-lives calculated using such parameter are in agreement with the experimental data. In this section, alpha decay half-lives of $^{198-220}$Rn isotopes are calculated using effective assault frequency ν_e discussed in previous section. First of all, the Q-value is calculated for α decay channel from Rn (Z = 84) isotopes. The calculated Q-value is plotted as function of neutron number of parent nucleus N_2 in figure.3.10. It can be observed from the figure that the Q-value is minimum for N = 126 and maximum for N=128, hence the importance of shell effects is evident for Rn isotopes. As a next step, the effective assault frequency ν_e and the penetration probability P is calculated and plotted as a function of neutron number N_2 and shown in figure.3.11.(a) and (b). The ν_e parameter varies linearly for N $\leq$ 126 and have parabolic

variation in case of N $<$ 126. The calculated penetration probability is minimum nearby N=126. After calculation of ν_e and penetration probability P, decay half-lives are calculated and a comparison is made the experimental results as shown in table 3.3. The calculated neck length parameter and the Q value are also shown in the table. The calculated results are in nice agreement with the experimental data [51]. The PCM evaluated decay half lives of Rn isotopes are framed with respect to the neutron number of the parent nucleus N in figure.3.12. The decay half-lives is higher for N=126, so the importance of shell closure effects is emphsised. The effective assault frequency parameter ν_e successfully addressed the experimental half-lives and the shell closure effects. Hence, we may incorporate such parameter to find the alpha decay half-lives of the radioactive nuclei.

3.3 Summary

Summarizing, the preformed cluster model (PCM) is employed for the α decay analysis of $^{188-218}$Po isotopes. The barrier characteristics of the α decay channel are studied with and without the inclusion of surface diffuseness parameter. The fragmentation structure of ^{188}Po,^{202}Po and ^{218}Po isotopes is explored, where α particle is found as the most probable decay fragment for the chosen set of Po isotopes. The preformation probability , barrier penetration probability and assault frequency (classical and quantum) are calculated and influence of neutron shell closure of the parent nucleus is explored. The PCM calculated P_0, P and ν is compared with the different theoretical approaches. The classical mode of the assault frequency (ν_c) depends on the Q value of the decay channel and the quantum mechanical mode (ν_q) depends on the global quantum number. The decay half-lives of alpha emission are calculated using both choices of assault frequency and a comparison is made with the results of CPPM, ADF, UDL, SLH, SLB, SemFIS and with the available experimental data .

The deformed (β_2) choice of the decaying fragments gives better agreement with the experimental data as compared to the spherical choice. The PCM calculated α decay life-time is found maximum nearby N=126. The verification of G-N law is made using the calculated decay half-lives and its dependency on the Q value of the decay channel is explored. The effective assault frequency parameter ν_e is obtained using P_0 and the quantum assault fre-

quency (ν_q). The alpha decay half-lives are calculated using ν_e and found in nice agreement with experimental results for the Po and Rn isotopes.

After the exploration of the α decay mode, our next goal is to focus on the other probable spontaneous decay modes such as CR, HPR and the SF. In next chapter, comprehensive analysis of these decay modes is made and relative relative comparison is worked out in view of alpha decay.

Bibliography

[1] Hourani et al., Annales de Physique (Paris) **14** , 311 (1989).

[2] D. N. Poenaru et al., Eur. Phys. L ,**118**,22001 (2017).

[3] D. N. Poenaru and R. A. Gherghescu, Phys. Rev. C **94**, 014309 (2016).

[4] Y.Z. Wang et al., Phys. Rev. C **92**, 064301 (2015).

[5] A. C. Wahl, At. Nucl. data table , **39**, 1-156 (1988).

[6] A. Parkhomenko and A. Sobiczewski, Acta Physica Polonica B , **36**, 1363 (2005).

[7] Yu Oganessian, Radioachemi. Acta , **99**, 429 (2011).

[8] J. H. Hamilton et al. , Ann. Rev. Nucl. Part. Sci., **63**, 383 (2013).

[9] D. N. Poenaru et al. , J. Phys. G: Nucl. Part. Phys. **32**, 1223 (2006).

[10] A. Staszczak et al. , Phys. Rev. C **87**, 024320 (2013).

[11] D. N. Poenaru and R. A. Gherghescu,J. Phys. G: Nucl. Part. Phys. **41**, 125104 (2014).

[12] D. N. Poenaru and R. A. Gherghescu, Phys. Rev. C **94**, 014309 (2016).

[13] D. N. Poenaru et al., Eur. Phys. J. A. **54**, 14 (2018).

[14] L. Capponi et al., Phys. Rev. C **94**, 024314 (2016).

[15] D. N. Poenaru and W. Greiner, Handbook of Nuclear properties, (clarendon press, Oxford) (1996).

[16] D. N. Poenaru , Nuclear decay modes, (Institute of Physics Publishing, Bristol) (1996).

[17] D. N. Poenaru et al.,J. Phys. G: Nucl. Part. Phys. **32**, 1223 (2006).

[18] D. T. Akrawy et al., Nucl. Phys. A **1021**, 122419 (2022).

[19] H. B. Yang et al., Phys. Rev. C **105**, L051302 (2022).

[20] A. N. Bezbakh, Phys. Rev. C **105**, 054305 (2022).

[21] K. P. Santosh et al., Phys. Rev. C **105**, 054605 (2022).

[22] D. N. Poenaru et al., Computer Physics Communications **25**, 297 (1982).

[23] D. T. Akrawy, D. N. Poenaru J. Phys. G: Nucl. Part. Phys. **44**, 105105 (2017).

[24] D. N. Poenaru et. al., Eur. Phys. J. A,**54**, 14 (2018).

[25] D. N. Poenaru and R. A. Gherghescu, Phys. Rev. C **97**, 044621 (2018).

[26] K. Varga et. al., Phys. Rev. L **69**, 37 (1992).

[27] I. Ahmad et al., Phys. Rev. C **8**, 2 (1973).

[28] D. N. Poenaru and R. A. Gherghescu , Eur. Phys. L **124**, 52001 (2018).

[29] G. Royer, R.A. Gherghescu , Nucl. Phys. A **699**, 479 (2002).

[30] Na. Na. Ma.,et. al. ,Chinese Physics C, **45**, 024105 (2021).

[31] Jun-Gang Deng, et. al. ,Phys. Rev. C **97**, 044322 (2021).

[32] Dong Bai ,et. al. ,Chinese Physics C, **42**, 124102 (2018).

[33] D. N. Poenaru, et. al., Phys. Rev. C **32**, 2 (1985).

[34] D. N. Poenaru, et. al., At. Data Nucl. Data Tables **34** 423 (1986).

[35] A. Kaur, N. Sharma, M. k. Sharma Phys. Rev. C **103**, 034618 (2021).

[36] N. Sharma ,A. Kaur, M. k. Sharma Phys. Rev. C **102**, 064603 (2020).

[37] S. S. Malik and Raj K. Gupta, Phys. Rev. C **39**,1992 (1989).

[38] K. Sharma, G. Sawhney, and M. K. Sharma , Phys. Rev. C **96**, 054307(2017).

[39] K. Sharma, et. al. , Nucl. Phys. A **972**, 1-17 (2018).

[40] R.K. Gupta and W. Greiner, Int. J. Mod. Phys. E. **03**, 335 (2) (1994).

[41] H. F. Zhang , *et. al.* , Phys. Rev. C **84**, 027303 (2011).

[42] V. Yu. Denisov and A. Khudenko, At. Data Nucl. Data Tables **95** 815 (2009).

[43] V. Yu. Denisov and A. Khudenko, Phys. Rev. C **80**, 034603 (2009).

[44] N. Sharma and M. K. Sharma, Phys. Rev. C **106**, 034608 (2022).

[45] G. Süssmann, Z. Phys. A **274**, 145 (1975).

[46] S. Dahmardeh, A. Alavi, V. Dehghani , **963**, 68 (2017).

[47] G. G. Adamian , Phys. Rev. C **90**, 03422 (2014).

[48] R. K. Gupta, S. Singh, R. K. Puri, A. Sandulescu, J. Phys. G Nucl. Part. Phys. **18**, 1533 (1992).

[49] M. Ismail et al., J. Phys. G: Nucl. Part. Phys. 47 , 055105 (2020).

[50] H. F. Zhang and G. Royer, Phys. Rev. C **77**, 054318 (2008).

[51] S. B. Duarte, et al., At. Data Nucl. Data Tables **80**, 235 (2002).

[52] D.N. Poenaru, E. Hourany, W. Greiner, in: D.N. Poenaru (Ed.), Nuclear Decay Modes, Institute of Physics Publishing, Bristol, UK, pp. 204–236, Ch. 4. (1996).

[53] D.N. Poenaru, I.H. Plonski, W. Greiner, Phys. Rev. C **74**,014312 (2006) .

[54] D.T. Akrawy, D.N. Poenaru, arXiv:1702.05598.

[55] C. Qi, F.R. Xu, R.J. Liotta, R. Wyss, Phys. Rev. Lett. **103** 072501,(2009).

[56] C. Qi, F.R. Xu, R.J. Liotta, R. Wyss, M.Y. Zhang, D. Hu, Phys. Rev. C **80**, 044326 (2009).

[57] B.A. Brown, Phys. Rev. C **46**,811 (1992).

[58] M. Horoi, J. Phys. G, Nucl. Part. Phys. **30**,945(2004) .

[59] S.S. Hosseini et al., Nucl. Phys. A **970**,259 (2018).

[60] M. Greiner and W. Scheid, J. Phys. G **12**, L229 (1986).

Chapter 4

Comparative analysis of different ground state decay mechanisms

In the previous chapter, α decay analysis of the Po isotopes was made using preformed cluster model (PCM), and significant role of the shell effects are explored using the preformation yield, barrier penetration probability and the classical and quantum mechanical impinging frequencies. In addition to the α decay mechanism, a radioactive nucleus may disintegrate through many other probable decay modes such as the cluster radioactivity (CR), heavy particle radioactivity (HPR) and the spontaneous fission (SF) etc. After the α decay analysis in the previous chapter, this part of the thesis includes a comprehensive analysis of CR, HPR and SF decay modes along with the α decay mechanism. A comparative analysis of all these decay modes is made using two kind of nuclear potentials. The detailed analysis of the present chapter is given below :

4.1 Introduction

After the discovery of radioactivity by Becquerel [1] numerous radioactive nuclei were detected, and vast understanding of different kind of radioactive decays was developed. It has been observed that the nuclei of actinide region are radioactive, and exhibit α-decay, cluster emission, heavy particle radioactivity (HPR) and spontaneous fission (SF) [2–7]. The dominance of one or more such decay modes rely on the binding energy of the parent nucleus and the fragmentation structure associated with it. After the establishment of the α-disintegration and spontaneous fission (SF) processes which are the traditional decay mechanisms of the unstable nuclei, cluster decay mode also known as cluster radioactivity (CR) came into existence in 1980 [4, 5]. In this process, the radioactive nucleus decays via fragments heavier than the α-particle but smaller than the lightest fission fragment. Till

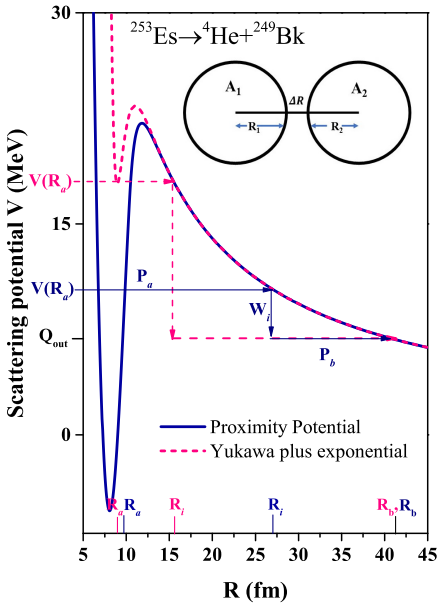

Figure 4.1: The binary interaction potential for α-decay of ^{253}Es nucleus for two kind of nuclear potentails, i.e., Yukawa plus exponential and proximity potentials. Also, the schematic representation of all the parameters is given.

now, different clusters such as ^{14}C,^{20}O,^{23}F,^{24}Ne,^{26}Ne, ^{28}Mg,^{30}Mg,^{32}Si,^{34}Si are detected experimentally. Different models are introduced to study the cluster emergence from a radioactive nucleus. Unified fission model was developed where the cluster is supposed to be in overlap region and the behaviour of the scattering potential is considered to be uniform throughout within the overlapping region (beyond touching state). The decay half-lives are calculated by studying the overlapping region and penetrating region [8]. Similarly, the cluster decay mode is studied using different models such as the Analytical Super-Asymmetric Fission Model (ASAFM) , preformed cluster model(PCM), Coulomb and proximity potential model (CPPM) and the universal decay formula (UDL), etc. [9–18]. Recently, another decay mode was predicted where the size of decaying fragments is heavier than CR fragment and lighter than fission fragment, and known as heavy particle radioactivity (HPR) [6, 7]. After the establishment of HPR, Santosh *et al.* also studied this mode using CPPM [19] for nuclei having Z=116-124, and the calculated results are compared with UDL. Similarly, analysis of the HPR mode was made for Z=113, 115 and 117 nuclei using PCM [20] and the importance of the nuclear proximity potentials is explored in view of HPR. The radioactive nucleus may opt any of these decay modes, hence it will be of interest to make a comparative analysis of these ground state emission processes.

This chapter aims to focus on the investigation of decay dynamics of ^{253}Es radioactive nucleus [21]. Till date, seventeen isotopes of Einsteinium nucleus are discovered, i.e. A=241-257, amongest a probable list of about hundred isotopes [22]. The main properties of the ^{253}Es nucleus (opted in present analysis), are fragment mass distribution, and half-lives of α decay, CR, HPR and the binary SF processes. In the present work, these binary decay mechanisms are analyzed using the framework of the preformed cluster model (PCM) [2,23]. In this work, ^{253}Es nucleus is of interest because some relevant data on α-decay, spontaneous fission processes is available. It is relevant to note that the half-lives of SF of the ^{253}Es nucleus is much higher as compared to the that for α-decay. Hence, it has been difficult to obtain sufficiently strong sources for study because of the extremely high alpha decay rates. The dynamic calculations incorporating both fragmentation potential and the preformation probability of the outgoing fragments, and penetration probability of fragments are expected to impart useful insight for the better understanding of aforementioned phenomena. Hence, the prime objectives of present work is (i) to explore the binary fragmentation potential and preformation probability distribution for the competing analysis of α-decay, CR, HPR and SF processes, (ii) to identify the decaying fragments and calculate their half-lives for all considered binary decay processes and compare with the experimental and other theoretical observations. The overview of this chapter is as per the following: the fragmentation analysis of ^{253}Es nucleus using fragmentation potential, preformation probability, penetration probability and the PCM calculated decay half-lives is carried out in section 4.2. The observations and conclusions drawn are outlined in section 4.3. The work presented in this chapter is published in the ref [24]

4.2 Calculations and results

In this section, theoretical investigation of the binary decay mechanism of ^{253}Es nucleus is made using the preformed cluster model (PCM). First of all, the competing analysis is carried out for various decay modes of ^{253}Es such as α decay, CR, HPR and SF. The fragmentation structure is analyzed to explore the probable fragment emission processes. The decaying fragments are identified and their corresponding half-lives are calculated, and compared with available experimental and other theoretical observations. It is worth mentioning here that

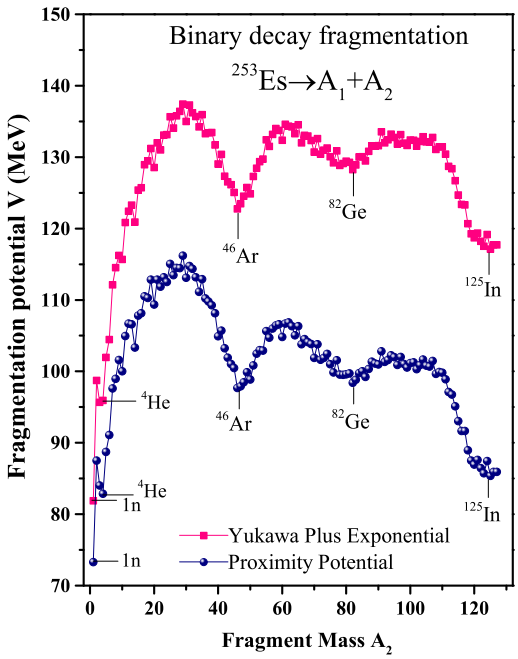

Figure 4.2: Binary fragmentation potential V(MeV) with respect to the fragment mass A_2 for ^{253}Es nucleus calculated using Yukawa plus exponential and proximity potential. The deepest minima of fragmentation potential are also marked.

such fragment identification is not available in the reported experiments for cluster, HPR and SF region, also no experimental information is available for the half-lives of CR and HPR channels. The calculations are made using two kind of nuclear potentials, i.e., Yukawa plus exponential and proximity potentials within the framework of PCM.

First of all, the barrier characteristics for the α-decay of ^{253}Es nucleus are analyzed by plotting scattering potential in Fig. 4.1 for both Yukawa plus exponential and proximity nuclear potential. It is evident that both the potentials show different barrier characteristics. The obtained value of the position of the barrier and height of the barrier are distinct for both cases, and hence the penetrability gets modify accordingly. The Coulomb barrier is smaller for the case of proximity potential, and one can say that the probability of α-emission is higher for the same. The collective illustration of a nuclear dynamics is exploited by studying the fragmentation potential and preformation probability. In order to examine the dynamics engaged with the radioactive nucleus, the collective potential energy (or fragmentation potential) is calculated, which is the key ingredient to the Schrödinger equation (see Eq. (2.18) of chapter 2). By studying the deep valleys in the fragmentation potential at

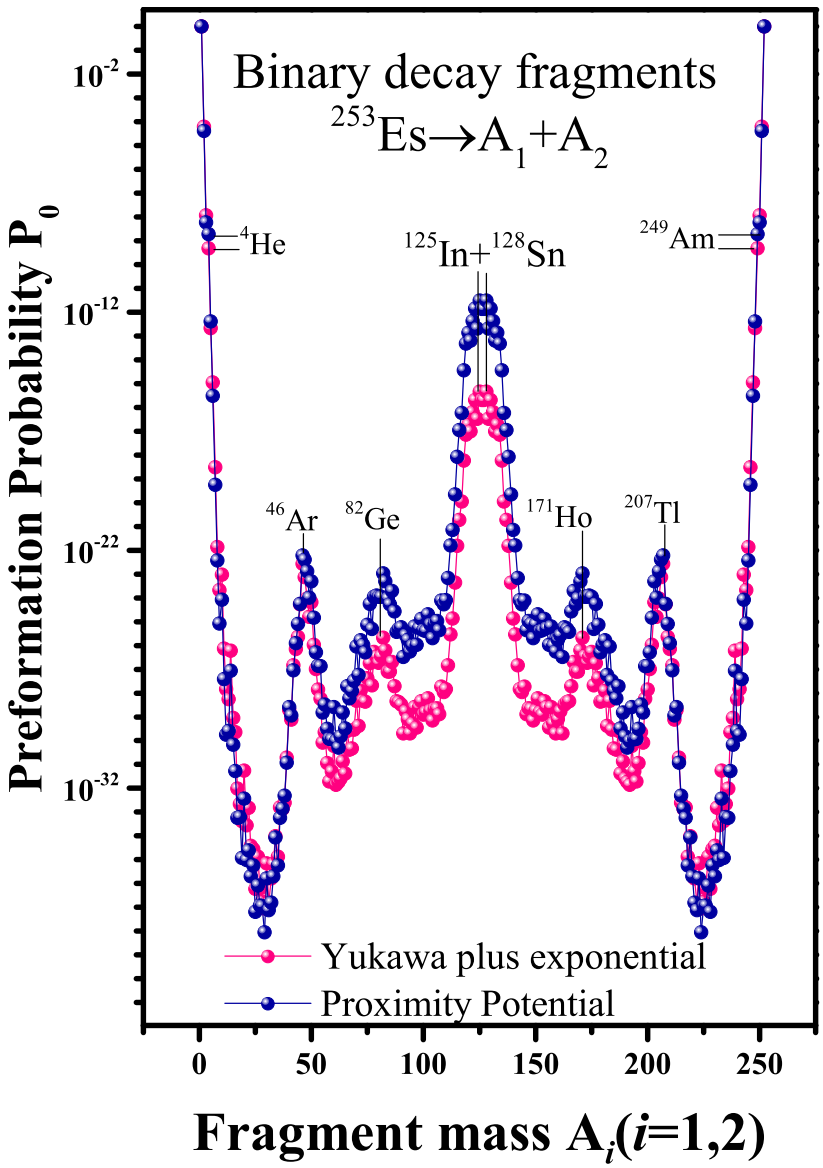

Figure 4.3: Preformation probability P_0 with respect to the fragment mass A_i for the ^{253}Es nucleus calculated using Yukawa plus exponential and proximity potential.

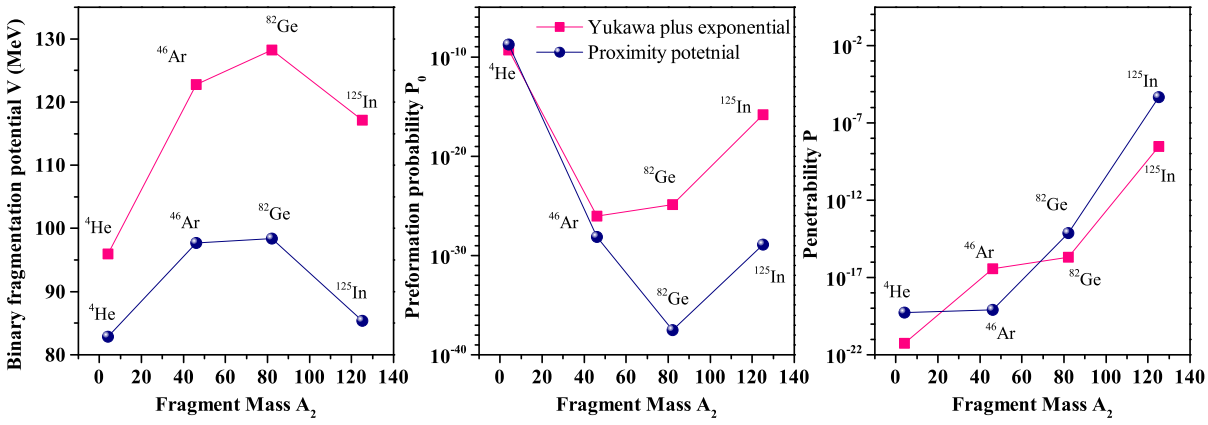

Figure 4.4: The competitive analysis of all the binary decay mechanisms (α, CR, HPR and SF) via (a) binary fragmentation potential V(MeV), (b) preformation probability P_0, and (c) penetrability P with respect to the fragment mass A_2.

all η-values, the relative stability of decaying fragments can be estimated. Therefore, the binary fragmentation potential $V_R(\eta)$(MeV) of ^{253}Es is calculated and the results are plotted in figure 4.1. The investigation of fragmentation potential is carried out for both Yukawa plus exponential and proximity nuclear potential. A deep analysis of the prominent dips in the fragmentation plot leads to the observation that most preferred decay fragments are same for both choices of nuclear potentials. However, there is a significant difference in the magnitude of fragmentation potential. It is evident from figure 4.2 that, the clusters/fragments corresponding to the deepest minima of the fragmentation potential are $1n$, ^{4}He, ^{46}Ar, ^{82}Ge and ^{125}In. The α-particle (^{4}He) along with the $1n$ are having the lower fragmentation potential. However, the present work aims primarily to explore the relative abundance of radioactive processes, so the α-decay is compared with the heavier cluster emission. As stated above, the decay fragments for CR, HPR and SF channels are identified, respectively, as ^{46}Ar, ^{82}Ge and ^{125}In (along with complementary fragments). Fig. 4.3 represents the PCM-calculated preformation probability P_0 with respect to the fragment mass A_i for binary decays of ^{253}Es nucleus with the help of the Yukawa plus exponential and proximity potential. The minima in the fragmentation structure corresponds to the maxima in the preformation profile (P_0). This indicates that the fragment having highest value of preformation probability forms the most favorable fragment pair in the exit channel. The decaying fragments are identified and are marked in the preformation plot. The spontaneous fission decay of ^{253}Es nucleus advocates symmetric fragmentation (^{125}In+^{128}Sn channel), and this choice of the most probable fission fragments triggered the importance of shell closure (lie nearby Z=50). The reason

The calculated decay half-lives of the binary decay mechanisms (α, CR, HPR and SF) of the ^{253}Es nucleus are compared with the available experimental data [25, 26] and other theoretical reference [27]. The optimized value of ΔR with other calculated quantities are also presented in the table.

Decay	Decay	Q value	ΔR (fm)		Half-lives log$T_{1/2}$ (sec.)			
mode	channel	(MeV)	Yukawa	Proximity	Yukawa (PCM)	Proximity (PCM)	Expt.	Theoretical
Alpha	^{4}He+^{249}Bk	6.75	-0.20	0.75	9.0	6.45	6.2	7.16 [27]
Cluster	^{46}Ar+^{207}Tl	128.7	0.70	-0.85	20.81	25.54	-	24.37 [27]
HPR	^{82}Ge+^{171}Ho	199.2	-0.40	-1.0	19.94	30.03	-	-
SF	^{125}In+^{128}Sn	243.3	-0.40	-1.0	2.77	12.65	13.29	-

behind the emergence of predicted cluster/fragments is apparently due to the magicity of the corresponding daughter products in all the decay channels.

The competing nature of all the four decay channels of ^{253}Es can be seen from figures 4.4(a-c), which shows the behaviour of fragmentation potential, preformation probability P_0 and barrier penetrability P (calculated at corresponding fitted ΔR's). It is observed from figure 4.4 (a) that α and spontaneous fission fragment (^{125}Sn) have lower magnitude of fragmentation potential than the cluster (^{46}Ar) and heavier fragment (^{82}Ge). Consequently, the magnitude of P_0 is large for α and SF fragment than other two decay channels, which means the probability of α emission and SF decay channels is higher for ^{253}Es nucleus. However, fig. 4.4(c) depicts that the barrier penetrability rises with respect to increase in the mass number of the decaying fragment. It may be noted from the figure that proximity and Yukawa nuclear potentials show similar structural behavior for all kind of binary decay processes (also shown in Fig. 4.2). However, there is a significant difference in magnitude. Knowing that half-lives are the combined effect of preformation probability P_0 and penetrability P, the PCM-calculated results are presented in table 1. The half-lives of α and fission fragment are smaller than cluster and heavy fragment. However, the half-lives for α and SF channels show nice agreement with the experiment measurements [25, 26] with the use of proximity potential. This is due to the different barrier characteristics of both the potentials as discussed in figure 4.1. The Q-value and the optimized values of neck-length parameter for the binary decay mechanisms are presented in table 1. The comparison of PCM-calculated half-lives with other theoretical observations [27] is also made.

4.3 Conclusion

Here, preformed cluster model (PCM) is employed to study different binary decay processes of the ^{253}Es radioactive nucleus. The binary decay mechanisms (such as α, cluster, HPR, SF), are explored using using two kinds of attractive nuclear potentials i.e. Yukawa plus exponential and proximity potential. The barrier characteristics for the α decay process are compared using both nuclear potentials. The Coulomb barrier is smaller for the case of proximity potential, hence the α particle emission probability is higher for this potential. After the barrier analysis, the fragmentation potential and the preformation probability

is calculated and most probable decaying fragments are identified. The identified decay fragments are similar for both of the nuclear potentials but there is significant change in the magnitude of the fragmentation potential. The identified most probable decaying fragments depict the importance of Shell closure effect. The decay half-lives are calculated for all decay mechanisms (α, cluster, HPR, SF) for both nuclear potentials. The PCM-calculated half-lives of α and SF channels show nice agreement with experimental results using proximity potential. However, the half-lives are predicted for cluster and heavy particle radioactivity. A comparison of the fragmentation potential, preformation probability (p_0) and the barrier penetration probability (P) of all binary decay mechanisms is made where alpha decay and SF are found as prominent decay modes for both choices of the nuclear potentials.

In this chapter, a comparative analysis of various ground state binary decay modes is made using the spherical choice of the decaying fragments. As a next step, relevant role of the deformations and geometrical configurations (cold and elongated) is explored in the next chapter. The mass distributions of the fermium (Fm) isotopes are examined for the spherical, hot and cold configuration choices of the decaying fragments and comparison is made with the available experimental data.

Bibliography

[1] A. Allisy, Radiation Protection Dosimetry **68**, 3 (1996).

[2] K. Sharma, G. Sawhney, and M. K. Sharma, Phys. Rev. C **96**, 054307 (2017).

[3] A. Kaur, G. Sawhney, and M. K. Sharma, Int. J. Mod. Phys. E **27**, 1850043 (2018).

[4] A. Sandulescu, D. N. Poenaru, and W. Greiner, Sov. J. Nucl. **11**, 528 (1980).

[5] H. J. Rose and G. A. Jones, Nature (London) **307**, 245 (1984).

[6] D. N. Poenaru, R. A. Gherghescu, and W. Greiner, Phys. Rev. Lett. **107**, 062503 (2011).

[7] D. N. Poenaru, R. A. Gherghescu, and W. Greiner, Phys. Rev. C **85**, 034615 (2012).

[8] D. N. Poenaru and W. Greiner, Physica Scripta. **44**, 427, (1991).

[9] A. Sandulescu, D. N. Poenaru and W. Greiner, Sov. J. Nucl. **11**, 528 (1980).

[10] D. N. Poenaru, M. Ivascu and W. Greiner, Int. J. Rad. Appl. Instrum. D, **12**, No. 1-6, pp. 313-316 (1986).

[11] D. N. Poenaru, W. Greiner and E. Hourani, Phys. Rev. C **51**, 2 (1995).

[12] C. Qi, F. R. Xu, R.J. Liotta and R. Wyss, Phys. Rev. Lett. **103**, 072501 (2009).

[13] X. Bao, H. F. Zhang, J. M. Dong, J. Q. Li and H. F. Zhang, Phys. Rev. C **89**, 067301 (2014).

[14] G. Royer, R. Moustabchir, Nucl. Phys. A **683**, 182 (2001).

[15] K. P. Santhosh and R. K. Biju, Ann. of Phys. **334**, 280287 (2013).

[16] G. Sawhney, M. K. Sharma, R. K. Gupta, Phys. Rev. C **83**, 064610 (2011).

[17] R. Kumar, M. K. Sharma, Phys. Rev. C **85**, 054612 (2012).

[18] R. Kumar, M. K. Sharma, Phys. Rev. C **85**, 054612 (2012).

[19] K.P.Santosh and B. Priyanka, Nucl. Phys. A **929**, 20, (2014).

[20] G. Sawhney *et al.*, Eur. Phys. J A **50**, 175, (2014).

[21] S. G. Thompson, A. Ghiorso, B. G. Harvey, and G. R. Choppin, Phys. Rev. **93**, 908 (1954).

[22] D. Meierfrankenfeld, A. Burya, and M. Thoennessen, Atomic Data and Nuclear Data Tables **97**, 134 (2011).

[23] G. Sawhney, K. Sandhu, M. K. Sharma, and Raj K. Gupta, Eur. Phys. J. A **50**, 175 (2014).

[24] N. Sharma, A. Kaur and M. K. Sharma, Phys. Rev. C **102**, 064603 (2020).

[25] https://www.nndc.bnl.gov/

[26] N. E. Holden and D. C. Hoffman, Pure Appl. Chem. **72**, 1525 (2000).

[27] G. M. Carmel, V. Bai, and R. N. Agnes, Pramana J. Phys. **88**, 43 (2017).

Chapter 5

Effect of compact and elongated configurations in the spontaneous fission (SF)

In the previous chapter comprehensive analysis of different binary decay modes is made using preformed cluster model (PCM). The mass asymmetry coordinate and relative separation coordinates are employed for the comparative analysis of the probable decay modes. All of these investigations are made using the spherical choice of the decaying fragments. As an extension of this work, role of the deformations and orientations (compact and elongated) is explored in the present chapter. The detailed description of the chapter is given below.

5.1 Introduction

Nuclear fission process, the division of atomic nucleus into two or more fragments, has a significant role in the generation of electric-power, stability of super-heavy nuclei, termination of r-nucleosynthesis process and the generation of exotic nuclear isotopes. In addition, the fission decay products have many industrial and medical applications. It is therefore important to have an appropriate knowledge of the fission fragment mass distribution of heavy nuclei. Several experimental and theoretical efforts have been made to analyze the properties of nascent fission fragments, and it has been observed that the macro-microscopic effects play an important role in the fission dynamics [1–8].

The literature shows some exceptional observations [3–5, 9, 10] in reference to the fission fragment mass distributions. For example, ^{180}Hg nucleus gets disintegrated via asymmetric fragmentation, however, it is supposed to decay via symmetric fission fragments, i.e., ^{90}Zr+^{90}Zr having magic neutron number N=50 [3, 4]. The n-induced fission of ^{238}U nucleus at higher energies (E_n=50-60 MeV) have maintained the two humped mass asymmetric distribution, where shell effects are expected to be vanished at such higher energies [5].

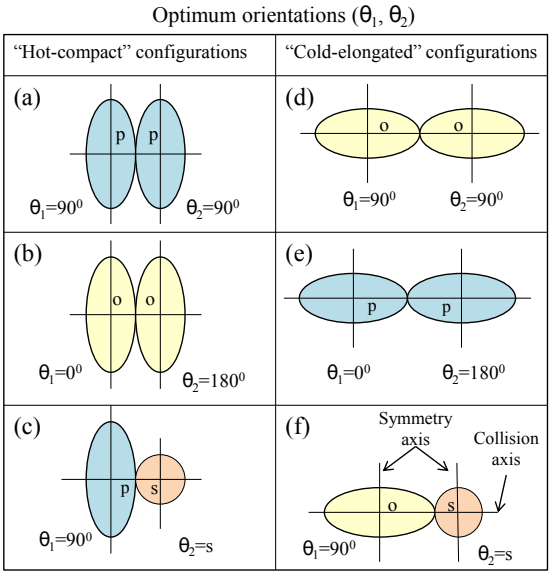

Figure 5.1: A pictorial representation of hot-compact (a-c) and cold-elongated (d-f) configurations for prolate (p), oblate (o) and spherical (s) shapes of nuclei. See ref. [12] for further details.

Moreover, the actinides are known to have an asymmetric fission pattern, but the first observation of a transition from asymmetric to symmetric fission has been measured in the region of mass A=256-258 of Fm isotopes [9,10]. Such competing emergence among the symmetric and asymmetric fission is mainly associated with the deformed magic shell effects [2]. Apart from this, the tip-to-tip (equatorial 'or' elongated) and side-to-side (polar 'or' compact) configurations of the nuclei has great impact on formation and the decay dynamics of a nucleus [11,12]. In view of above, we require a thorough analysis of fission fragment mass distributions in reference to the macroscopic-microscopic effects, deformations, orientations, angular momentum and energy dependence of fission observables for wide isotopic range. In the present chapter, the spontaneous fission (SF) and induced fission (IF) of fermium (Fm) isotopes having even mass number A=242-260 have been studied. These nuclei are of interest as they may exhibit a symmetric profile due to presence of two proton magic Sn (Z=50) mass-symmetric nuclei. Earlier, our group have studied the break up of ^{254}Fm* compound nucleus (CN) established in ^{11}B+^{243}Am reaction at wide excitation energy range [13]. The obtained results triggered that the deformation and orientation effects play crucial role in fission dynamics [13].

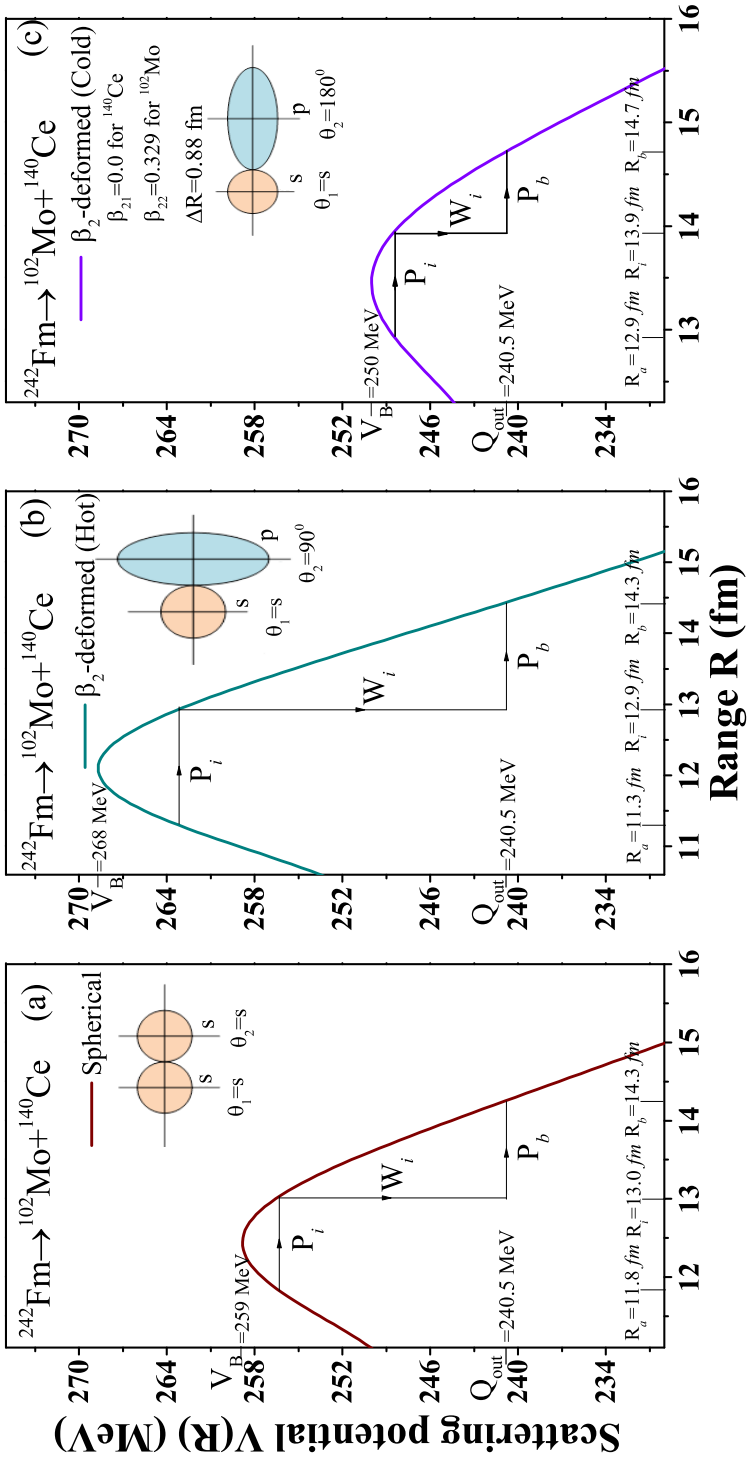

Figure 5.2: PCM-calculated scattering 'or' interaction potential for (a) spherical, (b) β_2-deformed hot-compact, and (c) β_2-deformed cold-elongated configurations for asymmetric spontaneous fission of ^{242}Fm nucleus.

To analyze the induced fission (IF) dynamics, we have extended this study to other isotopes, i.e., $^{242-260}$Fm* formed in ^{11}B+$^{231-249}$Am reactions at excitation energies E^{*}=5-42 MeV. The analysis of spontaneous fission and induced fission is worked out using the preformed cluster model (PCM) [14–17] and dynamical cluster-decay model (DCM) [18–22], respectively. The aim of the present chapter is (i) to analyze spontaneous as well as induced fission of Fm isotopes having mass number A=242-260, (ii) to examine the role of deformations and orientations of the interacting fragments in view of the structure of fragmentation potential V(η, R) and preformation probability (P_0) (iii) to investigate the impact of excitation energy (E^{*}), angular momentum (ℓ) and neutron (N) number of fissioning nuclei on fission fragment mass distributions, (iv) to study the possibility of multi-modal fission i.e. the presence of both symmetric fission and asymmetric fission in Fm isotopes, and (v) to recognize the nascent light (A_L) and heavy (A_H) fission fragments in order to analyze the role of spherical and deformed magic shell closure.

The present chapter is arranged as follows: The exploration of spontaneous fission and induced fission of Fm isotopes, and their corresponding discussions are presented in Section 5.2, and finally conclusion of the obtained results are summarized in the last section. The work presented in this chapter is published in the ref. [23]

5.2 Calculations and the results

5.2.1 Spontaneous fission of Fm isotopes

In PCM, the angular momentum and temperature effects are silent, however, the deformation effects are included up to quadrupole (β_2) deformations of fragments with optimum orientations of decay fragments. Depending on the prolate and oblate shapes (+ and - signs) of β_2-deformations, the orientation angles are optimally fixed, which result in the 'hot-compact' and 'cold-elongated' configurations as shown in Fig. 5.1, for detailed description of optimum orientations see Ref. [12]. The 'hot-compact' and 'cold-elongated' configurations are also known as equatorial (side-side) and polar (tip-tip) configurations, respectively. In this manuscript, we are denoting 'hot-compact' and 'cold-elongated' configurations as β_2-deformed (hot)

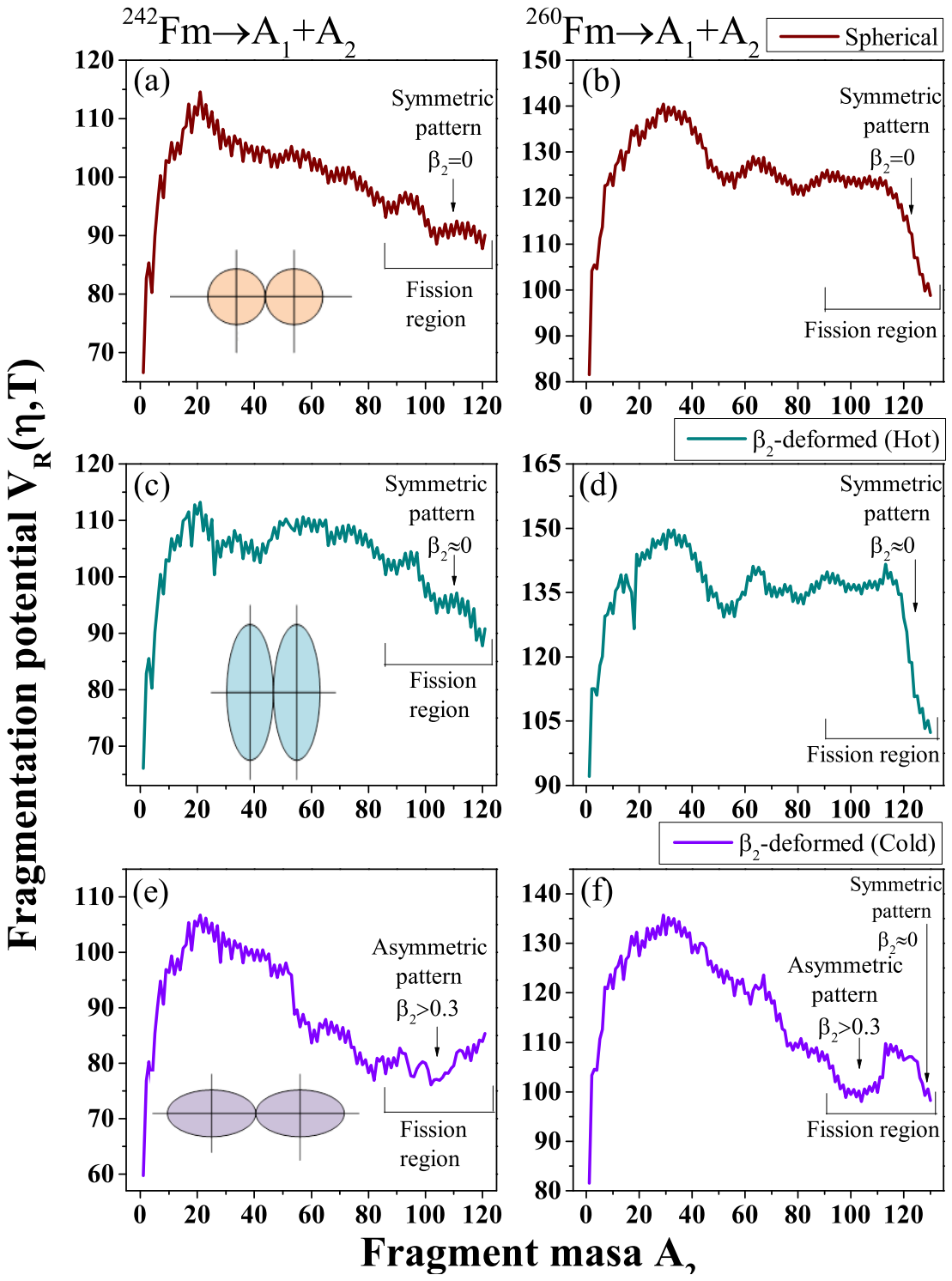

Figure 5.3: Collective fragmentation potential $V_R(\eta)$ of ^{242}Fm and ^{260}Fm nuclei for (a,b) the spherical, (c,d) the β_2-deformed (hot) and (e,f) β_2-deformed (cold) configurations. Fission region and related β_2-deformations are also marked.

Parent nucleus	Decay channel	ΔR(fm)	$\log_{10}T^{SF}_{1/2}$ (sec)	
			PCM	Expt.
		Spherical		
^{242}Fm	^{120}Sn+^{122}Sn	1.418	-1.586	-3.097
^{244}Fm	^{122}Sn+^{122}Sn	1.420	-1.600	-2.481
^{246}Fm	^{122}Sn+^{124}Sn	1.369	-0.826	0.903
^{248}Fm	^{124}Sn+^{124}Sn	1.372	5.247	4.556
^{250}Fm	^{124}Sn+^{126}Sn	1.000	7.353	7.402
^{252}Fm	^{126}Sn+^{126}Sn	0.640	9.606	9.596
^{254}Fm	^{126}Sn+^{128}Sn	0.640	7.291	7.294
^{256}Fm	^{128}Sn+^{128}Sn	0.653	4.023	4.019
^{258}Fm	^{128}Sn+^{130}Sn	1.100	-3.440	-3.432
^{260}Fm	^{130}Sn+^{130}Sn	0.725	-2.372	-2.397
		β_2-deformed		
^{242}Fm	^{102}Mo+^{140}Ce	0.880	-2.928	-3.097
^{244}Fm	^{98}Zr+^{146}Nd	0.760	-2.268	-2.481
^{246}Fm	^{98}Zr+^{148}Nd	0.480	0.860	0.903
^{248}Fm	^{98}Zr+^{150}Nd	0.180	4.767	4.556
^{250}Fm	^{100}Zr+^{150}Nd	0.015	7.397	7.402
^{252}Fm	^{100}Zr+^{152}Nd	0.001	7.615	9.596
^{254}Fm	^{102}Zr+^{152}Nd	0.083	6.228	7.294
^{256}Fm	^{102}Zr+^{154}Nd	0.274	2.455	4.019
^{258}Fm	^{102}Zr+^{156}Nd	0.660	-3.339	-3.432
	^{128}Sn+^{130}Sn	1.050	-3.439	
^{260}Fm	^{104}Zr+^{156}Nd	0.582	-2.324	-2.397
	^{130}Sn+^{130}Sn	0.670	-2.382	

and β_2-deformed (cold) orientations. First, the barrier characteristics are analyzed for the asymmetric spontaneous fission of ^{242}Fm$\rightarrow^{140}$Ce (β_{21}=0.0)+^{102}Me (β_{22}=0.329) nucleus in reference to these configurations. Figs. 5.2(a), 5.2(b) and 5.2(c) show the scattering potential V(R), respectively, for the choice of spherical fragments, β_2-deformed (hot), and β_2-deformed (cold) approaches. It is observed from figure that the barrier properties are significantly modified with the inclusion of deformations and orientation effects. The interaction radius is largest for the case of cold configurations and smallest for the hot configuration as evident from Figs. 5.1 and 5.2. Consequently, cold orientations correspond to the smallest interaction barrier and hot configurations to the largest interaction barrier. This means that such effects are highly important as they in turn modify the preformation probability P_0, barrier penetrability P, and hence the decay half-life.

For further analysis of fission valleys, the collective fragmentation potential $V_R(\eta)(A_2)$ of ^{242}Fm and ^{260}Fm fissioning nuclei is framed in Figs. 5.3(a-f) with respect to the light fragment mass (A_2) for the choice of spherical, β_2-deformed (hot) and β_2-deformed (cold) approaches. The structure of fission valleys is drastically modified with the incorporation of deformation effects. The probable fission region in the fragmentation structure is marked in the figure. If we focus on spherical approach (β_2=0 for each fragmentation), the fission dips indicate that the symmetric fragments are main contributors in the spontaneous fission of ^{242}Fm and ^{260}Fm parent nuclei, see Figs. 5.3(a) and 5.3(b). The contributed fission fragments of both nuclei in Figs. 5.3(c) and 5.3(d) also show the symmetric fission pattern for β_2-deformed hot configuration. However, the cold interactions in Figs. 5.3(e) and 5.3(f) show a dominance of asymmetric fission and multi-modal fission, respectively, for ^{242}Fm and ^{260}Fm nuclei. Here, multi-modal fission means the presence of both the symmetric fission and asymmetric fission.

It is clear from above analysis that the inclusion of hot or cold orientations cause significant influence on the fragment mass distribution, as the fragmentation potential depends on the deformation parameter and on the choice of radius vector. For β_2-deformed (hot) cases, the symmetric fission valleys in fragmentation potential are observed in the neighbourhood of spherical or nearly spherical fragments ($\beta_2\approx$0). However for cold configurations, the asymmetric minima in potential correspond to highly deformed fragments ($\beta_2>$0.3) where the symmteric one belong to spherical or nearly spherical nuclei ($\beta_2\approx$0). In hot orientations, the spherical decaying fragments have larger interaction radius than the β_2-deformed

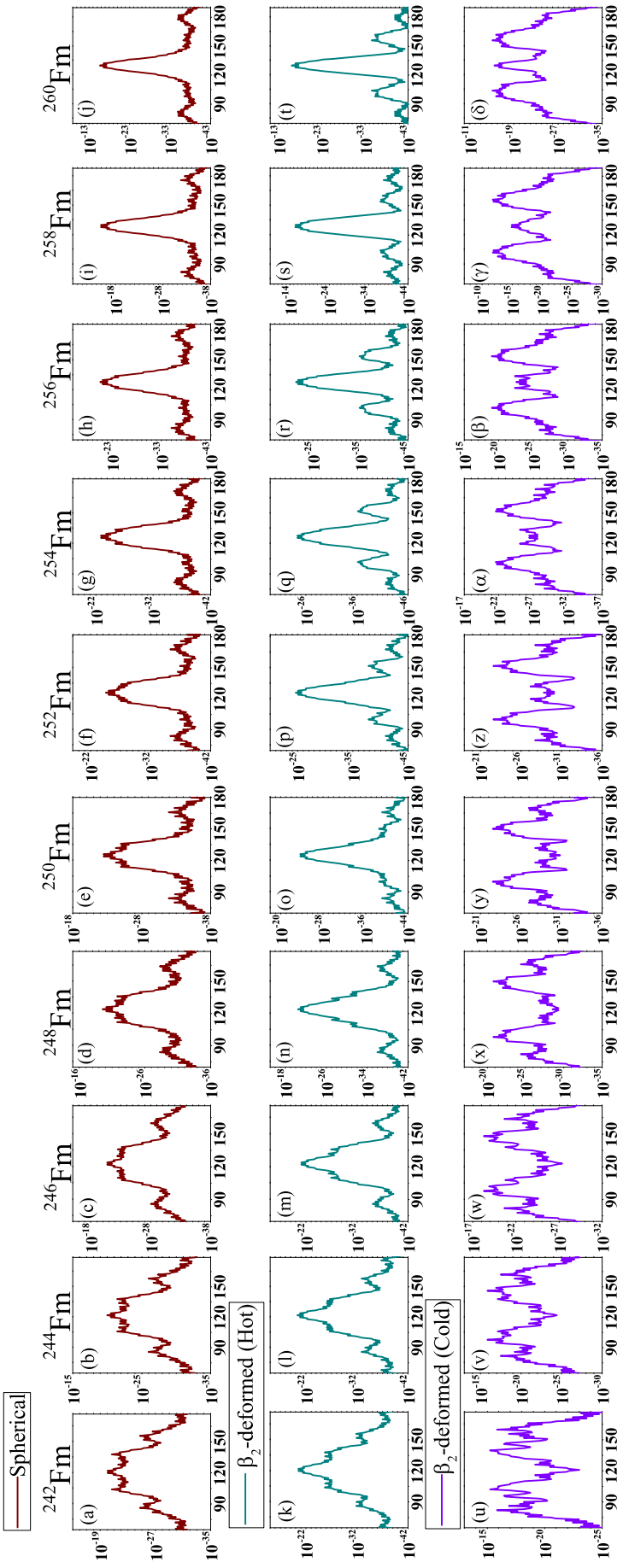

Figure 5.4: Preformation yield P_0 is plotted as a function of fission fragments of all considered Fm isotopes for (a-j) spherical fragments, (k-t) β_2-deformed hot-compact configurations, and (u-δ) β_2-deformed cold-elongated configurations.

fragments, and hence the fragmentation potential has smaller magnitude for spherical fragments, therefore we get the symmetric distribution for this case. On the other side, the cold-elongated interactions of highly deformed fragments result in the larger interaction radii leading to the lower fragmentation potential as compare to spherical fragments. As a consequence, the asymmetric fission becomes prominent for the case of cold-interactions. It will be of further interest to explore the cause and consequences of spherical emergence (symmetric) and deformed (asymmetric) fragments in the cold interaction criteria, for the case of ^{260}Fm nucleus.

For further analysis, the preformation probability P_0 of each isotope of Fm are shown in Figs. 5.4(a-j), 5.4(k-t) and 5.4(u-δ) for spherical, β_2-deformed (hot), and β_2-deformed (cold) approaches respectively. It is to be noted here that fragmentation potential further proceed as an input in the Schrödinger equation used to calculate the preformation probability P_0, and the valleys of fragmentation potential correspond to the peaks of preformation probability and vice versa. Overall, the mass distribution of $^{242-260}$Fm isotopes show symmetric pattern in fission region for spherical and β_2-deformed (hot) cases. However, symmetric peak becomes sharp with increase in neutron (N) number of Fm parent nucleus, for the inclusion of β_2-deformed hot orientations of the decay fragments. For β_2-deformed (cold) case, a transition from double peak to triple peak is observed as one goes from ^{242}Fm to ^{260}Fm fissioning nuclei. This indicates that β_2-deformed (cold) approach follows different fission decay path than the spherical and hot interactions. The results of preformation probability shown in Fig. 5.4 are in agreement with the ones plotted for fragmentation potential in Fig. 5.3. The lighter mass Fm isotopes exhibit the asymmetric spontaneous fission. However the mass distributions of heavier fermium isotope (^{260}Fm) seem to suggest the possibility of multi-modal spontaneous fission (that means the presence of the symmetric fission and asymmetric fission). This indicates that cold-elongated configuration results are in accordance with the experimental data of refs. [9, 10, 39].

In order to analyze the multi-modal fission of Fm isotopes, the positions of nascent fission fragments in proton (Z) and neutron (N) numbers, the most probable fission fragments are identified in reference to the peaks of preformation probability P_0. The most probable light (A_L) and heavy (A_H) fission fragments are listed in Table 5.2.1, and the Z and N number of light fission fragment (A_L) are framed in Figs. 5.5(a-b) with respect to the mass number

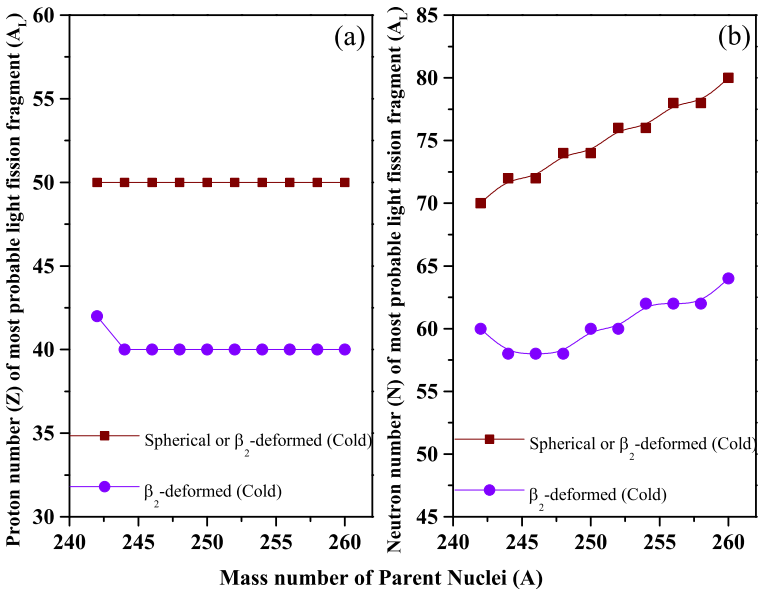

Figure 5.5: (a) Proton (Z), and (b) neutron (N) number of most preferred light fission fragments are plotted with respect to the mass of Fm spontaneous fissioning nuclei for spherical and β_2-deformed (cold) cases.

of parent nuclei for the spherical as well as the β_2-deformed (cold) approaches. The option of fission fragments for β_2-deformed (hot) case is same as that of spherical approach. The symmetric peaks for both spherical and hot interactions are mainly governed by the spherical magic shell closure of the proton number at Z=50, that means the $^{242-260}$Fm isotopes decay via isotopes of Tin (Sn).

The neutron number of these isotopes increases with mass number of the parent nuclei and approaches to the spherical neutron shell closure of N=82 for the heaviest considered isotope. For β_2-deformed (Cold) case, the Z number and N number of light asymmetric fission fragments lie in the neighbourhood of deformed magic shell closures of Z=38 and N=60,62. This indicates that deformed magic shell closures play important role for the case of cold-elongated configuration. However, the symmetric peak becomes more prominent in heavier mass ^{258,260}Fm nuclei, and belongs to the spherical doubly magic shell closures of the Sn (Z=50, N=82) nuclei. From Figs. 5.3-5.5, it may be concluded that the spherical and deformed magic shell closures along with the deformation and orientation degree of freedom play an important role in the division of fissioning nucleus.

The SF half-lives ($T_{1/2}^{SF}$) of identified fission fragments are calculated with the help of the'neck-length' parameter (ΔR) for spherical and β_2-deformed (cold) cases. Table 5.2.1

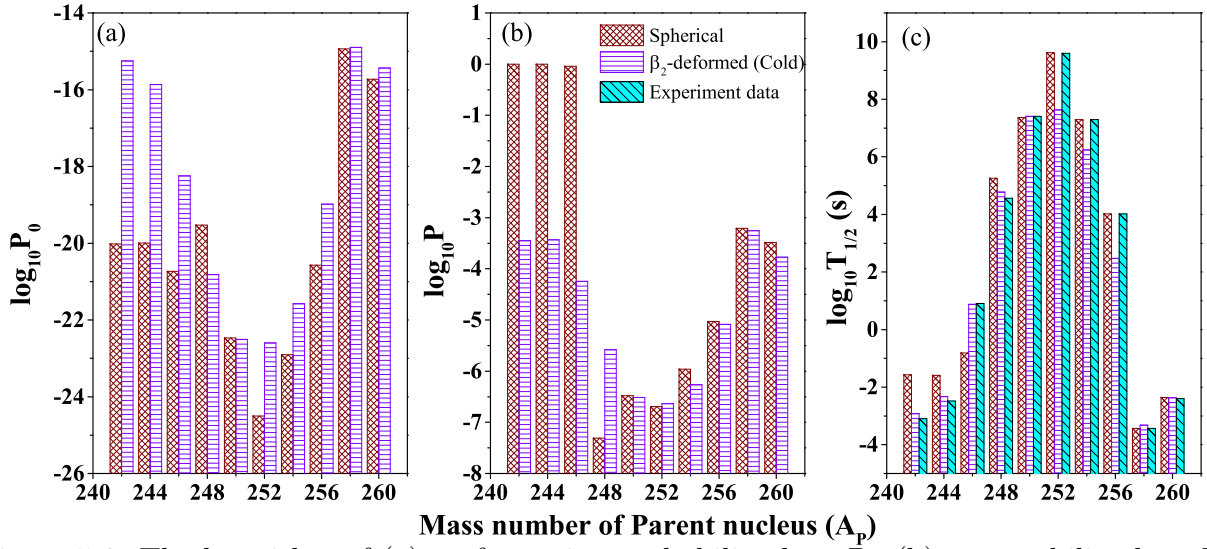

Figure 5.6: The logarithm of (a) preformation probability $log_{10}P_0$, (b) penetrability $log_{10}P$ and (c) SF half-lives $log_{10}T^{SF}_{1/2}$ (s) as a function of mass number of Fm isotopes for spherical, β_2-deformed (hot), β_2-deformed (cold) configurations.

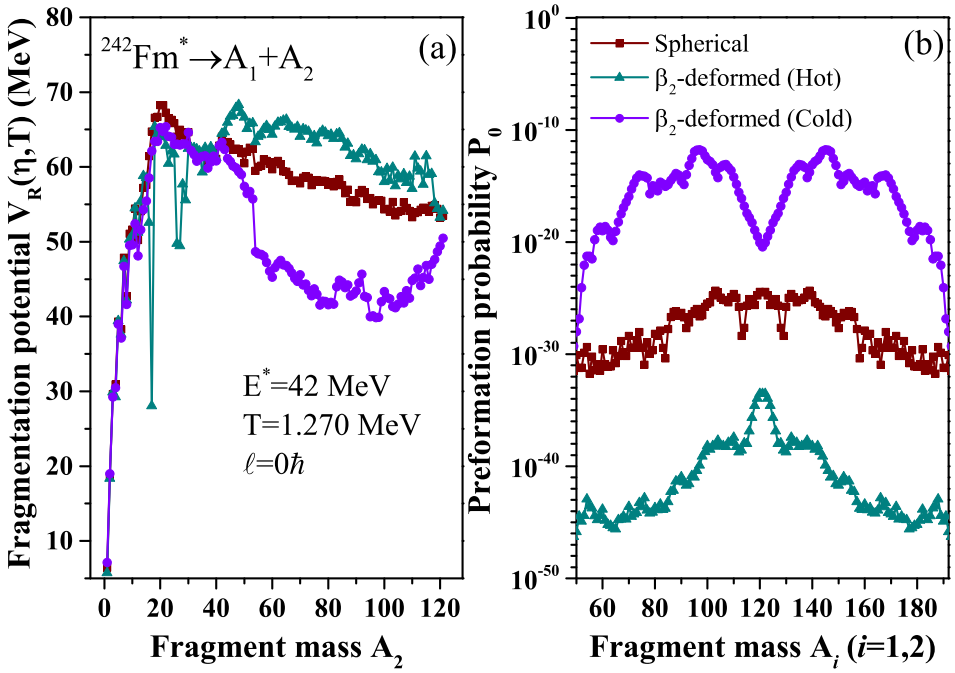

Figure 5.7: (a) The Fragmentation potential $V_R(\eta)$, and (b) the preformation probability P_0 of ^{242}Fm* nucleus plotted with respect to the fragment mass for the spherical, the β_2-deformed (hot), β_2-deformed (cold) configurations.

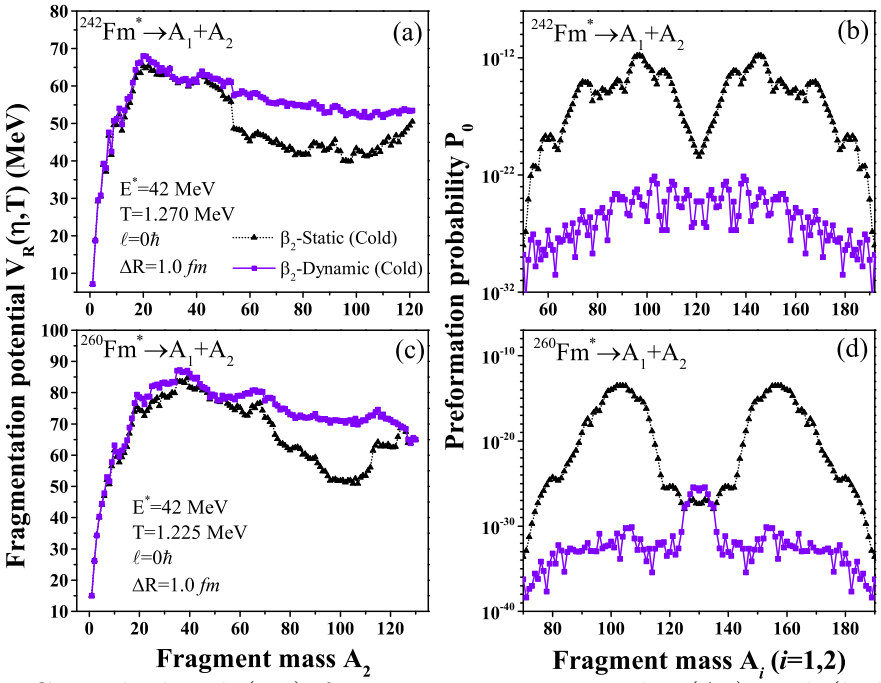

Figure 5.8: DCM-calculated (a,c) fragmentation potential V(A_2) and (b,d) preformation probability P_0 for ^{242}Fm* and ^{260}Fm* nuclei is plotted for static (T-independent) and dynamic (T-dependent) deformations for cold-orientationsx.

and Fig. 5.6 (c) represent the PCM-calculated half-lives which are in fair agreement with the experimental reference [38]. For case of ^{258,260} Fm nuclei, the half-lives are evaluated for both symmetric fission and asymmetric fission fragments as both nuclei show multi-modal fission in cold interactions. The fission half-lives, neck-length parameter along with the identified most probable fission fragments are listed in the Table 5.2.1. The magnitude of ΔR is small for cold interactions in comparison to the spherical approach. The decay half-life depends on the preformation probability P_0 and penetrability P as per equation (2.1). Figs. 5.6(a), 5.6(b) and 5.6(c) depict the $log_{10}P_0$, $log_{10}P$ and $log_{10}T^{SF}_{1/2}$ of most favorable fission fragments, respectively, with respect to the mass number of parent nuclei. It is clear from plot that $log_{10}T^{SF}_{1/2}$ show the opposite trend to $log_{10}P_0$ and $log_{10}P$. It is clearly evident from plot that when preformation and penetration probabilities are large, decay half-life is small and vice versa. This indicates that higher probability of fragments preformation and subsequent penetration lead to lower magnitude of the decay half life. This justifies the fact that the proper understanding of preformation factor and barrier penetrability is desirable for adequate addressal of decay half-lives of the SF mechanism.

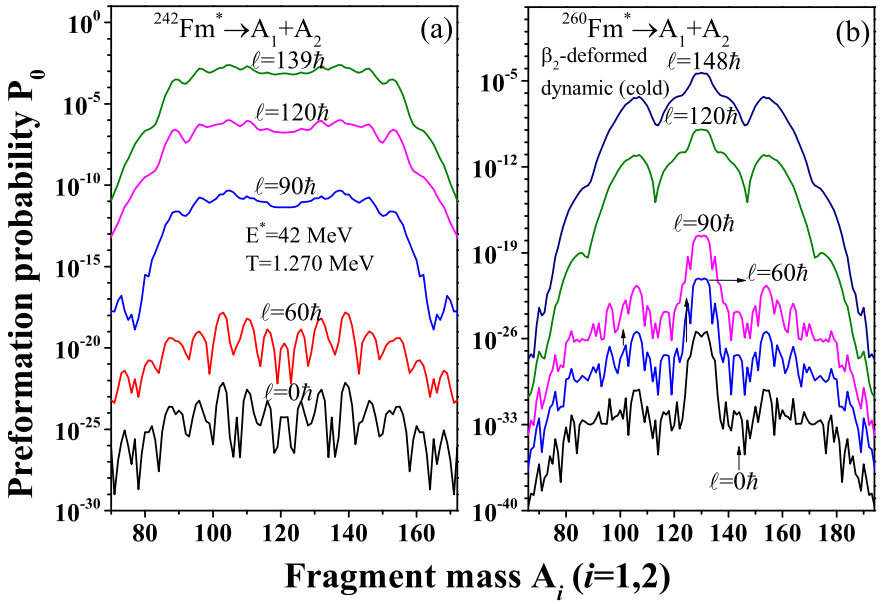

Figure 5.9: Preformation probability (P_0) as a function of fragment mass (A_i) for (a) ^{242}Fm and (b) ^{260}Fm nuclei at angular momentum values ℓ=0-ℓ_{max}.

5.2.2 Induced fission of Fm isotopes

From the results of preceding section, it can't be argued that properties of fission fragments may vary drastically with change in neutron number (N) of parent fissioning nucleus. Further, to analyze the excitation energy (E^*_{CN}) and angular momentum (ℓ) effects on fission fragment mass distributions, the excited state fission decay analysis of Fm isotopes is carried out in present section. Previously, our group has made an investigation on ^{254}Fm nucleus formed in ^{11}B+^{243}Am reaction at various excitation energies using spherical approach, only-β_2 and higher multipole (β_2-β_4) deformations within dynamical cluster-decay model (DCM) [13]. This work represents many interesting results regarding to the effects of deformations, orientations and excitation energies etc. Here, we have chosen ^{11}B-induced reactions on $^{231-249}$Am target forming hot and rotating $^{242-260}$Fm* isotopes to analyze the fission fragment mass distributions for compound nucleus (CN) mass and excitation energies range.

Firstly, the fragmentation potential $V_R(\eta,T)$ and preformation probability P_0 of ^{242}Fm* nucleus forming in ^{11}B+^{231}Am reaction at excitation energy E^*=42 MeV at ℓ=0$\hbar$, are calculated for three kind of approaches as used for the case of spontaneous fission, such as

spherical, β_2-deformed (hot), β_2-deformed (cold) configurations of decay fragments, see Figs. 5.7(a) and 5.7(b). In Figs. 5.7 (a,b), the deformations are considered T-independent i.e. static deformations ($\beta_2(0)$). The calculations are made at ΔR=1.0 fm taken from previous study of ^{254}Fm* at same excitation energy [13]. It is observed from the plot that the fragmentation strcture is significantly modified with inclusion of deformations and orientations. The mass distribution show asymmetric behavior for β_2-deformed (cold) configurations. However, broad symmetric pattern of spherical approach is changed to sharp peak for hot interactions. The reason behind these structural variations of fragmentation potential and preformation probability is same as that for the case of spontaneous fission, as discussed in Sec.3.2.1. Moreover, the results of cold-elongated interactions of decay fragments show nice agreement with the experimental observations [39]. Thereby, further calculations are carried out for the choice of β_2-deformed cold-elongated configurations only.

To see the temperature (T) dependence of deformations see Eq. 2.38) in cold orientations, a comparison of the T-independent (static) and T-dependent (dynamic) β_2-deformations is made in Figs. 5.8(a-b) and 5.8(c-d), respectively, for ^{242}Fm* and ^{260}Fm* excited nuclei at E^*=42 MeV and ℓ=0$\hbar$. It is seen from figure that the dynamic deformations ($\beta_{2i}(T)$ has great influence on fragmentation path and preformation distribution. The static deformations ($\beta_{2i}(0)$ follow asymmetric fission pattern for both fissioning nuclei. In case of dynamic deformations, the ^{242}Fm* nucleus decay via asymmetric fission fragments, however, a symmetric peak appeared in the mass distribution of ^{260}Fm* nucleus. This indicates that dynamic deformations have great influence on the fission fragment mass distributions, and show nice agreement with the experimental observations [39, 40]. Above results have been plotted at zero angular momentum (i.e. V_ℓ=0) only, therefore an effort is made in Fig. 5.9 to investigate the role of rotational energy on the fragment distributions. Figs. 5.9(a-b) show the preformation probability for ^{242}Fm* and ^{260}Fm* nuclei for cold approach using dynamic deformations at broad range of angular momentum i.e. ℓ=0-ℓ_{max}. There are some structural variations in the structure of P_0 for both nuclei. However, the overall mass distribution of fission fragments remains same such as asymmetric for ^{242}Fm* and symmetric for ^{260}Fm* nucleus.

ΔR is the parameter of the model which is used to fit the experimental half-lives and cross-sections. However, in this case we are analyzing the fission fragment mass distributions

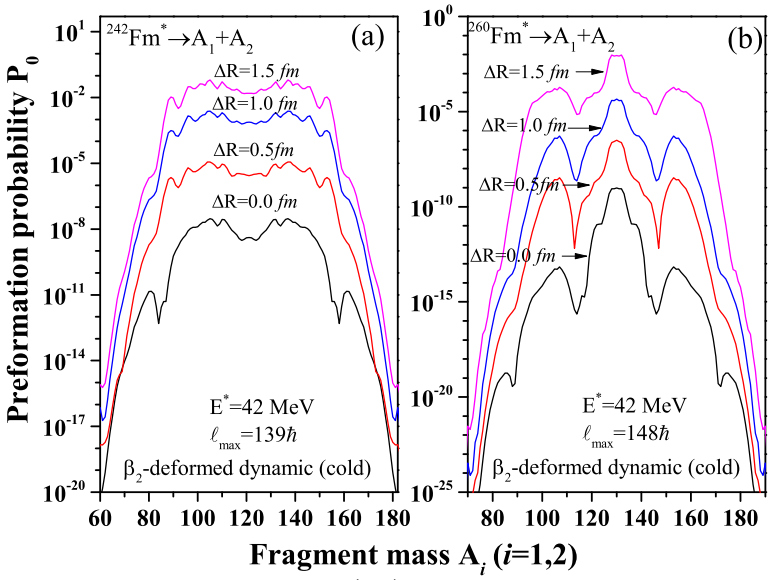

Figure 5.10: Preformation probability $P_0(A_i)$ is presented at a neck-length parameter range of ΔR=0-1.5 fm for (a) ^{242}Fm and (b) ^{260}Fm compound nuclei.

only. To check whether ΔR influence the mass distributions or not, the preformation probability P_0 is plotted in Figs. 5.10(a) and 5.10(b) respectively for ^{242}Fm* and ^{260}Fm* nuclei at E^*=42 MeV for ΔR=0.0 to 1.5 fm. It can be clearly seen from figure that magnitude of P_0 increases with increment in ΔR. However, the fission region structure remains same in general i.e. asymmetric for ^{242}Fm* and symmetric for ^{260}Fm* nucleus. That means ΔR does not effect the fission decay channel of considered fissioning nuclei. Finally, the energy dependence of fission fragment mass distributions of ^{242,250,256,260}Fm* isotopes is studied in Fig. 5.11 at excitation energies E^*=5,10,20 and 42 MeV and corresponding ℓ_{max} values for cold-interactions. It is clearly observed from figure that fission fragment mass distributions are significantly modified with increase in excitation energy and neutron number of compound nuclei. The evolution towards mass asymmetry slows down with increase in excitation energy for ^{242,250,256}Fm*, see Figs. 5.11(a-l). This can be easily understood from the fact that shell effects start diminishing with increase in energy [30]. However, ^{260}Fm* nucleus prefer to decay via symmetric fragments at all energies. If we compare spontaneous fission versus induced fission from Figs. 5.4 and 5.5 for cold interactions, it is observed that for both cases lighter mass Fm nuclei prefer asymmetric fission distribution. For heavier mass Fm nuclei, the triple humped distribution is observed for the case of spontaneous fission showing the equal distribution of symmetric as well as asymmetric fission. However, at excitation energies the symmetric fission is more dominant decay mode in comparison with

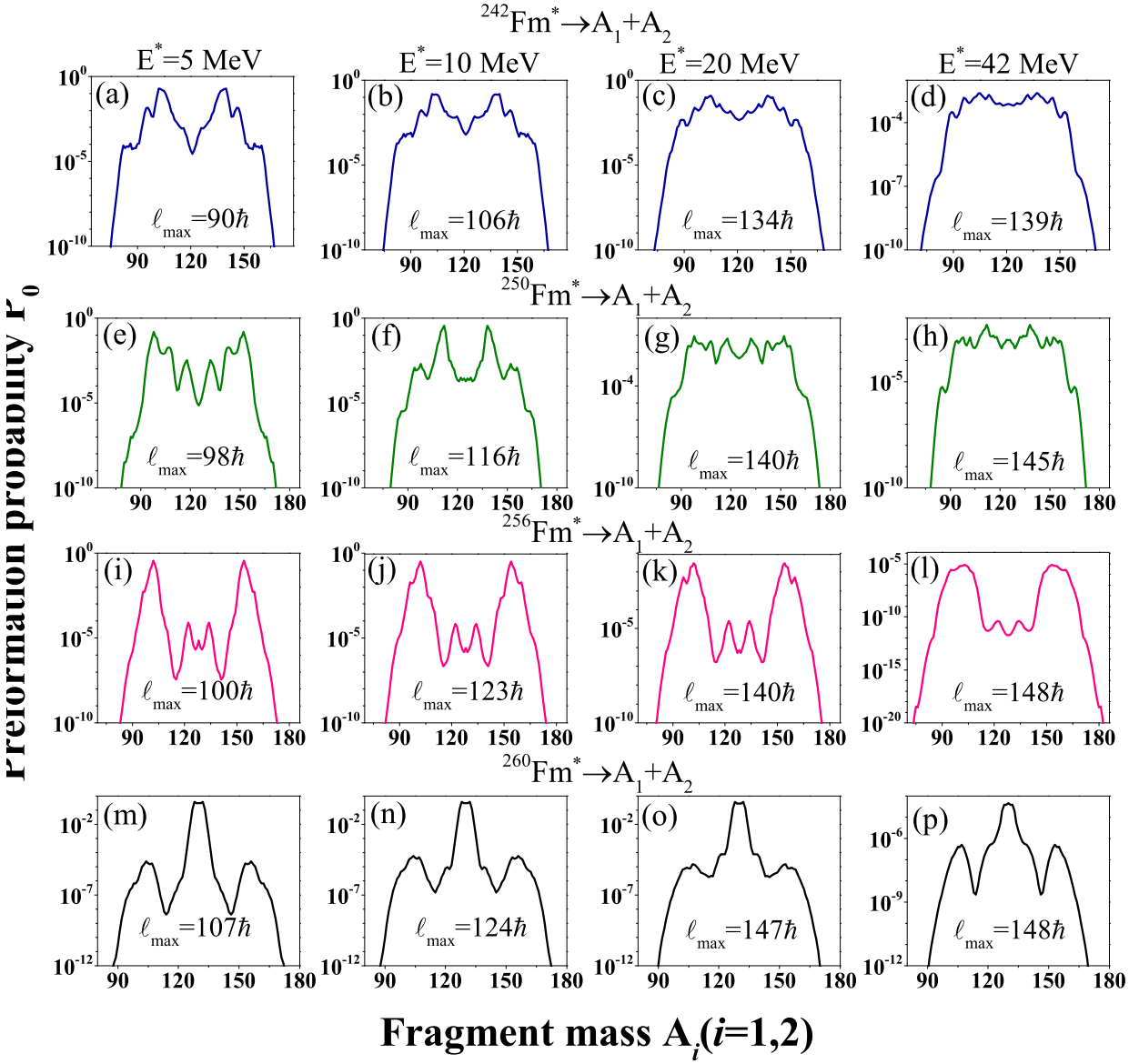

Figure 5.11: Preformation yield $P_0(A_i)$ of ^{242,250,256,260}Fm fissioning nuclei is plotted at excitation energies E^*=5,10,20,42 MeV.

asymmetric fission, as one can see from Figs. 5.11(m-p). These results are in fair agreement with the induced fission measurements of Refs. [39, 40].

5.3 Conclusion

Firstly, the spontaneous fission (SF) of $^{242-260}$Fm isotopes is studied within preformed cluster model (PCM). I have computed the fission fragment mass distributions for three types of decay configurations such as spherical, quadrupole β_2-deformed 'hot-compact' and β_2-deformed 'cold-elongated'. The interaction radius decreases as one go from cold-elongated to spherical to hot-compact shapes, whereas interaction barrier height increases for the same sequence. These results effect the barrier characteristics and hence the fragmentation path, because the potentials involved strongly depend on the deformation and interaction radius of decay fragments. The spherical and β_2-deformed hot-compact configurations depict the symmetric pattern for each fermium isotope, however, the symmetric peaks become sharp with respect to increment in the neutron (N) number of parent nucleus. β_2-deformed cold-elongated shapes of decay fragments show a transition from double humped (asymmetric fission) to triple humped (multi-modal fission) mass distribution. The heavier isotopes such as ^{258,260}Fm exhibit multi-modal fission (i.e. the presence of both symmetric as well as asymmetric fission) for the cold configuration criteria. Spherical and β_2-deformed hot-compact approaches show that Fm isotopes decay via spherical magic shell closure [Sn (Z=50) isotopes]. However, for cold-orientations, Fm nuclei prefer to decay via asymmetric fragments having deformed magic shell closures of Z=38 and N=60,62. This concludes that spherical as well as deformed magic shell closures play important role in the fission dynamics of Fm isotopes. The decay half-lives of the considered spontaneous fissioning nuclei are calculated and in the fair agreement with experimental observed results. This study study highlights the significance of deformation and orientation effects, together with the excitation energy and isotope dependence of fission fragment mass distributions for both spontaneous and induced fission dynamics.

Beside this, the induced fission (IF) of $^{242-260}$Fm* compound nuclei formed in ^{11}B+$^{231-249}$Am reactions at excitation energies E^*=5-42 MeV is analyzed using dynamical cluster-decay model (DCM) which includes the angular momentum (ℓ) and the temperature (T) effects as

discussed in the methodology. We observed that T-dependent (dynamic) deformations play significant role to decide the fission decay mode. Among all three type of considered configurations, the β_2-deformed cold-elongated configurations provide the desired results which are in fair agreement with the experimental findings as we notice in the case of the spontaneous fission. The variation of fragment mass distributions is studied with increase in neutron number and excitation energy. A transformation from asymmetric peak to symmetric peak is observed with increase in neutron number of Fm nucleus. Moreover, the excitation energy of fissioning nuclei significantly effect the fission mass distributions. The angular momentum (ℓ) and neck-length parameter (ΔR) dependence of mass distributions are studied and it is observed that magnitude of preformation yield significantly changes, however, overall fission decay pattern remains same.

After the study of the binary fission, the ternary fission analysis is made using three cluster model(TCM) in the next chapter. The light charge particle accompanied fission is studied and the probable fission fragments are identified.

Bibliography

[1] N. Bohr and J.A. Wheeler, Phys. Rev. **56**, 426 (1939).

[2] U. Brosa, S. Grossmann, and A. Müller, Phys. Rep. **197**, 167 (1990).

[3] A. N. Andreyev *et al.*, Phys. Rev. Lett. **105**, 252502 (2010).

[4] A. N. Andreyev, M. Huyse, and P. Van Duppen, Rev. Mod. Phys. **85**, 1541 (2013).

[5] I. V. Ryzhov *et al.*, Phys. Rev. C **83**, 054603 (2011).

[6] V. Thakur, S. K. Dhiman, Nucl. Phys. A **992**, 121623 (2019).

[7] C. Sharma, A. Jhingan,*et al.*, Phys. Rev. C **107**, 064615 (2023).

[8] A. Sharma, A. Gandhi,and A. Kumar, Phys. Rev. C **106**, L041601 (2022).

[9] J. E. Gindler, K. F. Flynn, L. E. Glendenin, and R. K. Sjoblom, Phys. Rev. C **16**, 1483 (1977).

[10] E. K. Hulet *et al.*, Phys. Rev. C **40**, 770 (1989).

[11] K. Nishio *et al.*, Phys. Rev. C **77**, 064607 (2008).

[12] R. K. Gupta, M Balasubramaniam, R. Kumar, N. Singh, M. Manhas, and W. Greiner, J. Phys. G: Nucl. Part. Phys. **31**, 631 (2005).

[13] M. Kaur, M. K. Sharma, and R. K. Gupta **86**, 064610 (2012).

[14] N. Sharma, A. Kaur, and M. K. Sharma, Phys. Rev. C **102**, 064603 (2020)

[15] K. Sharma, G. Sawhney, and M. K. Sharma, Phys. Rev. C **96**, 054307 (2017).

[16] G. Sawhney, M. K. Sharma, and R. K. Gupta, Phys. Rev. C **83**, 064610 (2011).

[17] K. Sharma, G. Sawhney, M. K. Sharma and R. K. Gupta, Nucl. Phys. A 972, 1 (2018).

[18] A. Kaur and M. K. Sharma, Phys. Rev. C **99**, 044611 (2019)

[19] A. Kaur and M. K. Sharma, Eur. Phys. J. A **55**, 89 (2019).

[20] G. Kaur, K. Sandhu, A. Kaur, and M. K. Sharma, Phys. Rev. C **97**, 054602 (2018)

[21] A. Kaur, G. Kaur, S. K. Patra, and M. K. Sharma, Nucl. Phys. A **990**, 94 (2019).

[22] B. B. Singh, M. K. Sharma, and R. K. Gupta, Phys. Rev. C **77**, 054613 (2008).

[23] A. Kaur, N. Sharma and M. K. Sharma, Phys. Rev. C **103**, 034618 (2021).

[24] H. J. Fink, J. Maruhn, W. Scheid, and W. Greiner, Z. Phys. **268**, 321 (1974).

[25] J. Maruhn and W. Greiner, Phys. Rev. Lett. **32**, 548 (1974).

[26] R. K. Gupta, W. Scheid, and W. Greiner, Phys. Rev. Lett. **35**, 353 (1975).

[27] N. J. Davidson, S. S. Hsiao, J. Markram, H. G. Miller, and Y. Tzeng, Nucl. Phys. A **570**, 61c (1994).

[28] P. A. Seeger, Nucl. Phys. **25**, 1 (1961).

[29] W. Myers and W. J. Swiatecki, Nucl. Phys. **81**, 1 (1966).

[30] A. S. Jensen, J. Damgaard, Nucl. Phys. A **203**, 578 (1973).

[31] V. M. Strutinsky, Nucl. Phys. A **95**, 420 (1967).

[32] R. Kumar and M. K. Sharma, Phys. Rev. C **85**, 054612 (2012).

[33] P. Möller, J. R. Nix, W. D. Myers, and W. J. Swiatecki, At. Data Nucl. Data Tables **59**, 185 (1995).

[34] M. Muenchow and W. Scheid, Phys. Lett. B **162**, 265 (1985); Nucl. Phys. A **468**, 59 (1987).

[35] M. Rashdan, A. Faessler, and W. Waida, J. Phys. G: Nucl. Part. Phys. **17**, 1401 (1991).

[36] H. Kröger and W. Scheid, J. Phys. G: Nucl. Part. Phys. **6**, L85 (1980).

[37] G. Royer and J. Mignen, J. Phys. G: Nucl. Part. Phys. **18**, 1781 (1992).

[38] N. E. Holden and D. C. Hoffman, Pure Appl. Chem. **72**, 1525 (2000).

[39] K. F. Flynn, J. E. Gindler, and L. E. Glendenin, Phys. Rev. C **12**, 1478 (1975).

[40] K. F. Flynn, J. E. Gindler, R. K. Sjoblom, and L. E. Glendenin, Phys. Rev. C **11**, 1676 (1975).

Chapter 6

Light particle accompanied fission

In previous chapters, analysis of different binary decay modes such as α decay, cluster decay, heavy particle radioactivity and the spontaneous fission is made and different properties associated with them are explored. The competing analysis of these decay modes are made using the fragmentation potential, preformation probability and the penetration probability. In the next step, role of the deformations and orientations in the spontaneous fission is explored. After the analysis of the SF mode, this chapter focus on the light charge particle accompanied fission (ternary fission) where the light fragment emission happens in perpendicular direction to the fission axis. The ternary fission fragmentation analysis is carried out using three cluster model (TCM). The most probable decay combinations (of three body decay mode) are obtained using the fragmentation structure. The barrier characteristics of the probable fission channel is studied using different nuclear potentials. A general description of light particle accompanied fission and related aspects is explained in the following section.

6.1 Introduction

The simultaneous emission of the light charge fragment along with two heavy fission fragments is known as light particle accompanied fission (LCP) [1–3]. Mostly, the light fragment emission happen in a direction perpendicular to the fission axis [4]. The light charge particle may be a proton, Triton or a α particle. Due to the higher stability, in light mass domain alpha particle is observed as third fragment in general. The emission of alpha particle along with two fragment in scission state is also known as long range alpha emission (LRA) [5–7,9,15]. Experimentally, the LRA emission is observed mostly in case of the heavy actinides [10–13] and concluded that emission probability increases with increase in the fissility parameter. The dynamical model is given [14]exists, where the LCP formation process

is explored as two random neck ruptures during the time interval about one single-particle period. Using this analysis new semi-classical expressions are given which are further employed to calculate the LCP yields and relative ternary fission probability. It is well known that the heavy actinides go through different binary decay modes (i.e. α decay, cluster decay, spontaneous fission etc) and it is difficult to examine whether the nuclei proceed through binary or ternary splitting. In the experimental observation of LRA in spontaneous fission of ^{252}Cf [15], it was found that the LRA emission and usual binary fission is very similar process. Additionally, the energy ratio distribution for both the processes (binary and ternary) is almost analogous. It will be of interest to make a comparative analysis of the binary and ternary fission process.

In this chapter, the ternary fission analysis of ^{253}Es, nucleus is made using three cluster mode (TCM) and the probable decaying fragments are identified. The three body fragmentation analysis is made using two kind of nuclear potentials i.e. Yukawa plus exponential potential and the Proximity potential. The most probable third fragment is obtained using the fragmentation potential. Keeping this fragment as fixed, comparison of the fragmentation structure is made using two nuclear potentials and the obtained fragments are compared with the binary fission fragments. The penetration probability of the decay channels (three body) are calculated and are used to calculate the relative yield of the fragments. Finally, a comparison of relative yield for the case of the binary and ternary decay is made. The work presented in this chapter is published in the ref [19]

6.2 Calculations and results

6.2.1 Decay of ^{253}Es through ternary fragmentation

In this section, the possibility of ternary decay of ^{253}Es nucleus is investigated, within the three cluster model (TCM) [16, 17]. The ternary fragmentation potential using equation (2.33 of Chapter 2) is calculated for considered radioactive nucleus using the assumption of equatorial configuration [16], and plotted in Fig.6.1 as a function of fragment mass A_2. In this work, the calculations are made at the surface separation s=0.8 fm as the scattering potential V(s_1) corresponding to first turning point s_1 is expected to be higher than the

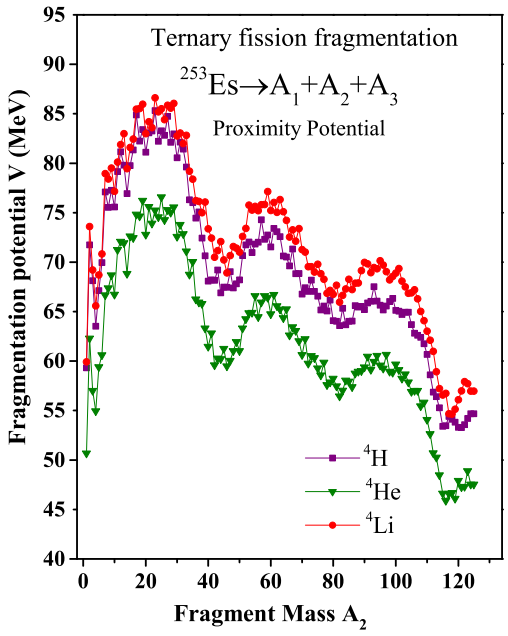

Figure 6.1: Ternary fragmentation potential V(MeV) as a function of fragment mass for ^{253}Es for different A_3=4 combinations.

Q-value of decay fragments in the exit channel. Note that the third fragment mass is fixed i.e. A_3=4, and the possible choices of fragments for mass number four are taken as ^{4}H, ^{4}He and ^{4}Li. As mentioned in Chapter 2 of the thesis, the fragmentation potential is minimized in mass/charge asymmetry coordinate for remaining two binary fragments (A_1+A_2). It may be noted from the figure that the magnitude of the ternary fragmentation potential is lower for A_3=^{4}He (than ^{4}H and ^{4}Li fragments). This indicates that the A_3=^{4}He accompanied ternary fission is more favoured for ^{253}Es nucleus. The preference of ^{4}He fragment as a third fragment for the ternary decay of considered nucleus is in accordance with [18]. Hence, the further investigations are carried out by considering ^{4}He as a third fragment for the ternary fission decay of ^{253}Es nucleus.

Next, to analyze the ternary decay of ^{253}Es, we have considered two nuclear potential, i.e., Yukawa plus exponential and proximity potential as discussed in Chapter 2. In Fig. 6.2, the ternary fragmentation potential is plotted with respect to the fragment mass A_2 for both type of nuclear potentials. Note that results shown in figure 6.2 are calculated at common surface separation s=0.8 fm. It is evident from the figure that the magnitude of fragmentation potential is lower for proximity potential as we compared it to the Yukawa plus exponential potential. That means, the probability of ternary emission seems higher for the choice of the proximity potential. However, the fragmentation structure and the choice

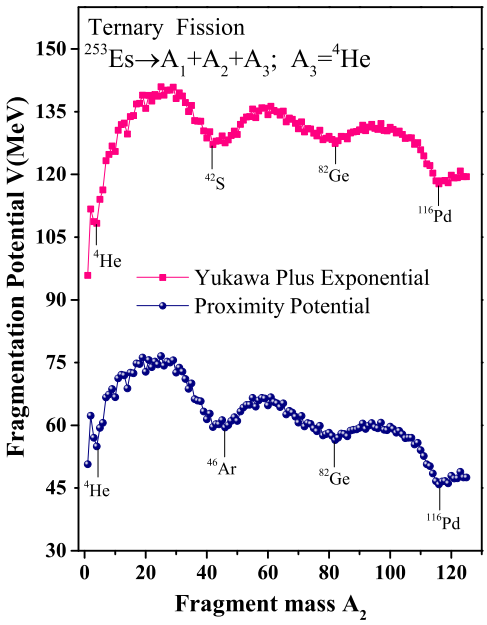

Figure 6.2: Ternary fragmentation potential V(A_2) of ^{253}Es for Yukawa plus exponential and proximity nuclear potentials.

of most probable A_1+A_2 fragment is same for both cases, where the third fragment is fixed (A_3=^{4}He). The minima's of fragmentation path (say, using proximity nuclear potential) of ^{253}Es nucleus, correspond to the following combinations (^{253}Es→A_1+A_2+A_3):

$$(i)^{253}Es \rightarrow {}^4He(Z=2,N=2) + {}^{46}Ar(Z=18,N=28) + {}^{203}Au(Z=79,N=124)$$

$$(ii)^{253}Es \rightarrow {}^4He(Z=2,N=2) + {}^{82}Ge(Z=32,N=50) + {}^{167}Tb(Z=65,N=102)$$

$$(iii)^{253}Es \rightarrow {}^4He(Z=2,N=2) + {}^{116}Pd(Z=46,N=70) + {}^{133}Sb(Z=51,N=82)$$

In case of (i), (ii) and (iii), the emergence of minima's are associated with neutron magicity N=28, 50 and 82 respectively. Where, ^{4}He (doubly magic nucleus) is considered as third fragment in the ternary decay. These results indicate the conclusive role of closed-shell effects in the ternary fission fragmentation of ^{253}Es. It would be of interest, if experimental

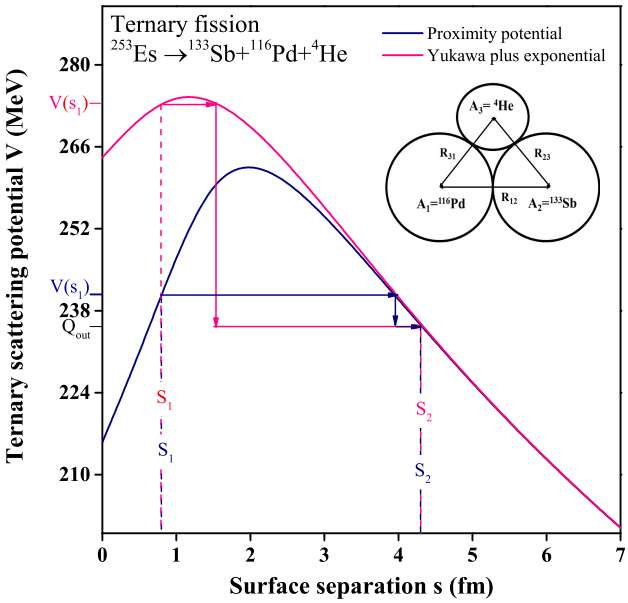

Figure 6.3: The ternary fission scattering potential V (MeV) with respect to the surface separation (s) for ^{253}Es is plotted with the use of Yukawa plus exponential and proximity nuclear potentials.

verification of the obtained results are made available.

After obtaining the most probable decay channel using the fragmentation potential, the barrier characteristics are studied using proximity potential and Yukawa plus exponential potential. The scattering potential is calculated and plotted as a function of the surface separation of the three fragments and shown in Figure 6.3. The position of the barrier and height of the barrier are different for the two cases, and hence the penetration probability gets modified accordingly. The Coulomb barrier is lower for the case of the proximity potential, and one can say that the probability of α emission is higher for that case. The calculated penetration probability is further used to obtain the relative yield of the binary and ternary fission processes discussed in the next section.

6.2.2 Comparative analysis of binary and ternary fission

Finally, a comparative examination of the binary and the ternary fission of ^{253}Es nucleus is made in this section. The relative yields (as per equation (2.36) of chapter.2) of binary and ternary fission fragments are calculated and the results are shown respectively Figs. 6.4(a)

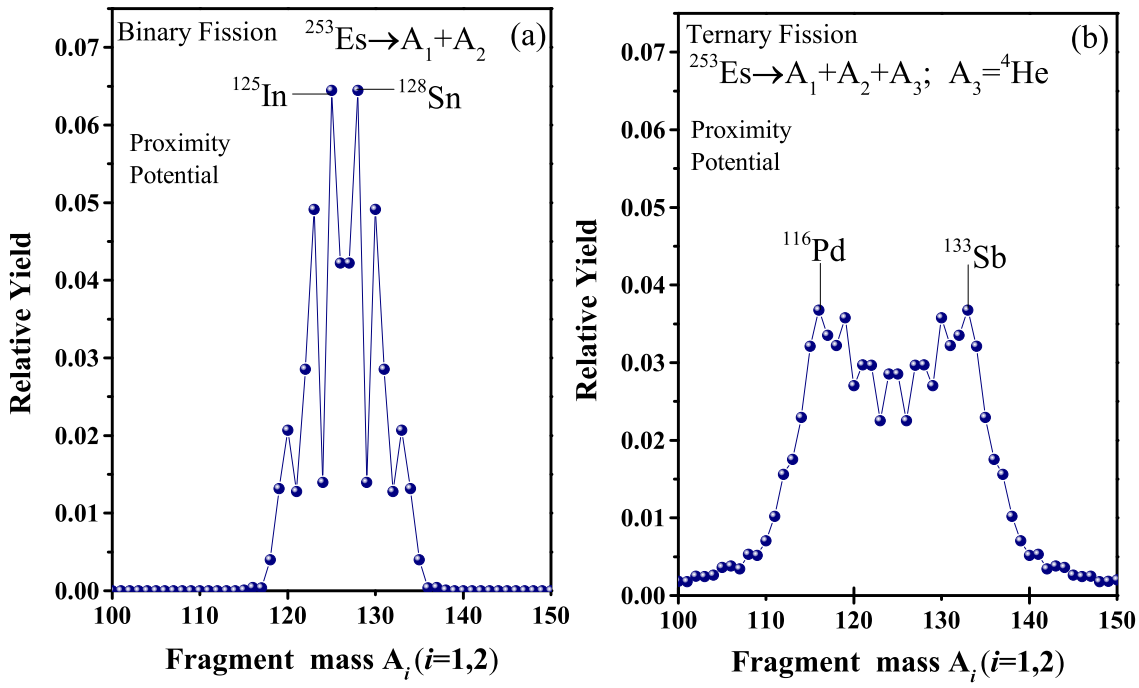

Figure 6.4: The TCM calculated relative yields for (a) binary fission and (b) ternary fission of ^{253}Es. The most probable fission fragment are also marked.

and (b). The scale of x- and y-axis is same in both panels so that one to one comparison for binary and ternary fission mechanisms be carried out. As per Fig. 6.3 and 6.4, the binary and ternary fission decay is more prominent for proximity potential, hence the calculations are done for this choice of potential. The fission fragment mass distribution is significantly different for binary and ternary fission. Ternary fission fragmentation is more asymmetric as compared to binary fission. The choice of most probable fragment as marked in the figure, is also different for the considered fission decay mechanisms. Clearly, the relative yield of symmetric fragments is higher for the case of binary fission decay relative to the ternary fission. This observation also suggests that possibility of binary fission is higher as compared to the ternary fission.

6.3 Conclusion

Summarizing, three cluster model (TCM) is used to study ternary decay process of ^{253}Es nucleus. The calculations are performed using two kinds of attractive nuclear potentials

i.e. Yukawa plus exponential and proximity potential. It is observed that ^{253}Es may also decay via particle-accompanied fission, where third particle is identified as ^{4}He. The most probable fission fragments are identified using the fragmentation structure. The probability of ternary fission seems higher for the choice of the proximity potential. The fragmentation structure and the choice of most probable A_1+A_2 fragments is same for both cases, where the third fragment is fixed (A_3=^{4}He). The barrier characteristics for the most probable decay channel are compared for both of the choices of nuclear potential. There is significant change in the barrier position and barrier height for considered nuclear potentials. The Coulomb barrier is lower for the case of the proximity potential and seems suitable for LCP mode. Further, a comparison of the binary and ternary decay modes is carried out and their mass distribution is compared. The relative yield of symmetric binary fragments is higher than the ternary fission. The most suitable decay channels are picked out for the two and three body splitting modes. Finally, it is observed that magic shell Closure (near Z=50,N=82) play important role for binary as well as ternary fission.

After the analysis of light particle accompanied fission (where a light charge particle is emitted along with two fragments), the comparative analysis of light and heavy third fragment emission processes is made in the next chapter.

Bibliography

[1] K. P. Santosh *et al.*, Eur. Phys. J. A **50**, 66 (2014).

[2] P. Heeg *et al.*, Nucl. Phys. A **409**, 379 (1983).

[3] C. Karthikraj *et al.*,J. Phys. G: Nucl. Part. Phys. **44** 065102 (2017).

[4] Yu. N. Kopatch *et al.*,Phys. Rev. Lett. **82**, 2 (1999).

[5] P. Fong, Phys. Rev. C. **3**, 5 (1971).

[6] Y. Boneh *et al.*, Phys. Rev. C. **156**, 4 (1967).

[7] G. Farwell *et al.*, Phys. Rev. C. **71**, 6 (1947).

[8] Z. Fraenkel *et al.*, Phys. Rev. C. **156**, 4 (1967).

[9] R. L. Watson *et al.*, Phys. Rev. C. **179**, 4 (1969).

[10] O. Cerot and C. Wagemans, Nucl. Phys. A. **641**, 34 (1998).

[11] C. Wagemans and A. J. Deruyetter, Zeitschrift für Physik A Atoms and Nuclei **275**, 149 (1975).

[12] S. Vermote *et al.*, Nucl. Phys. A **806**, 1 (2008).

[13] C. Wagemans *et al.*, Nucl. Phys. A **742**, 291 (2004).

[14] V.A. Rubchenya and S.G. Yavshits, Zeitschrift für Physik A Atoms and Nuclei **329**, 217 (1988).

[15] Z. Fraenkel *et al.*, Phys. Rev. C. **156**, 4 (1967).

[16] K. Manimaran and M. Balasubramaniam, Phys. Rev. C **79**, 024610 (2009).

[17] K. Manimaran and M. Balasubramaniam, Phys. Rev. C **83**, 034609 (2011).

[18] T. R. England and B. F. Rider, Evaluation and Compilation of Fission Product Yields 1993, (No. LA-SUBâ€“94-170), Los Alamos National Lab.

[19] N. Sharma, A. Kaur and M. K. Sharma, Phys. Rev. C **102**, 064603 (2020).

Chapter 7

Role of equatorial and collinear configuration in ternary fission

In previous chapter, the light charge particle accompanied fission is studied using the three cluster model (TCM). The most probable decay channels are identified by calculating the three body fragmentation potential using the equatorial configuration. In the present chapter, a comparative analysis of the equatorial cluster tripartition (ECT) and collinear cluster tripartition (CCT) is made using TCM. The most probable decay channels are identified for ECT and CCT modes using the fragmentation structure and the barrier characteristics are compared. The detailed discussion of the present chapter is given below:

7.1 Introduction

Generally, radioactivity involves the alpha (α), beta (β) and gamma (γ) decay processes. However, there may be a possibility of cluster radioactivity (CR), heavy particle radioactivity (HPR) and spontaneous fission (SF) decay channels depending on the shape, size and inter-nucleon forces of the radioactive element [1–4]. Among the aforementioned decay channels, SF is considered as a powerful tool, that determines the stability of heavy and superheavy nuclei together with related structure aspects. The SF process of actinides is expected to provide further insight of stability and dynamical evolution of the radioactive nuclei [5–7]. Various studies suggest that nuclei belonging to actinide mass region generally exhibit asymmetric fission. However, the experimental analysis of Refs. [8,9] show that the isotopes of Fm exhibit a transition from asymmetric to symmetric fission in region of mass A=256 to 258. In reference to this observation, recently, I have explored [10] the binary fission of $^{242-260}$Fm isotopes by incorporating the deformation and orientation effects in the framework of preformed cluster model (PCM). It was observed that potential energy surfaces and fission fragment mass distributions significantly depend on the mass of fissioning nuclei. In

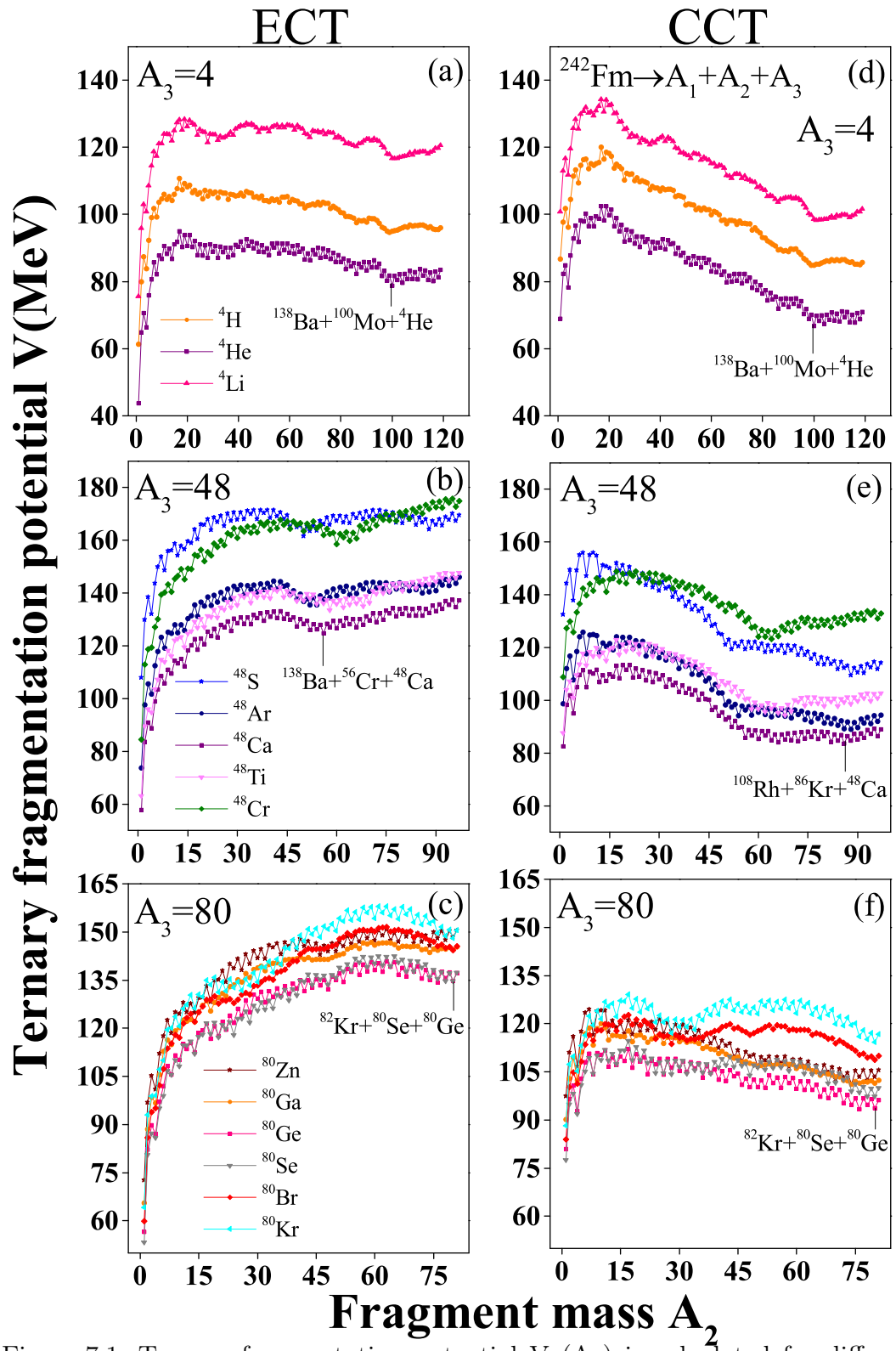

Figure 7.1: Ternary fragmentation potential V (A_2) is calculated for different third fragments with mass number A_3=4, 48, 80 for ^{242}Fm radioactive nucleus using (a-c) ECT and (d-f) CCT emission modes.

continuation of this work, here I intend to explore the ternary fission (TF) of Fm isotopes of extreme masses such as A=242 and 258. Usually, a binary fission mode comprises the emergence of two fragments of comparable masses, but some findings [11–13] give the idea of splitting of a radioactive nucleus into three fragments and the process is termed as TF. It was first observed by Alvarez *et al.* [11] in 1947 where long range alpha particles were observed in company of two fission fragments.

The literature indicate that the actinides and trans-actinidies may decay spontaneously into three partitions. However, mainly through light-particle-accompanied fission (LPF), where the mass of third particle is much smaller than other two fission fragments. The analysis of LPF mostly includes ^{4}He as a third fragment due to its high stability [14–17]. Apart from this, the other nuclei like ^{1,2,3}H, ^{6,8}He, ^{6,7,8,9}Li and ^{9,10}Be are observed in the spontaneous TF [18–20]. Besides LPF, there is also a possibility of true ternary fission (TTF), i.e., the partitioning of nucleus into three fragments of comparable masses [21, 22]. It is to be noted here that spontaneous TTF has not been observed experimentally but some relevant predictions has been made in past. On the other hand, an experimental signature of TTF exists in the induced reactions where isotopes of C, N, O, F, Ne, Na, Mg, S, Al, Si, Ca, Mn and Ni were measured as a heavier third fragment [23–27].

In the ternary fission, a fissioning nucleus may divide into three parts by following equatorial cluster tripartition (ECT) or collinear cluster tripartition (CCT). The process in which third fragment emission happens in a direction perpendicular to the fission axis is termed as equatorial or orthogonal emission. On the other hand, the configuration where the third fragment emits in the direction of fission axis, is known as collinear or polar emission. Previously, some findings concluded that ECT is suited for the light-particle accompanied fission, whereas CCT mode is better for the emission of heavier third fragment [29]. This work is devoted to analyse the ternary fragmentation behaviour of ^{242,258}Fm radioactive nuclei involving wide range of light and heavy mass third fragments by employing ECT and CCT configurations. In view of above discussion, the present chapter is devoted to fulfill the following objectives within the quantum mechanical theory (QMFT) [31–33] based cluster decay models [10, 15, 29, 34, 35]: (i) the selection of third fragment by minimizing all possibilities of

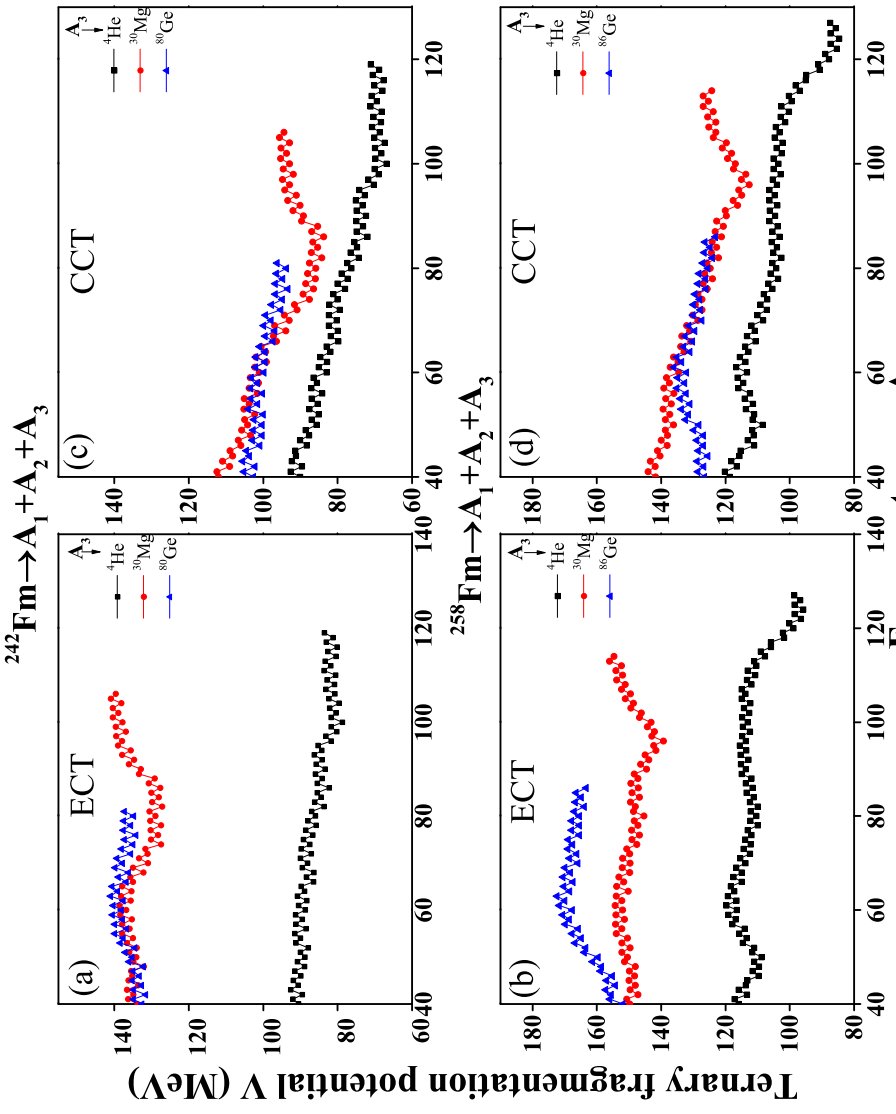

Figure 7.2: Ternary fragmentation potential V(MeV) with respect to the fragment mass A_2 for identified choices of third fragments for (a,c) ^{242}Fm and (b,d) ^{258}Fm nuclei using ECT and CCT configuration modes.

third fragments with respect to their charge numbers for ^{242,258}Fm parent nuclei, (ii) the impact of equatorial and collinear tripartition modes is analyzed by studying the valleys of ternary fragmentation potential and peaks of relative fission yield, (iii) the identification of most probable nascent fission fragments, i.e., A_1+A_2+A_3, and (iv) a relative analysis of binary and ternary fission mass distributions. The overview of the chapter is as follows. The behavior of fragmentation potential and fission yield is studied in section 7.2 using equatorial and collinear configuration. Finally, the summary of the observed results is concluded in section 7.3. The work presented in this chapter is published in the ref [30]

7.2 Calculations and Discussions

First of all, the third fragment (A_3) is selected by minimizing the possible third fragments with respect to their charge (Z) numbers. The TCM-calculated three body fragmentation potential of ^{242}Fm fissioning nucleus for fixed mass numbers of third fragment A_3=4, 48 and 80 is plotted in Figs. 7.1(a-c) and 7.1(d-f) for equatorial cluster tripartition (ECT) and collinear cluster tripartition (CCT) configurations, respectively. These choices are taken to examine the behaviour of fragmentation potential for lighter to heavier mass third fragments. For example, the fragment mass A_3=4 has three possibilities such as ^{4}H, ^{4}He and ^{4}Li, with complementary daughters as ^{238}Es, ^{238}Cf and ^{238}Bk, respectively, whose binary fragmentation (A_1+A_2) is properly minimized in charge or mass asymmetry (η_Z) coordinate. Using these choices, the ternary fragmentation potential is calculated for ^{242}Fm nucleus, see Fig. 7.1(a) and 7.1(d), and the lowest among these three is the most favourable A_3 fragment, i.e. ^{4}He for both ECT and CCT choices. We have 12 possible choices of charge number for both A_3 = 48 and 80 fragments such as (Z = 16 to 27) and (Z=29 to 40), However, the ternary fragmentation potential is represented for the limited cases just for the sake of clarity . It is noticed from figure that ^{4}He, ^{48}Ca and ^{80}Ge are the most preferred choices among their competing fragments due to the lower fragmentation potential, independent of the choice of cluster tripartition configurations. Moreover, the magnitude and the fragmentation structure is drastically modified when one shifts from ECT to CCT configuration. Similar analysis is carried out for ^{258}Fm nucleus, but not shown here to avoid repetition, and it is observed that ^{4}He, ^{48}Ca and ^{86}Se are the most favorable choices for third fragment.

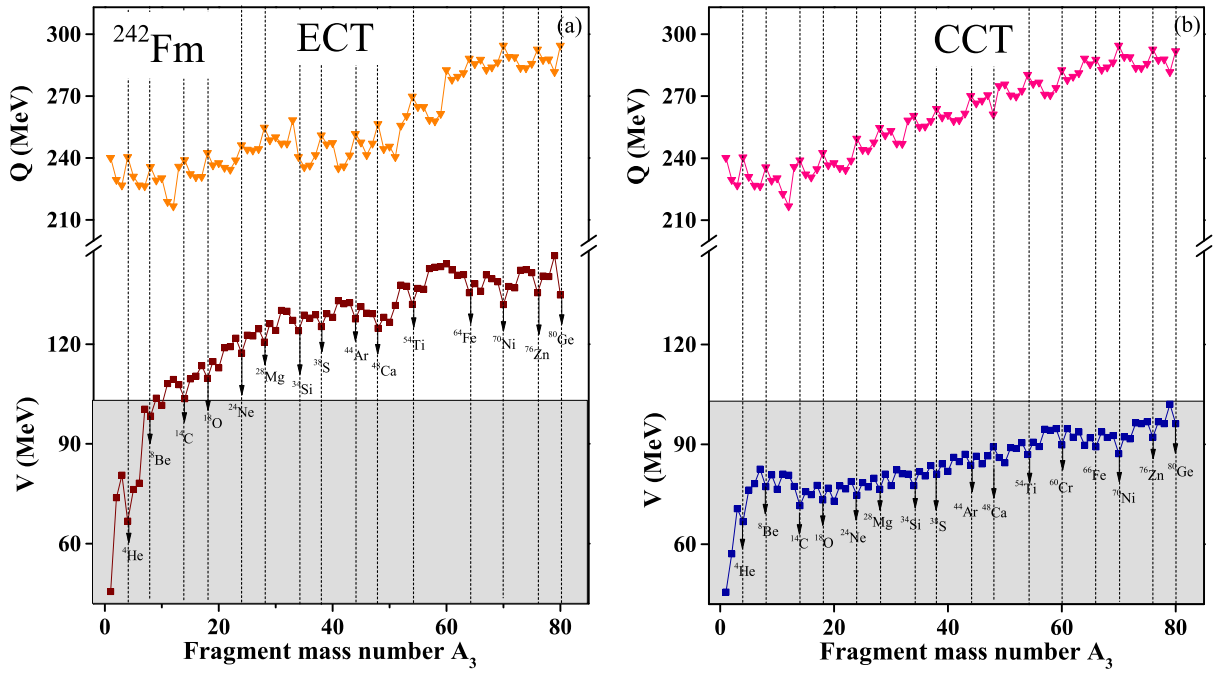

Figure 7.3: The ternary fragmentation potential with respect to the third fragment mass A_3 for ^{242}Fm using (a) equatorial and (b) collinear configuration mode.

Table 7.1: The most preferred ternary fission fragment combination (A_1+A_2) along with fixed third fragment (A_3) for ECT and CCT configuration of ^{258}Fm parent nucleus. The corresponding proton (Z) and neutron (N) number are also listed.

ECT		CCT	
Fragment combination	$(N_1,Z_1)+(N_2,Z_2)+(N_3,Z_3)$	Fragment combination	$(N_1,Z_1)+(N_2,Z_2)+(N_3,Z_3)$
^{96}Zr+^{86}Kr +^{60}Cr	(56,40)+(**50**,36)+(36,24)		
^{91}Sr+^{90}Sr +^{61}Cr	(53,38)+(52,38)+(37,24)		
^{90}Sr+^{90}Sr +^{62}Cr	(52,38)+(52,38)+(38,24)		
^{90}Sr+^{90}Sr +^{63}Mn	(52,38)+(52,38)+(39,24)		
^{90}Sr+^{88}Kr +^{64}Fe	(52,38)+(**50**,38)+(38,24)		
^{91}Sr+^{86}Kr +^{65}Fe	(53,38)+(**50**,36)+(39,26)		
^{91}Sr+^{86}Kr +^{65}Fe	(53,38)+(**50**,36)+(39,26)		
^{90}Sr+^{86}Kr +^{66}Fe	(52,38)+(**50**,36)+(40,26)		
^{89}Sr+^{86}Kr +^{67}Fe	(51,38)+(**50**,36)+(41,26)		
^{88}Sr+^{86}Kr +^{68}Fe	(**50**,38)+(**50**,36)+(42,26)		
^{87}Rb+^{86}Kr +^{69}Co	(**50**,37)+(**50**,36)+(42,27)		
^{86}Kr+^{86}Kr +^{70}Ni	(**50**,36)+(**50**,36)+(42,**28**)		
^{85}Kr+^{86}Kr +^{71}Ni	(49,36)+(**50**,36)+(43,**28**)		
^{88}Sr+^{82}Se +^{72}Ni	(**50**,38)+(48,34)+(44,**28**)		
^{88}Sr+^{82}Se +^{72}Ni	(**50**,38)+(48,34)+(44,**28**)		
^{88}Sr+^{81}Se +^{73}Ni	(**50**,38)+(47,34)+(45,**28**)		
^{88}Sr+^{80}Se +^{74}Ni	(**50**,38)+(46,34)+(46,**28**)		
^{87}Rb+^{80}Se +^{75}Cu	(**50**,37)+(46,34)+(46,29)		
^{86}Kr+^{80}Se +^{76}Zn	(**50**,36)+(46,34)+(46,30)		
^{85}Kr+^{80}Se +^{77}Zn	(49,36)+(46,34)+(47,30)		
^{84}Kr+^{80}Se +^{78}Zn	(48,36)+(46,34)+(48,30)		
^{83}Kr+^{80}Se +^{79}Zn	(47,36)+(46,34)+(49,30)		
^{82}Kr+^{80}Se +^{80}Ge	(48,34)+(46,34)+(48,32)		
^{129}Sn +^{128}Sn +^{1}n	(79,**50**)+(78,**50**)+(1,0)		
^{130}Sn +^{126}In +^{2}H	(80,**50**)+(77,49)+(1,1)		
^{130}Sn +^{125}In +^{3}H	(80,**50**)+(76,49)+(**2**,1)		

ECT		CCT	
Fragment combination	$(N_1,Z_1)+(N_2,Z_2)+(N_3,Z_3)$	Fragment combination	$(N_1,Z_1)+(N_2,Z_2)+(N_3,Z_3)$
^{130}Sn +^{124}In +^{4}He	(80,**50**)+(76,48)+(**2**,**2**)		
^{131}Sn +^{122}Cd +^{5}He	(81,**50**)+(74,48)+(3,**2**)		
^{130}Sn +^{122}Cd +^{6}He	(80,**50**)+(74,48)+(4,**2**)		
^{132}Sn +^{119}Ag +^{7}Li	(**82**,**50**)+(72,47)+(4,3)		
^{132}Sn +^{118}Pd +^{8}Be	(**82**,**50**)+(72,46)+(4,4)		
^{131}Sn +^{118}Pd +^{9}Be	(81,**50**)+(72,46)+(5,4)		
^{132}Sn +^{116}Pd +^{10}Be	(**82**,**50**)+(70,46)+(6,4)		
^{131}Sn +^{116}Pd +^{11}Be	(81,**50**)+(70,46)+(7,4)		
^{130}Sn +^{116}Pd +^{12}Be	(80,**50**)+(70,46)+(**8**,4)		
^{132}Sn +^{113}Ru +^{13}C	(**82**,**50**)+(72,44)+(7,6)		
^{132}Sn +^{112}Ru +^{14}C	(**82**,**50**)+(72,44)+(**8**,6)		
^{131}Sn +^{112}Ru +^{15}C	(81,**50**)+(68,44)+(9,6)		
^{134}Te +^{108}Mo +^{16}C	(**82**,52)+(66,42)+(10,6)		
^{133}Sb+^{108}Mo +^{17}N	(**82**,51)+(66,42)+(10,7)		
^{132}Sn+^{108}Mo +^{18}O	(**82**,**50**)+(66,42)+(10,**8**)		
^{132}Sn+^{107}Mo +^{19}O	(**82**,**50**)+(65,42)+(11,**8**)		
^{132}Sn+^{106}Mo +^{20}O	(**82**,**50**)+(64,42)+(12,**8**)		
^{134}Te+^{103}Zr +^{21}O	(**82**,52)+(63,40)+(13,**8**)	^{131}Sn+^{106}Mo +^{21}O	(81,**50**)+(64,42)+(13,**8**)
^{134}Te+^{102}Zr +^{22}O	(**82**,52)+(62,40)+(14,**8**)		
^{133}Sb+^{102}Zr +^{23}F	(**82**,51)+(62,40)+(14,9)		
^{132}Sn+^{102}Zr +^{24}Ne	(**82**,**50**)+(62,40)+(14,10)		
^{132}Sn+^{101}Zr +^{25}Ne	(**82**,**50**)+(61,40)+(15,10)		
^{132}Sn+^{100}Zr +^{26}Ne	(**82**,**50**)+(60,40)+(16,10)		
^{133}Sn+^{98}Sr +^{27}Na	(**82**,**50**)+(60,38)+(16,11)	^{132}Sn+^{99}Y +^{27}Na	(**82**,**50**)+(60,39)+(16,11)
^{132}Sn+^{98}Sr +^{28}Mg	(**82**,**50**)+(60,38)+(16,12)		
^{132}Sn+^{97}Sr +^{29}Mg	(**82**,**50**)+(59,38)+(17,12)		
^{132}Sn+^{96}Sr +^{30}Mg	(**82**,**50**)+(58,38)+(18,12)		
^{131}Sn+^{96}Sr +^{31}Mg	(81,**50**)+(58,38)+(19,12)		
^{134}Te+^{92}Kr +^{32}Mg	(**82**,52)+(56,36)+(**20**,12)	^{132}Sn+^{94}Sr +^{32}Mg	(**82**,**50**)+(56,38)+(**20**,12)
^{132}Sn+^{93}Kr +^{33}Si	(**82**,**50**)+(57,36)+(19,14)		
^{132}Sn+^{92}Kr +^{34}Si	(**82**,**50**)+(56,36)+(**20**,14)		

ECT		CCT	
Fragment combination	$(N_1,Z_1)+(N_2,Z_2)+(N_3,Z_3)$	Fragment combination	$(N_1,Z_1)+(N_2,Z_2)+(N_3,Z_3)$
^{132}Sn+^{91}Kr +^{35}Si	(**82**,**50**)+(55,36)+(21,14)		
^{134}Te+^{88}Se +^{36}Si	(**82**,52)+(54,34)+(22,14)	^{132}Sn+^{90}Kr +^{36}Si	(**82**,**50**)+(54,36)+(22,14)
^{133}Sb+^{88}Se +^{37}P	(**82**,51)+(54,34)+(22,15)	^{132}Sn+^{89}Br +^{37}P	(**82**,**50**)+(54,35)+(22,15)
^{132}Sn+^{88}Se +^{38}S	(**82**,**50**)+(54,34)+(22,16)		
^{132}Sn+^{87}Se +^{39}S	(**82**,**50**)+(53,34)+(23,16)		
^{132}Sn+^{86}Se +^{40}S	(**82**,**50**)+(52,34)+(24,16)		
^{134}Te+^{83}Ge +^{41}S	(**82**,52)+(51,32)+(25,16)	^{132}Sn+^{85}Se +^{41}S	(**82**,**50**)+(51,34)+(25,16)
^{134}Te+^{82}Ge +^{42}S	(**82**,52)+(**50**,32)+(26,16)	^{132}Sn+^{84}Se +^{42}S	(**82**,**50**)+(**50**,34)+(26,16)
^{133}Sb+^{82}Ge +^{43}Cl	(**82**,51)+(**50**,32)+(26,17)	^{132}Sn+^{83}As +^{43}Cl	(**82**,**50**)+(**50**,33)+(26,17)
^{132}Sn+^{82}Ge +^{44}Ar	(**82**,**50**)+(**50**,32)+(26,18)		
^{131}Sn+^{82}Ge +^{45}Ar	(81,**50**)+(**50**,32)+(27,18)		
^{134}Te+^{78}Zn +^{46}Ar	(**82**,52)+(48,30)+(**28**,18)	^{132}Sn+^{78}Zn +^{46}Ar	(**82**,**50**)+(48,30)+(**28**,18)
^{133}Sb+^{78}Zn +^{47}K	(**82**,51)+(48,30)+(**28**,19)	^{132}Sn+^{79}Ga +^{47}K	(**82**,**50**)+(57,32)+(**28**,19)
^{132}Sn+^{78}Zn +^{48}Ca	(**82**,**50**)+(48,30)+(**28**,**20**)		
^{131}Sn+^{78}Zn +^{49}Ca	(81,**50**)+(48,30)+(29,**20**)		
^{132}Sn+^{76}Zn +^{50}Ca	(**82**,**50**)+(46,30)+(30,**20**)		
^{131}Sn+^{76}Zn +^{51}Ca	(81,**50**)+(46,30)+(31,**20**)		
^{134}Te+^{72}Ni +^{52}Ca	(**82**,52)+(44,**28**)+(32,**20**)	^{130}Sn+^{76}Zn +^{52}Ca	(80,**50**)+(46,30)+(32,**20**)
^{133}Sb+^{72}Ni +^{53}Sc	(**82**,51)+(44,**28**)+(32,21)	^{132}Sn+^{73}Cu +^{53}Sc	(**82**,**50**)+(44,29)+(32,21)
^{132}Sn+^{72}Ni +^{54}Ti	(**82**,**50**)+(44,**28**)+(32,22)		
^{131}Sn+^{72}Ni +^{55}Ti	(81,**50**)+(44,**28**)+(33,22)		
^{132}Sn+^{70}Ni +^{56}Ti	(**82**,**50**)+(42,**28**)+(34,22)		
^{131}Sn+^{70}Ni +^{57}Ti	(81,**50**)+(42,**28**)+(35,22)		
^{130}Sn+^{70}Ni +^{58}Ti	(80,**50**)+(42,**28**)+(36,22)		
^{133}Sb+^{66}Fe +^{59}V	(**82**,51)+(40,26)+(36,23)	^{132}Sn+^{67}Co +^{59}V	(**82**,**50**)+(40,27)+(36,23)
^{132}Sn+^{66}Fe +^{60}Cr	(**82**,**50**)+(40,26)+(36,24)		
^{131}Sn+^{66}Fe +^{61}Cr	(81,**50**)+(40,26)+(37,24)		
^{130}Sn+^{66}Fe +^{62}Cr	(80,**50**)+(40,26)+(38,24)	^{132}Sn+^{64}Fe +^{62}Cr	(**82**,**50**)+(38,26)+(38,24)

ECT		CCT	
Fragment combination	$(N_1,Z_1)+(N_2,Z_2)+(N_3,Z_3)$	Fragment combination	$(N_1,Z_1)+(N_2,Z_2)+(N_3,Z_3)$
^{132}Sn+^{63}Mn +^{63}Mn	(**82**,**50**)+(38,25)+(38,25)		
^{132}Cd+^{66}Fe +^{64}Fe	(84,48)+(40,26)+(38,26)		
^{127}Cd+^{66}Fe +^{65}Fe	(79,48)+(40,26)+(39,26)		
^{126}Cd+^{66}Fe +^{66}Fe	(78,48)+(40,26)+(40,26)		
^{124}Cd+^{67}Fe +^{67}Fe	(76,48)+(41,26)+(41,26)	^{109}Mo+^{82}Ge +^{67}Fe	(67,42)+(**50**,32)+(41,26)
^{122}Cd+^{68}Fe +^{68}Fe	(74,48)+(42,26)+(42,26)	^{108}Mo+^{82}Ge +^{68}Fe	(66,42)+(**50**,32+(42,26)
^{108}Mo+^{81}Ga +^{69}Co	(66,42)+(49,32)+(42,27)	^{107}Nb+^{82}Ga +^{69}Co	(66,41)+(**50**,32)+(42,27)
^{110}Mo+^{78}Zn +^{70}Ni	(58,42)+(48,30)+(42,**28**)	^{106}Zr+^{82}Ge +^{70}Ni	(66,40)+(**50**,32)+(42,**28**)
^{109}Mo+^{78}Zn +^{71}Ni	(57,42)+(48,30)+(43,**28**)	^{105}Zr+^{82}Ge +^{71}Ni	(65,40)+(**50**,32)+(43,**28**)
^{104}Zr+^{82}Ge +^{72}Ni	(64,40)+(**50**,32)+(44,**28**)		
^{103}Zr+^{82}Ge +^{73}Ni	(63,40)+(**50**,32)+(45,**28**)		
^{102}Zr+^{82}Ge +^{74}Ni	(62,40)+(**50**,32)+(46,**28**)		
^{102}Zr+^{81}Ga +^{75}Cu	(62,40)+(**50**,31)+(46,29)	^{101}Y+^{82}Ge +^{75}Cu	(62,39)+(**50**,32)+(46,29)
^{102}Zr+^{80}Zn +^{76}Zn	(62,40)+(**50**,30)+(46,30)		
^{103}Zr+^{78}Zn +^{77}Zn	(63,40)+(48,30)+(47,30)	^{99}Sr+^{82}Ge +^{77}Zn	(61,38)+(**50**,32)+(47,30)
^{102}Zr+^{78}Zn +^{78}Zn	(62,40)+(48,30)+(48,30)	^{98}Sr+^{82}Ge +^{78}Zn	(60,38)+(**50**,32)+(48,30)
^{97}Sr+^{82}Ge +^{79}Zn	(59,38)+(**50**,32)+(49,30)		
^{98}Sr+^{82}Zn +^{80}Ge	(60,38)+(52,30)+(48,32)	^{96}Kr+^{82}Ge +^{80}Ge	(60,36)+(**50**,32)+(48,32)
^{95}Kr+^{82}Ge +^{81}Ge	(59,36)+(**50**,32)+(49,32)		
^{94}Kr+^{82}Ge +^{82}Ge	(58,36)+(**50**,32)+(**50**,32)		
^{92}Kr+^{83}Ge +^{83}Ge	(56,36)+(51,32)+(51,32)		
^{88}Se+^{86}Se +^{84}Ge	(54,34)+(52,34)+(52,32)		
^{87}Se+^{86}Ge +^{85}Se	(53,34)+(54,32)+(51,34)		
^{86}Se+^{86}Ge +^{86}Se	(52,34)+(54,32)+(52,34)		
^{132}Sn+^{78}Zn +^{48}Ca	(**82**,**50**)+(48,30)+(**28**,**20**)		
^{131}Sn+^{78}Zn +^{49}Ca	(81,**50**)+(48,30)+(29,**20**)		
^{132}Sn+^{76}Zn +^{50}Ca	(**82**,**50**)+(46,30)+(30,**20**)		
^{131}Sn+^{76}Zn +^{51}Ca	(81,**50**)+(46,30)+(31,**20**)		
^{134}Te+^{72}Ni +^{52}Ca	(**82**,52)+(44,**28**)+(32,**20**)	^{130}Sn+^{76}Zn +^{52}Ca	(80,**50**)+(46,30)+(32,**20**)
^{133}Sb+^{72}Ni +^{53}Sc	(**82**,51)+(44,**28**)+(32,21)	^{132}Sn+^{73}Cu +^{53}Sc	(**82**,**50**)+(44,29)+(32,21)
^{132}Sn+^{72}Ni +^{54}Ti	(**82**,**50**)+(44,**28**)+(32,22)		

ECT		CCT	
Fragment combination	$(N_1,Z_1)+(N_2,Z_2)+(N_3,Z_3)$	Fragment combination	$(N_1,Z_1)+(N_2,Z_2)+(N_3,Z_3)$
^{131}Sn+^{72}Ni +^{55}Ti	(81,**50**)+(44,**28**)+(33,22)		
^{132}Sn+^{70}Ni +^{56}Ti	(**82**,**50**)+(42,**28**)+(34,22)		
^{131}Sn+^{70}Ni +^{57}Ti	(81,**50**)+(42,**28**)+(35,22)		
^{130}Sn+^{70}Ni +^{58}Ti	(80,**50**)+(42,**28**)+(36,22)		
^{133}Sb+^{66}Fe +^{59}V	(**82**,51)+(40,26)+(36,23)	^{132}Sn+^{67}Co +^{59}V	(**82**,**50**)+(40,27)+(36,23)
^{132}Sn+^{66}Fe +^{60}Cr	(**82**,**50**)+(40,26)+(36,24)		
^{131}Sn+^{66}Fe +^{61}Cr	(81,**50**)+(40,26)+(37,24)		
^{130}Sn+^{66}Fe +^{62}Cr	(80,**50**)+(40,26)+(38,24)	^{132}Sn+^{64}Fe +^{62}Cr	(**82**,**50**)+(38,26)+(38,24)
^{132}Sn+^{63}Mn +^{63}Mn	(**82**,**50**)+(38,25)+(38,25)		
^{132}Cd+^{66}Fe +^{64}Fe	(84,48)+(40,26)+(38,26)		
^{127}Cd+^{66}Fe +^{65}Fe	(79,48)+(40,26)+(39,26)		
^{126}Cd+^{66}Fe +^{66}Fe	(78,48)+(40,26)+(40,26)		
^{124}Cd+^{67}Fe +^{67}Fe	(76,48)+(41,26)+(41,26)	^{109}Mo+^{82}Ge +^{67}Fe	(67,42)+(**50**,32)+(41,26)
^{122}Cd+^{68}Fe +^{68}Fe	(74,48)+(42,26)+(42,26)	^{108}Mo+^{82}Ge +^{68}Fe	(66,42)+(**50**,32+(42,26)
^{108}Mo+^{81}Ga +^{69}Co	(66,42)+(49,32)+(42,27)	^{107}Nb+^{82}Ga +^{69}Co	(66,41)+(**50**,32)+(42,27)
^{110}Mo+^{78}Zn +^{70}Ni	(58,42)+(48,30)+(42,**28**)	^{106}Zr+^{82}Ge +^{70}Ni	(66,40)+(**50**,32)+(42,**28**)
^{109}Mo+^{78}Zn +^{71}Ni	(57,42)+(48,30)+(43,**28**)	^{105}Zr+^{82}Ge +^{71}Ni	(65,40)+(**50**,32)+(43,**28**)
^{104}Zr+^{82}Ge +^{72}Ni	(64,40)+(**50**,32)+(44,**28**)		
^{103}Zr+^{82}Ge +^{73}Ni	(63,40)+(**50**,32)+(45,**28**)		
^{102}Zr+^{82}Ge +^{74}Ni	(62,40)+(**50**,32)+(46,**28**)		
^{102}Zr+^{81}Ga +^{75}Cu	(62,40)+(**50**,31)+(46,29)	^{101}Y+^{82}Ge +^{75}Cu	(62,39)+(**50**,32)+(46,29)
^{102}Zr+^{80}Zn +^{76}Zn	(62,40)+(**50**,30)+(46,30)		
^{103}Zr+^{78}Zn +^{77}Zn	(63,40)+(48,30)+(47,30)	^{99}Sr+^{82}Ge +^{77}Zn	(61,38)+(**50**,32)+(47,30)
^{102}Zr+^{78}Zn +^{78}Zn	(62,40)+(48,30)+(48,30)	^{98}Sr+^{82}Ge +^{78}Zn	(60,38)+(**50**,32)+(48,30)
^{97}Sr+^{82}Ge +^{79}Zn	(59,38)+(**50**,32)+(49,30)		
^{98}Sr+^{82}Zn +^{80}Ge	(60,38)+(52,30)+(48,32)	^{96}Kr+^{82}Ge +^{80}Ge	(60,36)+(**50**,32)+(48,32)
^{95}Kr+^{82}Ge +^{81}Ge	(59,36)+(**50**,32)+(49,32)		
^{94}Kr+^{82}Ge +^{82}Ge	(58,36)+(**50**,32)+(**50**,32)		
^{92}Kr+^{83}Ge +^{83}Ge	(56,36)+(51,32)+(51,32)		
^{88}Se+^{86}Se +^{84}Ge	(54,34)+(52,34)+(52,32)		
^{87}Se+^{86}Ge +^{85}Se	(53,34)+(54,32)+(51,34)		
^{86}Se+^{86}Ge +^{86}Se	(52,34)+(54,32)+(52,34)		

Further, the deepest minima in the fission region of the ternary fragmentation potential of the most favorable A_3 fragment are also marked with vertical line in Figs.7.1(a-f) for all considered cases. Interestingly, the choice of third fragment A_3 remains same and it is independent of the type of the cluster tripartition, however, the most preferred A_1+A_2 fragments can be different for ECT/CCT approaches.

Note that the deep valley of the fragmentation potential gives the most probable fission fragment combination as they are more stable than the neighbouring decay fragments. It is observed that such kind of minima in the fragmentation structure is mainly due to the influence of shell closure effects of the fragment combination. As a consequence, lowest magnitude of fragmentation potential is observed for those fragments which have either magic proton/neutron numbers or lying nearby the magic shell closures. Therefore, magic nuclide is observed as one or two of the decay fragments. From Fig.7.1, the identified most probable fission fragment combinations (A_1+A_2+A_3) for ECT mode are ^{138}Ba(Z=56,N=**82**)+^{100}Mo(N=58,Z=42)+^{4}He(Z=**2**,N=**2**), ^{138}Ba(Z=56,N=**82**)+^{56}Cr(Z=24, N=32)+^{48}Ca(Z=**20**,N=**28**), ^{82}Kr(Z=34,N=48)+^{80}Se(Z=34,N=46)+^{80}Ge(Z=32,N=48), and for CCT partition the fragment combination is same for A_3=^{4}He and ^{80}Ge but different for A_3=^{48}Ca as: ^{108}Ru(Z=44,N=64)+^{86}Kr(Z=36,N=**50**)+^{48}Ca(Z=**20**,N=**28**). This may happen because of the contribution of Coulomb potential, which reduces in the CCT configuration due to the large interfragment distance between A_1 and A_2 (see Fig. 2.3 (b) of chapter 2), and this impact is more for the for the heavier A_3 fragment.

Following the same procedure, the most preferred choices for third fragment from mass A_3=1 to $A_P/3$ are identified and listed in tables I and II for ^{242}Fm and ^{258}Fm parent nuclei, respectively. Here, A_P is the mass of parent nucleus. The fragment combinations (A_1+A_2+A_3) having the lowest value in the ternary fission region are also shown in the tables. Note that, a condition of $A_1 \geq A_2 \geq A_3$ is imposed in the calculations to avoid the repetition of fragment combination. It is observed that the choice of third fragment A_3 remains same and it is independent of the choice of tripartition, and in accordance with the results of Fig.7.1. However, the most preferred A_1+A_2 fragments get changed for many cases as listed tables I and II. The proton and neutron numbers are also mentioned along with the fragment combination. The proton (Z=2, 8, 20, 28, 50) and neutron (N=2, 8, 20, 28, 50, 82) shell closures of all fragments are marked with the bold letters.

Table 7.2: The most preferred ternary fission fragment combination (A_1+A_2) along with fixed third fragment (A_3) for ECT and CCT configuration of ^{242}Fm parent nucleus. The corresponding proton (Z) and neutron (N) number are also listed.

ECT		CCT	
Fragment combination	$(N_1,Z_1)+(N_2,Z_2)+(N_3,Z_3)$	Fragment combination	$(N_1,Z_1)+(N_2,Z_2)+(N_3,Z_3)$
^{121}Sn +^{120}Sn +^{1}n	(71,**50**)+(70,**50**)+(1,0)		
^{138}Ba +^{104}Tc +^{2}H	(**82**,56)+(61,43)+(1,1)		
^{139}La +^{100}Mo +^{3}H	(**82**,57)+(58,42)+(**2**,1)		
^{138}Ba +^{100}Mo +^{4}He	(**82**,56)+(58,42)+(**2**,**2**)		
^{138}Ba +^{99}Mo +^{5}He	(**82**,56)+(57,42)+(3,**2**)		
^{138}Ba +^{98}Mo +^{6}He	(**82**,56)+(56,42)+(4,**2**)		
^{138}Ba +^{97}Nb +^{7}Li	(**82**,56)+(56,41)+(4,3)		
^{138}Ba +^{96}Zr +^{8}Be	(**82**,56)+(56,40)+(4,4)		
^{138}Ba +^{95}Zr +^{9}Be	(**82**,56)+(55,40)+(5,4)		
^{138}Ba +^{95}Zr +^{10}Be	(**82**,56)+(55,40)+(6,4)		
^{141}Ba +^{90}Y +^{11}Be	(83,58)+(52,38)+(7,4)	^{138}Ba +^{93}Zr +^{11}Be	(**82**,56)+(53,40)+(7,4)
^{140}Ce +^{90}Sr +^{12}Be	(**82**,58)+(52,38)+(**8**,4)		
^{138}Ba+^{91}Sr +^{13}C	(**82**,56)+(53,38)+(7,6)		
^{138}Ba+^{90}Sr +^{14}C	(**82**,56)+(52,38)+(**8**,6)		
^{138}Ba+^{89}Sr +^{15}C	(**82**,56)+(51,38)+(9,6)		
^{138}Ba+^{88}Sr +^{16}C	(**82**,56)+(**50**,38)+(10,6)		
^{139}La+^{86}Kr +^{17}N	(**82**,57)+(**50**,36)+(10,7)	^{137}Cs+^{88}Sr +^{17}N	(**82**,55)+(**50**,38)+(10,7)
^{138}Ba+^{86}Kr +^{18}O	(**82**,56)+(**50**,36)+(10,**8**)		
^{137}Ba+^{86}Kr +^{19}O	(81,56)+(**50**,36)+(11,**8**)		
^{136}Ba+^{86}Kr +^{20}O	(80,56)+(**50**,36)+(12,**8**)		
^{133}Xe+^{88}Sr +^{21}O	(79,54)+(**50**,38)+(13,**8**)		
^{132}Xe+^{88}Sr +^{22}O	(78,54)+(**50**,38)+(14,**8**)		
^{131}I+^{88}Sr +^{23}F	(78,53)+(**50**,38)+(14,9)		
^{132}Xe+^{86}Kr +^{24}Ne	(78,54)+(**50**,36)+(14,10)	^{132}Te+^{88}Sr +^{24}Ne	(80,52)+(**50**,38)+(14,10)
^{129}Te+^{88}Sr +^{25}Ne	(77,52)+(**50**,38)+(15,10)		
^{128}Te+^{88}Sr +^{26}Ne	(76,52)+(**50**,38)+(16,10)		
^{129}I+^{86}Kr +^{27}Na	(76,53)+(**50**,36)+(16,11)	^{127}Sb+^{88}Sr +^{27}Na	(76,51)+(**50**,38)+(16,11)
^{128}Te+^{86}Kr +^{28}Mg	(76,52)+(**50**,36)+(16,12)		
^{127}Te+^{86}Kr +^{29}Mg	(75,52)+(**50**,36)+(17,12)	^{124}Sn+^{89}Sr +^{29}Mg	(74,**50**)+(51,38)+(17,12)

ECT		CCT	
Fragment combination	$(N_1,Z_1)+(N_2,Z_2)+(N_3,Z_3)$	Fragment combination	$(N_1,Z_1)+(N_2,Z_2)+(N_3,Z_3)$
^{126}Te+^{86}Kr +^{30}Mg	(74,52)+(**50**,36)+(18,12)	^{124}Sn+^{88}Sr +^{30}Mg	(74,**50**)+(**50**,38)+(18,12)
^{123}Sn+^{88}Sr +^{31}Mg	(73,**50**)+(**50**,38)+(19,12)		
^{122}Sn+^{88}Sr +^{32}Mg	(72,50)+(**50**,38)+(**20**,12)		
^{123}Sn+^{86}Kr +^{33}Si	(73,**50**)+(**50**,36)+(19,14)		
^{140}Ce+^{68}Ni +^{34}Si	(**82**,58)+(40,**28**)+(**20**,14)	^{122}Sn+^{86}Kr +^{34}Si	(72,**50**)+(**50**,36)+(**20**,14)
^{140}Ce+^{67}Ni +^{35}Si	(**82**,58)+(39,**28**)+(21,14)	^{121}Sn+^{86}Kr +^{35}Si	(71,**50**)+(**50**,36)+(21,14)
^{140}Ce+^{66}Ni +^{36}Si	(**82**,58)+(38,**28**)+(22,14)	^{120}Sn+^{86}Kr +^{36}Si	(70,**50**)+(**50**,36)+(22,14)
^{139}La+^{66}Ni +^{37}P	(**82**,57)+(38,**28**)+(22,15)	^{119}In+^{86}Kr +^{37}P	(70,49)+(**50**,36)+(22,15)
^{138}Ba+^{66}Ni +^{38}S	(**82**,56)+(38,**28**)+(22,16)	^{122}Sn+^{82}Se +^{38}S	(72,**50**)+(48,34)+(22,16)
^{137}Ba+^{66}Ni +^{39}S	(81,56)+(38,**28**)+(23,16)	^{121}Sn+^{82}Se +^{39}S	(71,**50**)+(48,34)+(23,16)
^{136}Ba+^{66}Ni +^{40}S	(80,56)+(38,**28**)+(24,16)	^{120}Sn+^{82}Se +^{40}S	(70,**50**)+(48,34)+(24,16)
^{140}Ce+^{61}Fe +^{41}S	(**82**,58)+(35,26)+(25,16)	^{115}Cd+^{86}Kr +^{41}S	(67,48)+(**50**,36)+(25,16)
^{139}Tc+^{60}Fe +^{42}S	(**82**,58)+(34,26)+(26,16)	^{114}Cd+^{86}Kr +^{42}S	(66,48)+(**50**,36)+(26,16)
^{139}La+^{60}Fe +^{43}Cl	(**82**,57)+(34,26)+(26,17)	^{113}Ag+^{86}Kr +^{43}Cl	(66,47)+(**50**,36)+(26,17)
^{138}Ba+^{60}Fe +^{44}Ar	(**82**,56)+(34,26)+(26,18)	^{112}Pd+^{86}Kr +^{44}Ar	(66,46)+(**50**,36)+(26,18)
^{137}Ba+^{60}Fe +^{45}Ar	(81,56)+(34,26)+(27,18)	^{111}Pd+^{86}Kr +^{45}Ar	(65,46)+(**50**,36)+(27,18)
^{140}Ce+^{56}Cr +^{46}Ar	(82,58)+(32,24)+(28,18)	^{110}Pd+^{86}Kr +^{46}Ar	(64,46)+(**50**,36)+(**28**,18)
^{139}La+^{56}Cr +^{47}K	(**82**,57)+(32,24)+(**28**,19)	^{109}Rh+^{86}Kr +^{47}K	(64,45)+(**50**,36)+(**28**,19)
^{138}Ba+^{56}Cr +^{48}Ca	(**82**,56)+(32,24)+(**28**,**20**)	^{108}Ru+^{86}Kr +^{48}Ca	(64,44)+(**50**,36)+(28,**20**)
^{141}Ce+^{52}Ti +^{49}Ca	(83,58)+(30,22)+(29,**20**)	^{107}Ru+^{86}Kr +^{49}Ca	(63,44)+(**50**,36)+(29,**20**)
^{140}Ce+^{52}Ti +^{50}Ca	(**82**,58)+(30,22)+(30,**20**)	^{106}Ru+^{86}Kr +^{50}Ca	(62,44)+(**50**,36)+(30,**20**)
^{140}Ce+^{51}Ti +^{51}Ca	(**82**,58)+(29,22)+(31,**20**)	^{105}Ru+^{86}Kr +^{51}Ca	(61,44)+(**50**,36)+(31,**20**)
^{124}Te+^{66}Ni +^{52}Ca	(72,52)+(38,**28**)+(32,**20**)	^{105}Ru+^{86}Kr +^{52}Ca	(61,44)+(**50**,36)+(32,**20**)
^{123}Sb+^{66}Ni +^{53}Sc	(72,51)+(38,**28**)+(32,21)	^{103}Tc+^{86}Kr +^{53}Sc	(61,43)+(**50**,36)+(32,21)
^{122}Sn+^{66}Ni +^{54}Ti	(72,**50**)+(38,**28**)+(32,22)	^{102}Mo+^{86}Kr +^{54}Ti	(60,42)+(**50**,36)+(32,22)
^{121}Sn+^{66}Ni +^{55}Ti	(71,**50**)+(38,**28**)+(32,22)	^{101}Mo+^{86}Kr +^{55}Ti	(59,42)+(**50**,36)+(32,22)
^{120}Sn+^{66}Ni +^{56}Ti	(70,**50**)+(38,**28**)+(34,22)	^{100}Mo+^{86}Kr +^{56}Ti	(58,42)+(**50**,36)+(34,22)
^{119}Sn+^{66}Ni +^{57}Ti	(69,**50**)+(38,**28**)+(35,22)	^{99}Mo+^{86}Kr +^{57}Ti	(57,42)+(**50**,36)+(35,22)
^{118}Sn+^{66}Ni +^{58}Ti	(68,**50**)+(38,**28**)+(36,22)	^{98}Mo+^{86}Kr +^{58}Ti	(56,42)+(**50**,36)+(36,22)
^{117}In+^{66}Ni +^{59}V	(68,49)+(38,**28**)+(36,23)	^{97}Nb+^{86}Kr +^{59}V	(56,41)+(**50**,38)+(37,23)

It is important to mention that except for few cases, the the fragment combinations associate themselves with the magic shell at least for one fragment of tripartition. This result is an agreement with reference [37, 38]. Interestingly, some of the predicted third fragments A_3 in table 1 and 2 are either observed or predicted in cluster radioactivity studies or in induced ternary fission [23–27, 39, 40].

CCT mode is observed experimentally for ^{252}Cf nucleus by Pyaktov et al. in 2010 [42] using the missing mass method. In this experiment $^{48-56}$Ca is reported as the third fragment along with heavy Sn (Z=50 magicity) as one of the fragment. In the present calculations, $^{48-52}$Ca are emerged as third fragment in ECT as well as CCT mode for ^{242,258}Fm isotopes. The remaining fragments (fragment 1 and/or fragment 2) are reinforced via Z=50 or N=82 magicity as evident from Table 1 and 2. Henceforth, the present calculations are in reasonable agreement with the experiment data [42]. Previous experimental studies of ternary fission have pointed out that the third light fragment will emit in the perpendicular direction to the fission axis [14–17]. However, a collinear emission of three fragments of comparable masses is also identified [23–27] in many studies and called as collinear tripartition. To estimate the most preferred A_3 fragment among the predicted possibilities of ^{242,258}Fm nuclei for ECT and CCT modes of emission, the ternary fragmentation potential $V(A_2)$ is plotted for A_3=4, 30 and 80 (or 86) fragments in Figs. 7.2(a-d) for both equatorial and collinear cluster tripartition. Here, the ternary fragmentation potential is represented only for limited cases just for the clarity, however the trend remains same after the inclusion of other third fragment choices. One can clearly see from Figs.7.2(a) and 7.2(b) that the ternary fragmentation potential has lower magnitude for $A_3=^4$He case for ECT mode. The magnitude of fragmentation potential increases with increment in mass of third fragment, and hence one may conclude that the emergence of lightest third fragment is most favourable at equatorial partition of the parent nuclei. However, for CCT case, the heavier third fragments start competing the lighter ones as shown in Figs. 7.2(c) and 7.2(d) for both parent nuclei. For further analysis, Figs. 7.3(a) and 7.3(b) represent the decay Q-value (triangles) and ternary fragmentation potential V(MeV) (squares) corresponding to fragment combinations as listed in table 1 of ^{242}Fm parent nucleus with respect to the third fragment mass A_3 for the ECT and the CCT ternary emission modes. The dotted lines are used to label the minima of potential and maxima of Q-value. It is observed that the A_3 fragments like ^{4}He, ^{8}Be, ^{14}C, ^{18}O, ^{24}Ne, ^{28}Mg, ^{34}Si, ^{38}S, ^{44}Ar, ^{48}Ca, ^{54}Ti, ^{60}Cr, ^{64}Fe, ^{66}Fe, ^{70}Ni, ^{76}Zn and

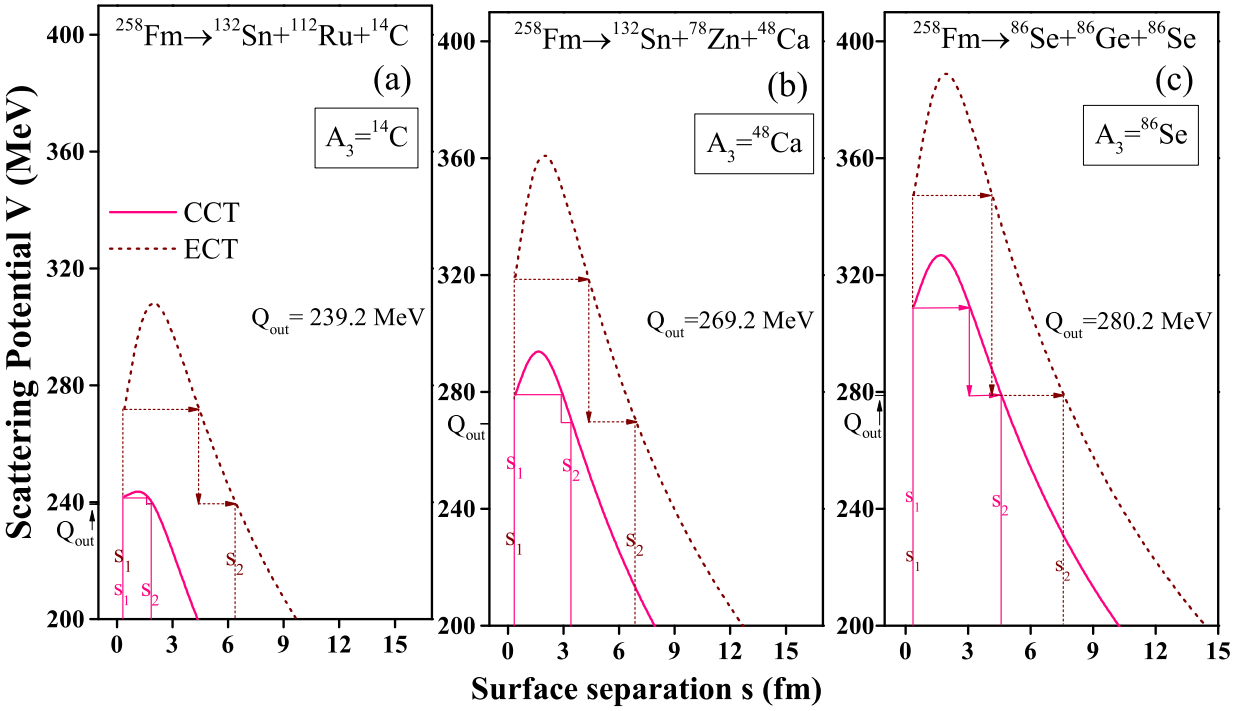

Figure 7.4: The calculated scattering potential V(MeV) as a function of surface separation distance (s) for fixed third fragments such as (a) ^{14}C, (b) ^{48}Ca and (c) ^{86}Se of ^{258}Fm for both ECT and CCT emission modes.

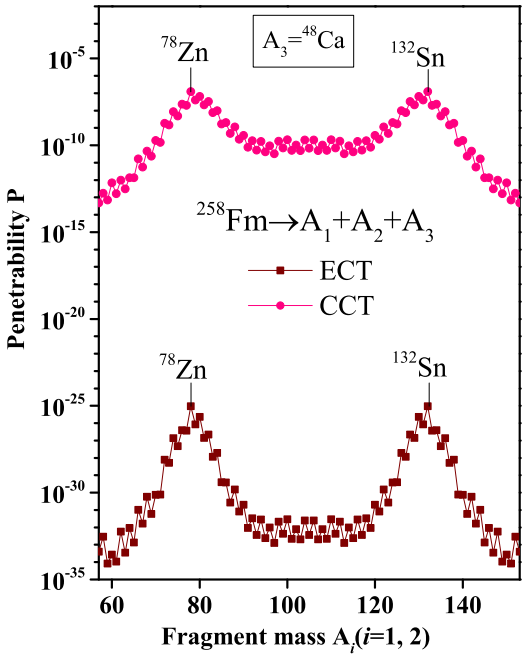

Figure 7.5: Penetrability P as a function of A_i (i=1,2) of ^{258}Fm parent nucleus for A_3=^{48}Ca to compare equatorial and collinear emission modes.

^{80}Ge have maxima in Q-value and minima in the fragmentation potential. Interestingly, the systematics of Q-value and potential energy support the emission of even-mass third particles strongly. The fragmentation potential has higher magnitude for equatorial emission than the collinear mode particularly for heavier third fragments, for instance, it is around 40 MeV for true ternary fission (TTF), i.e. ^{82}Kr+^{80}Se+^{80}Ge, indicating that heavier third fragments have more possibility in collinear emission. The compelling reason behind this difference is the Coulomb potential because it reduces in the CCT configuration due to the large inter-fragment distance between A_1 and A_2 fragments, see Fig. 2.3(b). Moreover, this effect is large for heavy fragments due to higher charge and mass numbers. Therefore, one can say that heavy fragments and true (symmetric) ternary fission prefer the CCT emission as observed in various studies [23–27]. A deeper look of Fig. 7.3 supports that ^{4}He is the most preferred third fragment for both equatorial and collinear configurations. Similar result is observed in the experiment study of ^{256,257}Fm isotopes [41]. However, the potential energy of heavier fragments in CCT mode is much lower than the ECT mode, see the shaded area in the figure. This indicates that heavier third fragment starts competing the lighter third fragment in CCT mode. It is to be noted here that the ^{258}Fm has shown the same behaviour as we noticed for ^{242}Fm nucleus for both CCT and ECT configurations.

Figs.7.4(a-c) depict the scattering potential which is calculated using $V = V_{C_{ij}} + V_{P_{ij}}$ relation as a function of separation distance (s) for three choices of third fragments such as A_3=^{14}C, ^{48}Ca and ^{86}Se. The scattering potential denotes the interaction between the fragments by increasing the value of the surface separation 's' as in Eqs. (19) and (23) for ECT and CCT modes. Here in present case, I have varied the surface separation distance uniformly in ECT and CCT mode without varying the radius of corresponding fragments unchanged. The idea is to visualize the impact of variation in magnitude of surface separation distance on the barrier characteristics and also the penetration probability of the fragments emerged in these two configurations. In the present calculations, the first turning point s_1=0.4 fm is common for all choices of third fragments for better comparison and for which the barrier penetration works. It is found that the height of the barrier is lower for the CCT configuration as compared to the ECT. This indicates that collinear division of parent nuclei seems preferable than the equatorial emission for the considered cases. Further, the penetrability P and relative fission yield $Y(A_i,Z_i)$ are calculated using equations (2.34) and (2.36), to analyze the ternary fission fragment mass distributions of ^{242,258}Fm parent nuclei.

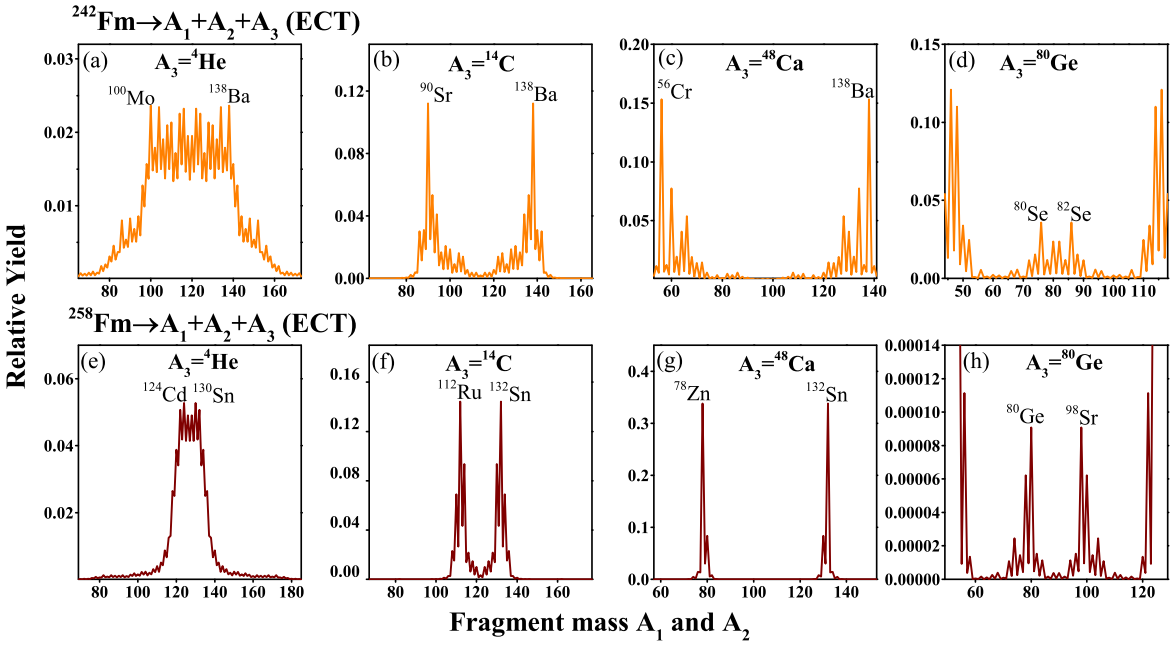

Figure 7.6: The calculated relative fission yield as a function of fragment masses A_1 and A_2 for (a) ^{242}Fm and (b) ^{258}Fm for fixed A_3 fragments such as ^{4}He, ^{14}C, ^{48}Ca and ^{80}Ge for ECT approach.

A relative study of barrier penetration is carried out by plotting TCM-calculated penetrability P as a function of fragment mass A_i (i=1,2) for ECT and CCT emission modes for A_3=^{48}Ca fragment of ^{258}Fm nucleus (see Fig.7.5). The penetration probability is higher for collinear decay mode as compared to equatorial one, because the barrier height for CCT mode is much lower than the ECT (see fig.7.4). However, in both configurations the choice of most favorable fragment combination remains same (^{132}Sn+^{78}Zn+^{48}Ca) having maximum penetrability. Figs. 7.6(a-d) and 7.6(e-h) represent the relative ternary fission yield of ^{242}Fm and ^{258}Fm nuclei as a function of fragment mass A_1 and A_2 for a few selected third fragments for ECT configuration. The considered A_3 fragments such as ^{4}He, ^{14}C, ^{48}Ca, ^{80}Ge leaving the remaining system (A_P-A_3) as ^{232}Cf, ^{228}Pu, ^{194}Hg, ^{162}Er for ^{242}Fm parent nucleus, and ^{254}Cf, ^{244}Pu, ^{210}Hg, ^{178}Er for ^{258}Fm nucleus. The lower limit of mass distribution is decided by taking 0.55 fraction of (A_P-A_3)/2, and higher limit is the related complementary element for each case of A_3 fragment. One may notice that the ternary fission mass distribution changes from becomes more asymmetric for heavier third fragment. However, the overall distribution remains asymmetric in nature. The most probable fission fragments A_1+A_2 are also marked in the figure which are same as observed across minima of the fragmentation potential. Interestingly, the nature of ternary fission mass yield of the remaining nuclei, i.e.,

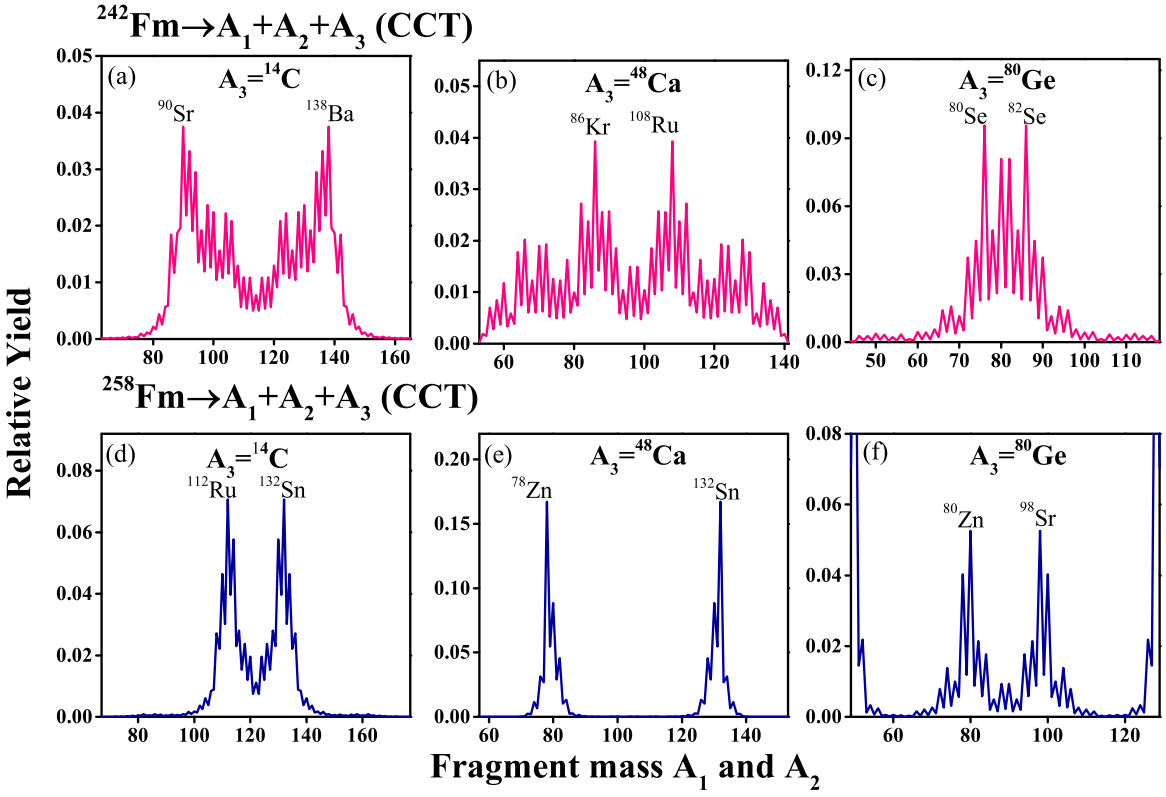

Figure 7.7: The calculated relative fission yield as a function of fragment masses A_1 and A_2 for (a) ^{242}Fm and (b) ^{258}Fm for fixed A_3 fragments such as ^{14}C, ^{48}Ca and ^{80}Ge for CCT approach.

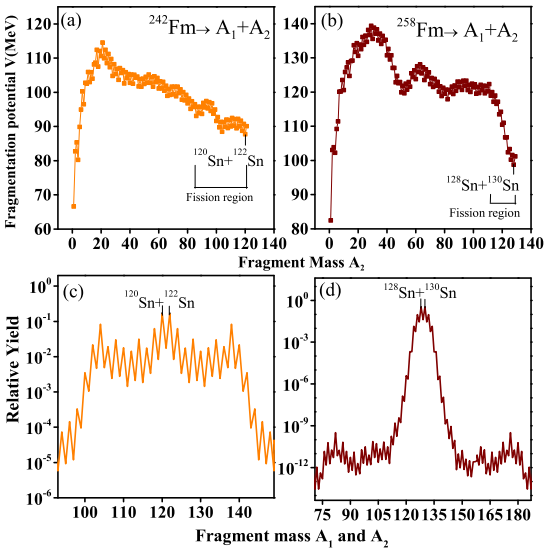

Figure 7.8: The binary fragmentation potential (a,b) as a function of fragment mass A_2 and relative yield (c,d) as a function of fragment masses A_1 and A_2 using PCM. The most probable binary fission channel is also shown.

asymmetric, remains same as the binary fission mass distributions of such nuclei is studied in Refs. [43–46]. Similar kind of results are observed for the CCT case as plotted in Figs. 7.7(a-c) and 7.7(d-f) respectively for ^{242}Fm and ^{258}Fm nuclei. The choice of A_1 and A_2 fragments may change as one shift from ECT to CCT configuration. Note that, the relative yield for the case of A_3=^{4}He is not shown in Fig. 7.7 for CCT case, because the barrier potential V(s) is much lower than Q value of the ^{4}He decay, and hence the barrier penetration is not possible. In our previous work of binary fission of Fm isotopes [10], it was observed that mass distribution gets modified with increase in mass of Fm isotopes from A_P=242 to 260, irrespective of deformation effects. Figs.7.8(a) and 7.8(b) represent binary fragmentation potential for ^{242}Fm and ^{258}Fm, respectively. It is depicted from figures that for the spherical choice of fission fragments, symmetric fission is prominent for both fissioning nuclei. However, the symmetric valley becomes deeper for ^{258}Fm as compared to ^{242}Fm. Further, the relative yield of both nuclei is represented in Figs.7.8 (c) and 7.8(d), and it represents similar result as reported in the fragmentation potential. That means, the broader symmetric peak of ^{242}Fm becomes sharper for ^{258}Fm nucleus. Therefore, one can say that the binary fission prefers the symmetric distribution for considered Fm isotopes, whereas asymmetric behaviour of relative mass yield is observed for the case of ternary fission. Further for the relevant discussion of binary fission, one may refer our recent paper [10], which also suggests that deformation and orientation effects play important role in the binary division. In view

of this, it would be of interest to employ the deformation and orientation effects in ternary fragmentation of fissioning nuclei that will be taken as our future assignment.

7.3 Summary

Summarizing, the ternary fission analysis of ^{242}Fm and ^{258}Fm isotopes is carried out within collinear cluster tripartition (CCT) and equatorial cluster tripartition (ECT) configurations. Three body fragmentation potential is used to fix the third fragment (A_3) among various possibilities. The systematics of Q-value and ternary fragmentation potential supports the emission of even-mass third fragments. The most probable fission channels (A_1+A_2+A_3) are identified for a wide range of light and heavy mass third fragments (1 to $A_P/3$), where A_P is mass of the parent nucleus. It is observed that at least one among the three probable ternary fission fragments, associate with the neutron or proton closed shell. A relative study of equatorial and collinear emission in context of ternary fragmentation potential reveals that the light mass third fragments are equally probable for both ECT and CCT modes. However, the heavier mass third fragments start competing the lighter one in collinear mode due to large inter-fragment distance and have lower magnitude of Coulomb potential. Further, the barrier height and barrier penetrability P are analyzed for both ECT and CCT configurations. The barrier height is observed to be lower and barrier penetrability P is higher for the CCT as compared to ECT configuration, indicating that collinear emission may be preferred over the equatorial one. Finally, a relative comparison of binary and ternary fission has been carried out in reference to fragmentation structure and relative yield. It may be of further interest to include deformation effects in the ternary fragmentation of fissioning nuclei.

The overall outcome of this work and major conclusions drawn are briefly outlined in the last chapter.

Bibliography

[1] A. Allisy, Radiat. Prot. Dosim. **68**, 3 (1996).

[2] H. J. Rose and G. A. Jones, Nature (London) **307**, 245 (1984).

[3] D. N. Poenaru, R. A. Gherghescu, and W. Greiner, Phys. Rev. Lett. **107**, 062503 (2011).

[4] G. N. Flerov and K. A. Petrzhak, Phys. Rev. **58**, 275 (1940).

[5] A. N. Andreyev, M. Huyse, and P. Van Duppen, Rev. Mod. Phys. **85**, 1541 (2013).

[6] I. V. Ryzhov *et al.*, Phys. Rev. C **83**, 054603 (2011).

[7] A. N. Andreyev *et al.*, Phys. Rev. Lett. **105**, 252502 (2010).

[8] J. E. Gindler, K. F. Flynn, L. E. Glendenin, and R. K. Sjoblom, Phys. Rev. C **16**, 1483 (1977).

[9] E. K. Hulet *et al.*, Phys. Rev. C **40**, 770 (1989).

[10] A. Kaur, N. Sharma, and M. K. Sharma, Phys. Rev. C **103**, 034618 (2021).

[11] L. W. Alvarez, as reported by G. Farewell, E. Segre, and C. Wiegand, Phys. Rev. **71**, 327 (1947).

[12] H. Diehl and W. Greiner, Nucl. Phys. A. **229**, 29-46 (1974).

[13] M. Luis Muga , Phys. Rev. Lett. **11**, 129 (1963).

[14] A. V. Ramayya *et al.*, Nuovo Cimento A **110**, 1073 (1997); Phys. Rev. C **229**, 2370 (1998).

[15] K. Manimaran and M. Balasubramaniam, Phys. Rev. C **79**, 024610 (2009).

[16] A. K. Nasirov, R. B. Tashkhodjaev and W. von Oertzen, Eur. Phys. J. A, **52**, 135 (2016).

[17] A. V. Karpov, Phys. Rev. C **94**, 064615 (2016).

[18] S. W. Cosper, J. Cerny, and R. C. Gatti, Phys. Rev. **154**, 1193 (1967).

[19] G. M. Raisbeck, T. D. Thomas, Phys. Rev. **172**, 1272 (1968).

[20] S. L. Whetstone, T. D. Thomas, Phys. Rev. Lett. **15**, 298 (1965); Phys. Rev. **154**, 1174 (1967).

[21] D. N. Poenaru *et al.* Romanian reports in physics. **55**, 549-554 (2003).

[22] K. R. Vijayaraghavan, M. Balasubramaniam, and W. von Oertzen, Phys. Rev. C **91**, 044616 (2015).

[23] R. H. Iyer and J. W. Cobble, Phys. Rev. **172**, 1186 (1968).

[24] L. Rosen and A. M. Hudson, Phys. Rev. **78**, 533 (1950).

[25] R. L. Fleischer, P. B. Price, R. M. Walker, and E. L. Hubbard, Phys. Rev. **143**, 943 (1966).

[26] V. P. Perelygin, N. H. Shadieva, S. P. Tretyakova, A. H. Boos, and R. Brandt, Nucl. Phys. A **127**, 577 (1969).

[27] H. J. Becker, P. Vater, R. Brandt, and A. H. Boos, Phys. Lett. B **50**, 24 (1974).

[28] S. Thakur *et al.*, Int. J. Mod. Phys. E. **22**, 1350014 (3) (2013).

[29] K. Manimaran and M. Balasubramaniam, Phys. Rev. C **83**, 034609 (2011).

[30] N. Sharma, A. Kaur and M. K. Sharma , Phys. Rev. C **105**, 044602 (2022).

[31] J. Maruhn and W. Greiner, Phys. Rev. Lett. **32**, 548 (1974).

[32] R. K. Gupta, W. Scheid, and W. Greiner, Phys. Rev. Lett. **35**, 353 (1975).

[33] R. K. Gupta, A. Sandulescu, and W. Greiner, Phys. Lett. B **67**, 257 (1977)

[34] N. Sharma, A. Kaur, and M. K. Sharma, Phys. Rev. C **102**, 064603 (2020).

[35] K. Sharma, G. Sawhney, and Manoj K. Sharma, Phys. Rev. C **96**, 054307 (2017).

[36] W von Oertzen and A K Nasirov , Journal of physics; conference series **569**, 012040 (2014).

[37] A. Algora, J. Cesh, J. Darai, P. O. Hess, Phys. Lett. B **639**, 451 (2006).

[38] Yu. V. Pyatkov *et al.*, Rom. Rep. Phys. **59**, 569 (2007).

[39] R.K. Gupta and W. Griener, Int. J. Mod. Phys. E. **03**, 335 (2) (1994).

[40] R. Bonetti and A. Guglielmetti, Rom. Rep. Phys. **29**, 301 (2007).

[41] J. F. Wild, P. A. Baisden, R. J. Dougan, E. K. Hulet, R. W. Lougheed, and J. H. Landrum, Phys. Rev. C **32**, 488 (1994).

[42] Yu. V. Pyatkov *et al.*, Eur. Phys. J. A **45**, 29 (2010).

[43] A. V. Andreev, G. G. Adamian, N. V. Antonenko, and A. N. Andreyev, Phys. Rev. C **88**, 047604 (2013).

[44] H. Pasca, A. V. Andreev, G. G. Adamian, and N. V. Antonenko, Phys. Rev. C **99**, 064611 (2019)

[45] K. Sharma, G. Sawhney, Manoj K. Sharma, and R. K. Gupta, Nucl. Phys. A **972**, 1 (2018).

[46] N. K. Virk, R. Kumar, and M. K. Sharma, Int. J. Mod. Phys. E **30**, 2150001 (2021).

Chapter 8

Summary

In the present work, the binary and ternary decay analysis of different nuclei is made using the collective clusterization approach. The binary decay modes include the α decay, cluster radioactivity (CR), heavy particle radioactivity (HPR), and the spontaneous fission (SF). These decay modes are generally observed in the nuclei belonging to the heavy and superheavy mass region. One of the interesting properties of such nuclei is that they can decay via one or multiple channels of the above mentioned decay modes. Hence, in present work, an attempt is made to make comparative analysis of all these decay modes using different factors such as the shell effect, deformation, orientation, and the decay half-lives etc. In addition to this, there is also possibility of three fragment emission from the heavy mass nuclei. Hence, after the binary decay analysis, efforts are made to workout the three body fragmentation analysis and related aspects are explored. The binary and ternary fragmentation analysis is done using the preformed cluster model (PCM) and three cluster model (TCM), respectively.

Using PCM, the α decay analysis of $^{188-218}$Po isotopes is made nearby N=126 and the role of neutron shell closure effect is explored. The barrier characteristics of the α decay channel are studied with and without the inclusion of surface diffuseness parameter. The fragmentation structure of ^{188}Po,^{202}Po, and ^{218}Po isotopes is explored, where α particle is observed as the most probable decay fragment for the chosen set of Po isotopes. The preformation probability, barrier penetration probability and assault frequency (classical and quantum) are calculated and the influence of neutron shell closure of the parent nucleus is explored. The PCM calculated P_0,P and ν are compared with the different theoretical approaches. The classical mode of the assault frequency (ν_c) depends on the Q value of the decay channel and its quantum mechanical mode (ν_q) depends on the global quantum number. The decay half-lives of alpha emission are calculated using both choices of assault frequency and a comparison is made with the results of CPPM, ADF, UDL, SLH, SLB, SemFIS and the available experimental data . The deformed (β_2) choice of the decaying fragments gives

better agreement with the experimental data as compared to the spherical choice. The calculated α decay half-life is found to be maximum nearby N=126. The verification of G-N law is made using the calculated decay half-lives and its dependency on the Q value of the decay channel is explored. The effective assault frequency parameter ν_e is obtained using P_0 and the quantum assault frequency (ν_q). The alpha decay half-lives are calculated using ν_e and are found in good agreement with the experimental data for Po and Rn isotopes.

After the alpha decay analysis, other probable binary decay modes (such as α, cluster, HPR, SF) of ^{253}Es nucleus are studied using PCM. The binary decay mechanisms are explored using two kinds of attractive nuclear potentials i.e. Yukawa plus exponential and proximity potential. The barrier characteristics for the α decay process are compared using both nuclear potentials. The coulomb barrier is smaller for the case of proximity potential, hence the α particle emission probability is higher for this potential. After the barrier analysis, the fragmentation potential and the preformation probability are calculated and the most probable fragments are identified. The identified decay fragments are similar for both nuclear potentials, but there is significant change in the magnitude of the fragmentation potentials. The choice of most probable fission fragments depicts the importance of shell closure effect. The decay half-lives are calculated for all decay mechanisms (α, cluster, HPR, SF) for both choices of nuclear potentials. The proximity potential based PCM-calculated half-lives of α and SF channels show nice agreement with experimental data. Besides this, the half-lives are predicted for cluster radioactivity and heavy particle radioactivity. A comparison of the fragmentation potential, preformation probability (P_0) and the barrier penetrability (P) of all binary decay mechanisms is made where alpha decay and spontaneous fission appear as prominent decay modes for both the nuclear potentials.

The deformation and orientation efects play an important role in the decay dynamics of the nuclei. In the next step, the spontaneous fission (SF) of $^{242-260}$Fm isotopes is studied within preformed cluster model (PCM) by including the deformation and orientation effects. We have computed the fission fragment mass distributions for three types of configurations such as spherical, quadrupole β_2-deformed 'hot-compact' and β_2-deformed 'cold-elongated'. The interaction radius decreases as one goes from cold-elongated to spherical to hot-compact shapes, whereas interaction barrier height increases for the same sequence. These results effect the barrier characteristics and corresponding the fragmentation potential, because the potentials involved strongly depend on the deformation and interaction radius of the decay

fragments. The spherical and β_2-deformed hot-compact configurations depict the symmetric pattern for each fermium isotope, however, the symmetric peaks become sharp with an increase in the neutron (N) number of the parent nucleus. The β_2-deformed cold-elongated shapes of decay fragments show a transition from double humped (asymmetric fission) to triple humped (multi-modal fission) mass distribution. The heavier isotopes such as ^{258,260}Fm exhibit multi-modal fission (i.e. co-existence of both symmetric and asymmetric fission) for the cold configuration criteria. Spherical and β_2-deformed hot-compact approaches show that Fm isotopes decay via spherical magic shell closure [Sn (Z=50) isotopes]. However, for cold-orientations, Fm nuclei prefer to decay via asymmetric fragments having deformed magic shell closures of Z=38 and N=60,62. This concludes that spherical as well as deformed magic shell closures play important role in the fission dynamics of Fm isotopes. The decay half-lives of the considered spontaneous fissioning nuclei are calculated and found in nice agreement with the experimental data.

As we discussed earlier that the nuclei belonging to heavy mass region may undergo ternary decay mechanism. Hence, after the binary decay analysis, three cluster model (TCM) is used to study ternary decay process of ^{253}Es nucleus. The calculations are performed using two kinds of attractive nuclear potentials i.e. Yukawa plus exponential and proximity potential. It is observed that ^{253}Es may also decay via particle-accompanied fission, where third particle is identified as ^{4}He. The most probable fission fragments are identified using the fragmentation structure. The probability of ternary fission seems higher for the choice of the proximity potential. The fragmentation structure and the choice of most probable A_1+A_2 fragments is same for both cases, where the third fragment is fixed (A_3=^{4}He). The barrier characteristics for the most probable decay channel is compared for both of the nuclear potentials. There is significant change in the barrier position and barrier height for both of the choices. Further, a comparative analysis of binary and ternary fission is carried out. The relative yield of symmetric binary fragments is higher than the ternary fission. The most probable decay fragments are identified for binary as well as ternary fission. Finally, it is observed that magic shell effects near Z=50 and N=82 play important role for binary as well as ternary fission dynamics.

The ternary fission analysis of ^{242}Fm and ^{258}Fm isotopes is carried out within collinear cluster tripartition (CCT) and equatorial cluster tripartition (ECT) configurations. Three body fragmentation potential is used to fix the third fragment (A_3) among various possibilities.

The systematics of Q-value and ternary fragmentation potential support the emission of even-mass third fragments. The most probable fission channels (A_1+A_2+A_3) are identified for a wide range of light and heavy mass third fragments (1 to $A_P/3$), where A_P is the mass of parent nucleus. It is observed that at least one among the three probable ternary fission fragments, associate with the neutron or proton closed shell. A relative study of equatorial and collinear emission in context of ternary fragmentation reveals that, the light mass third fragments are equally probable for both ECT and CCT modes. However, heavier mass third fragments start competing the lighter one in collinear mode due to large inter-fragment distance and have lower magnitude of Coulomb potential. Further, the barrier height and barrier penetrability P are analyzed for both ECT and CCT configurations. The barrier height is observed to be lower and barrier penetrability P is higher for the CCT as compared to ECT configuration, indicating that the collinear emission may be preferred over the equatorial one. Finally, a relative comparison of binary and ternary fission has been carried out in reference to fragmentation structure and relative yield.

FUTURE SCOPE

In the present work, comprehensive analysis of the binary and ternary decay mechanism is done using the collective clusterization approach for the heavy mass region. Different terms such as the fragmentation potential, preformation probability, penetration probability and the assault frequency are employed to study various binary radioactive decay modes. Three body fragmentation potential and barrier characteristics are used for the exploration of the ternary decay mechanism. The obtained results are in good agreement with the available experimental data and few predictions are made for which experimental verification will be of interest. The present work can be extended and following points will be of future interest:

(i) The effective assault frequency parameter (ν_e) may be used in the study of α-disintegration process. This work can be further expanded by introducing this parameter for other heavier decay modes (CR, HPR and SF etc.).

(ii) The comparative analysis of different binary decay modes such as α decay, cluster radioactivity (CR), heavy particle radioactivity (HPR), and the spontaneous fission (SF) is carried out using spherical choice of the decaying fragments. In addition to these modes, comparison of other experimentally observed radioactive decay modes such as Proton (p) radioactivity, 2P- radioactivity and the double α decay can be made by incorporating the deformation effects.

(iii) The fragmentation analysis of the light charge particle accompanied fission is made and comparison is done with binary fission fragments. This work can be extend by incorporating the deformations and orientation effects and their related mass distribution can be compared.

(iv) The ECT and CCT modes of the ternary fission are considered as a simultaneous emission process in this work. The CCT mode can be studied as a sequential process and comparison of both sequential and simultaneous approach can worked out.

(v) The ternary decay mechanism in the present work is explored using three cluster model (TCM), where temperature effects remains silent. In future, temperature effects can be included in the methodology to explore the induced ternary decay mechanism.